Temperature measurement of high-energy-density matter generated by intense heavy ion beam

Vom Fachbereich Physik der
Technischen Universität Darmstadt

zur Erlangung des Grades eines
Doktors der Naturwissenschaften
(Dr. rer. nat.)

genehmigte Dissertation von

Dipl.-Phys. Pavel Ni
aus Alma-Ata

Darmstadt 2006
D 17

-I dedicate this work to my grandfathers,
Dipl.-Jur., Dipl.-Hist. Petr Alexandrovich Truhin
and Prof. Dr. Dr. h.c. mult. Leonid Pavlovich Ni.

Referent: Prof. Dr. Dr. h.c./RUS Dieter H.H. Hoffmann
Korreferent: Prof. Dr. Markus Roth

Tag der Einreichung: 4.7.2006
Tag der Prüfung: 24.7.2006

Zusammenfassung

Intensive Schwerionenstrahlen sind ein hervorragendes Werkzeug, um Materie hoher Energiedichte (HED = High Energy Density) in makroskopischen Volumina zu erzeugen, in denen nahezu homogene physikalische Bedingungen herrschen. Die Untersuchung von Materie unter extremen physikalischen Bedingungen in Bezug auf Dichte, Temperatur und Druck ist von fundamentalem Interesse für die Forschung auf den Gebieten der Plasmaphysik, Atomphysik, Astrophysik und Geophysik, sowie für Forschung und Anwendungen auf dem Gebiet der Inertialfusion.

Erst kürzlich wurde eine Reihe von Experimenten zu Materie im Zustand hoher Energiedichte, die durch Schwerionenstrahlen erzeugt wurde, bei der GSI Darmstadt am Messplatz HHT durchgeführt. Bei diesen Experimenten wurden makroskopische, metallische Targets von intensiven Schwerionenstrahlen homogen, quasi-isochor geheizt, wobei Materiezustände hoher Energiedichte und hoher Entropie entstehen. Das geheizte Targetmaterial expandiert isentropisch und durchläuft dabei Zustände von grossem physikalischem Interesse, die sich sowohl im Bereich der Verdampfungskurve, des Zweiphasen-Flussigkeit-Gas-Zustands als auch im Bereich des kritischen Punkts des Phasendiagramms befinden. Die fundamentalen thermodynamischen Eigenschaften des Targets wurden dabei sowohl während der Aufheizungs- als auch der Ausdehnungsphase gemessen.

Das Hauptziel dieser Arbeit ist die dynamische Temperaturmessung des Targetmaterials während der Bestrahlung mit Schwerionenstrahlen. Im Zuge diese Arbeit wurde ein schnelles Mehrkanal-Pyrometer entwickelt und während mehrerer Strahlzeiten erfolgreich getestet und eingesetzt. Das Pyrometer erlaubt es sogenannte "Brightnesstemperaturen" (die Temperatur bei der die gemessene Strahlungsleistung der eines schwarzen Korpers in diesem Frequenzbereich entspricht) bei 12 Wellenlängen zu messen, wobei die zeitliche Auflösung im Nanosekundenbereich und die räumliche Auflösung im Mikrometerbereich liegt. Die "Brightnesstemperaturen" werden durch die Auswertung der Planckschen Strahlungsverteilung im sichtbaren und nahen-infrarot Spektralbereich bestimmt. Die gesamte emittierte Strahlung des aufgeheizten Targets, die vom Pyrometer über alle 12 Wellenlängen gemessen wird, erlaubt es auch eine physikalische Temperatur des Targets zu definieren. Dies geschieht durch Anpassung der Temperatur an unterschiedliche theoretische Modelle für die Emission im betrachteten Spektralbereich.

In den hier durchgeführten HED-Experimenten mit Schwerionenstrahlen wurden zum ersten Mal Targettemperaturen, die zwischen 1000 K — 12000 K lagen, gemessen. Zusätzlich zu der Temperatur wurde die Geschwindigkeit der Expansion der Targetmaterie gemessen, dies geschah mit einem Backlighting/Schattenwurf-Messystem, das auf einer Aufzeichnung der Emission des Targetmaterials mit einer Streakkamera basiert. Für das Targetmaterial Blei wurden Expansionsgeschwindigkeiten bis zu 2600 m/s gemessen, für Wolfram war die Expansionsgeschwindigkeit mit bis zu 1700 m/s geringer.

Diese Arbeit stellt die ersten experimentellen Resultate vor, die für Temperaturmessungen im Bereich von Materie hoher Energiedichte, erzeugt durch Schwerionenstrahlen, erzielt werden konnten. Das in diesem Rahmen entwickelte schnelle Mehrkanalpy-

rometer ist unentbehrlich, sowohl für die momentan laufenden und in Zukunft geplanten HED Experimente bei GSI und auch im Hinblick auf das zukünftige FAIR-Projekt. Genauso sind die gewonnenen experimentellen Daten und die während dieser Arbeit entwickelten Diagnostiken richtungsweisend für die geplanten HED-Experimente bei GSI und die zukünftigen Experimente beim FAIR-Projekt.

Summary

Intense heavy ion beams are an excellent tool to create large-volume samples of high energy density (HED) matter with fairly uniform physical conditions. Experimental study of matter under extreme conditions of density, temperature and pressure is of considerable interest to fundamental research in the fields of plasma physics, atomic physics, astrophysics, geophysics as well as for the inertial fusion research and its applications.

Recently, a series of HED physics experiments with heavy ion beams have been carried out at the GSI-Darmstadt. In these experiments, metallic targets of macroscopic volumes were heated by intense heavy ion beams uniformly and quasi-isochorically, thereby generating high-density, high-entropy states. The heated target material was expanding isentropically, passing through many interesting physical states located in the region of boiling curve, two-phase liquid-gas and the critical point. Most of the heavy ion beam energy is deposited within 120 ns which gives a possibility of appearance of intermediate meta-stable superheated liquid states. The fundamental thermodynamical properties of the target were measured during the heating as well as the expansion phases.

The main subject of this work is the dynamic temperature measurement of the target material in the HED physics experiments with intense heavy ion beams. In the course of this work a fast multi-channel radiation pyrometer has been developed and successfully employed in experimental campaigns. The pyrometer allows measurement of brightness temperatures at 12 wavelengths with a nanosecond temporal resolution and the micrometer spatial resolution. The brightness temperatures are obtained from analysis of the Planck radiation in visible and near-infrared spectral regions. The absolute radiation emission recorded by the pyrometer at different wavelengths allow also determination of the physical temperature using different models of spectral emissivity.

In the performed HED physics experiments with heavy ion beams target temperatures varying from 1000 K to 12000 K were measured for the first time. Different materials showed different behavior of hydrodynamic expansion, clearly seen on the pyrometer records. In addition to temperature measurements, measurements of target expansion dynamics have been carried out using a backlighting/shadowgraphy system based on a streak camera. Expansion velocities up to 2600 m/s have been registered for lead and up to 1700 m/s for tungsten targets.

This work presents the first experimental results on temperature measurement in HED physics experiments with intense heavy ion beams. The developed fast multichannel pyrometer is indispensable for the present and the future HED physics experiments at GSI. The new experimental data, developed diagnostics and experience obtained during the course of this work are also of a great importance for planning future HED physics experiments at FAIR.

Table of Contents

1 Introduction

A study of the fundamental properties of high-energy-density (HED) matter is an extremely important subject as it has very wide applications to basic as well as different branches of applied sciences. Matter under extreme conditions of density, temperature and pressure is frequently found in extraterrestrial objects such as stars and giant planets. HED matter can have super-solid densities, temperatures of the order of millions of Kelvin and pressures in the range of megabars. Experimental study of equation-of-state (EOS) of HED matter is of considerable interest to basic research of thermodynamic and hydrodynamic behavior of dense plasmas. This study will enable one to probe the validity of existing theories on stellar formation and evolution, compressibility of inertial fusion targets and existing models for strongly coupled high density plasmas. These phenomena are related to the field of plasma physics, astrophysics, geophysics and planetary sciences.

In order to study the properties of HED states, one has to create a HED sample in the laboratory. The traditional methods of creating samples of HED matter for experimental investigations can be divided into static and dynamic techniques. In static experiments diamond anvil cells are the main instrument, while in dynamic experiments a target material is usually compressed by shock waves. The most commonly used shock wave generators are chemical explosives, high-current Z-pinch and high power lasers. In several experiments nuclear explosions have also been employed to generate pressures in the range of Gbar.

The heavy ion synchrotron SIS-18 at the Gesellschaft für Schwerionenforschung (GSI, Darmstadt) is a unique facility worldwide that delivers intense beams of highly energetic heavy ions. Using these heavy ion beams, it is possible to heat macroscopic volumes of matter to extreme conditions of temperature and pressure with fairly uniform physical conditions.

Recently, a series of HED physics experiments with heavy ion beams have been carried out at the HHT ("high temperature") experimental area of the plasma physics group at GSI. In these experiments, metallic targets of macroscopic volumes were heated by intense heavy ion beams uniformly and quasi-isochorically, thereby generating high-density, high-entropy states. The heated target material was expanding isentropically, passing through many interesting physical states located in the region of boiling curve, two-phase liquid-gas and the critical point. Most of the heavy ion beam energy is deposited within 120 ns which gives a possibility of appearance of intermediate meta-stable superheated liquid states. The fundamental thermodynamical properties of the target were measured during the heating as well as the expansion phases.

The main subject of this work is the dynamic temperature measurement of the target material in the HED physics experiments with intense heavy ion beams. In the course of this work a fast multi-channel radiation pyrometer has been developed and successfully employed in experimental campaigns. The pyrometer allows measurement of brightness temperatures at 12 wavelengths with a nanosecond temporal resolution and a micrometer spatial resolution. The brightness temperatures are obtained from analysis of the Planck radiation in visible and near-infrared spectral regions. The absolute radiation emission recorded by the pyrometer at different wavelengths allow also determination of the physical temperature by employing

various models of spectral emissivity.

In the performed HED physics experiments with heavy ion beams, HED samples of various target materials such as copper, aluminum, tungsten, tantalum, sapphire and uranium dioxide, were generated and for the first time target temperatures varying from 1000 K to 12000 K were measured. Different materials showed different behavior of hydrodynamic expansion, clearly seen on the pyrometer records. In addition to temperature measurements, target expansion dynamics was measured using a backlighting/shadowgraphy system based on a streak camera. Expansion velocities up to 2600 m/s have been registered for lead and up to 1700 m/s for tungsten targets.

An upgrade of GSI facility to FAIR (Facility for Antiprotons and Ion Research) is planned in a near future. This upgrade will provider researcher with much more energetic and intense heavy ion beams. For example, it is estimated that the level of energy deposited by the future beam will be comparable to that generated by shocks produced by nuclear explosions. It is to note that the experimental work performed in the frame of this thesis is highly relevant to the FAIR project, since developed methods and techniques are planned to be used routinely in future experiments at FAIR.

In chapter 2, existing methods used to study HED of matter are reviewed. The technique of optical pyrometry and corresponding theoretical background are addressed there as well. Chapter 3 introduces the GSI accelerator facilities, the HHT experimental area, target design and various diagnostic methods employed in performed experiments. Chapter 4 gives a detailed description of the developed multi-wavelength pyrometer system, calibration procedure, data processing and accuracy of the measurement. The obtained results along with interpretation are presented in chapter 5. Finally, in chapter 6, the conclusions drawn from this study are exposed, outlining the main results of this work. Possible future extensions and improvements are also suggested.

2 Review of the field

This chapter presents a brief overview of the existing methods for EOS research of HED matter. Also, a new HIHEX technique for EOS study with intense heavy ion beams is explained. Advantages and limitations of each of these methods are discussed. Since the main theme of the thesis is the pyrometric temperature measurements, an overview of the existing temperature measurement techniques is also presented. At the end of this section, theoretical background of the physics in the performed experiments is briefly exposed.

2.1 Experimental methods for EOS studies

Thermodynamical properties of matter are characterized by macroscopical parameters that include pressure, internal energy, density, entropy, temperature, speed of sound and specific heat. An equation of state (EOS) describes a physical system by the relation between these parameters. One of the most trivial example is the EOS of an ideal gas

$$P \cdot V = \frac{m}{M} \cdot R \cdot T,$$

where P — is pressure, V — is volume, m — is mass, M — is molar mass, R — is the universal gas constant and T — is temperature. However, the EOS of real thermodynamical systems cannot be derived easily and in some cases, the only way to obtain it is to measure simultaneously three thermodynamic variables, for example density, pressure and temperature.

The EOS of lead in pressure-volume-temperature variables is presented in Figure 2.1 as a illustrative example. In this figure are shown regions corresponding to different phase states and phase transitions, experimental data that have been obtained using different techniques, including diamond anvil-cell (DAC), isobaric expansion (IEX) and shock compression of solid and porous material. A few release isentropes of shocked matter are plotted as well.

The existing methods of experimental study of EOS in the laboratory can be divided into static and dynamic techniques. All these methods are briefly reviewed below.

Diamond anvil cell (DAC). The main instrument in static experiments is the diamond anvil cell [1–3]. High pressures in this technique are achieved by squeezing a solid sample between two diamonds. Due to limited strength of these diamonds the maximum achievable pressure is limited to several megabars. Data obtained with this technique for lead are represented as the DAC curve in Figure 2.1.

Shock waves. In dynamic experiments, on the other hand, a shock wave is launched in a sample that leads to irreversible heating of matter, thereby generating HED states. In this type of experiments, parameters like shock speed and particle flow velocity are measured and the EOS of the material is deduced from this information. It is to note that typical shock-wave measurements are not complete in the thermodynamic sense, because a temperature measurement is essential for obtaining complete EOS information and for calculating first and second derivatives such as heat capacity or sound velocity. In general, EOS data measured

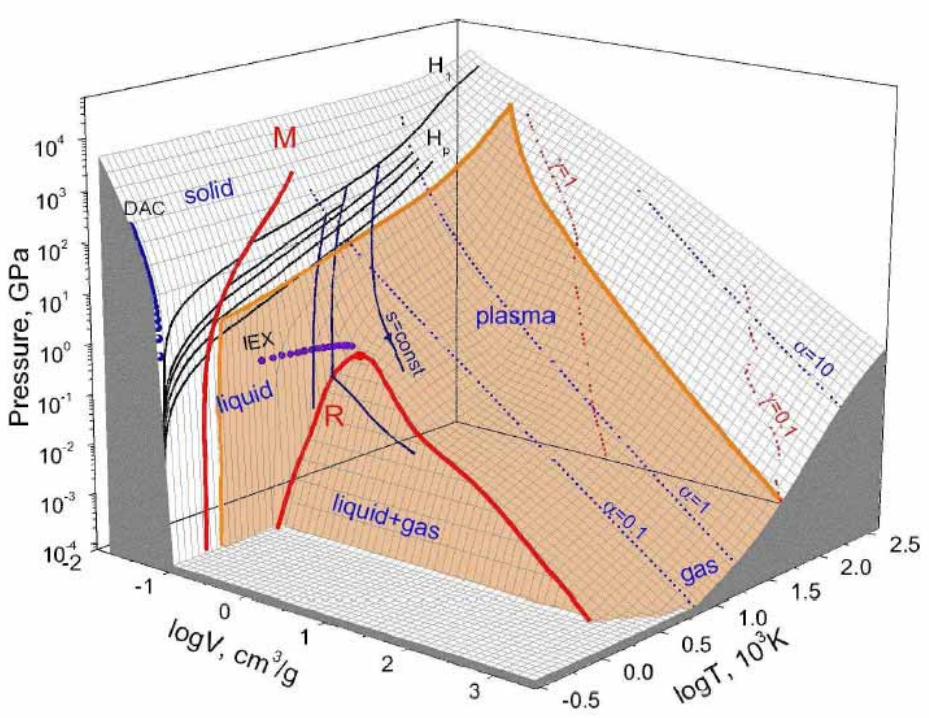

Figure 2.1: Equation-of-state surface for lead in P-V-T variables (logarithmic scale). M — melting region, H — principal and porous Hugoniots, DAC — diamond anvil cells data, IEX — isobaric expansion data, S — release isentropes, R — boundary of two-phase liquid-gas region with the critical point, isolines of ionization degree α and plasma non-ideality parameter γ.

in shock experiments are always limited to the regions of principal and porous Hugoniot (H and H_p curves in Figure 2.1).

Shocks can be generated by high explosives, powerful lasers, underground nuclear explosions, Z-pinches, two-stage light gas guns, rail guns and magnetic compression devices. These techniques have allowed one to study thermodynamical properties as well as electric conductivity and opacity along shock adiabats for different states, including the hot compressed phase and strongly coupled plasma. Available experimental data, obtained by the shock wave technique for various metals extend over nine orders of magnitude with respect to pressure.

Chemical explosives have been used to create shock waves in metals up to about 10 Mbar and temperatures of the order of 10^4 K [4,5]. Higher pressures of tens of megabars have been accessed by spherical cumulative systems [6,7] and by underground nuclear explosions [8,9]. Recent laser-driven and pulsed-power-driven compression experiments provided new data on the EOS of hydrogen and its isotopes at pressures $>$ 1 Mbar [10]. An extension of the studied regions of the phase diagram to larger relative volumes in comparison to the principal Hugoniot can be achieved by investigating shock compressibility of porous samples [11].

Isobaric expansion technique (IEX). Another dynamic method of EOS study is the isobaric expansion technique [12]. In these experiments, a high current is discharged through a metal wire placed in a vessel with liquid or buffer gas under pressure. This method, in comparison to the shock wave one, is of practical significance, since thermodynamically complete EOS data are obtained by measuring pressure, temperature and volume. Due to limited

material strength of the pressure vessel and magnetic instabilities during discharge, the maximum pressure lies in the 10 kbar region and the temperature is of about 8000 K. Thus states of liquid metal up to the evaporation phase transition have been accessed (IEX curve in Figure 2.1).

Heavy Ion Heating and Expansion (HIHEX). During the past decade it was demonstrated by extensive theoretical and experimental work [13-20] that intense heavy ion beams are potentially an efficient tool to generate macroscopic volumes of HED matter with fairly uniform physical conditions. An additional advantage compared to some traditional methods, like IEX and DAC, is that there is no limitation to specific type of target material, hence any material of interest, like minerals or oxides, can be studied.

Extensive experimental work has been carried out since 2003 at the Plasma Physics group of Gesellschaft für Schwerionenforschung-Darmstadt (GSI). In particular the "Heavy Ion Heating and Expansion" experimental concept (HIHEX) has been employed and studied [21].

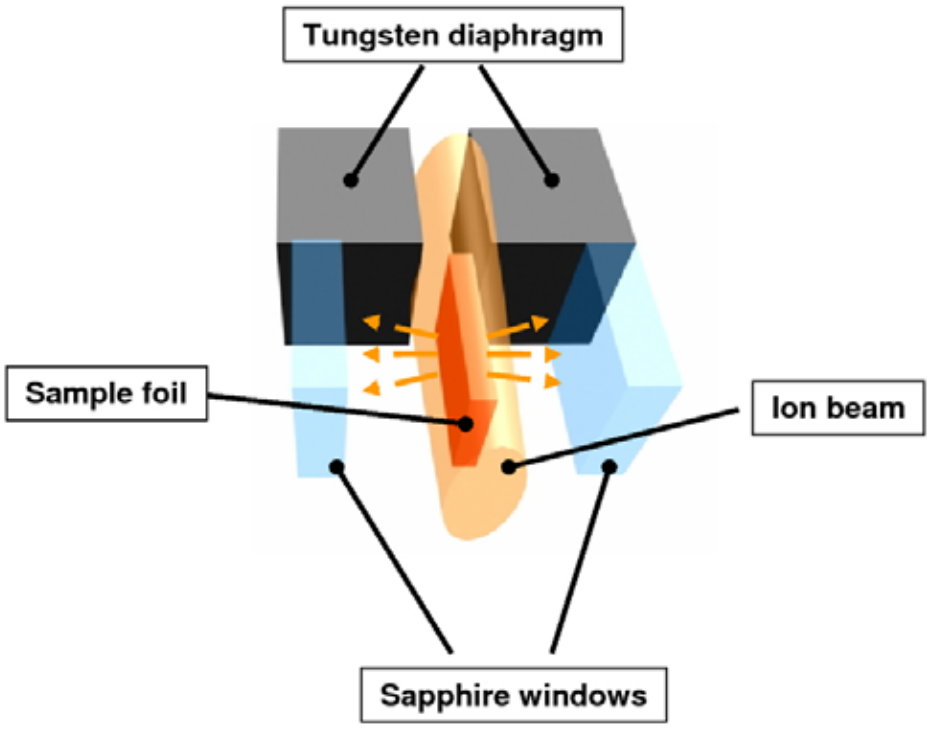

Figure 2.2: The HIHEX beam-target design of HED physics experiments with heavy ion beams.

The main idea of the HIHEX experiment, in contrast to shock wave experiments, is to exploit the intrinsic feature of heavy ions: the volumetric character of heating. A macroscopic volume of the sample material is heated by the heavy ion beam uniformly and quasi-isochorically, thereby generating HED states. The heated material will then expand quasi-isentropically, passing through many interesting physical states. The expansion of the target material can be limited by a surrounding container that can also be filled with a buffer gas at different initial pressures. Measurements of the target physical properties are performed during the heating, as well as during the expansion phase. Figure 2.2 shows the concept of the HIHEX experiment configuration using one-dimensional plane geometry. In this case a thin foil of a target material is placed along the ion beam and in order to optimize the specific

energy deposition, a beam with an elliptic focal spot is used. The width of the beam is larger that the foil thickness and the ion range is longer than the foil length. These conditions allow uniform heating of the sample and such a beam-target configuration leads to a quasi one-dimensional target expansion. The two plates of transparent material placed on either side of the foil act as walls that confine and homogenize the expanding target material. With present beam parameters at GSI, the level of specific energy deposition in solid lead is about 1 kJ/g that allows generation of HED states at solid state densities with temperatures up to 12000 K and pressures in the kbar range.

A new heavy ion accelerator facility, the Facility for Antiproton and ion research (FAIR), is being designed and constructed at GSI [22]. At FAIR, one expects the specific energy deposition of 200 kJ/g in solid lead, leading to generation of HED states including hot liquid states, the critical point region, the two-phase liquid-gas region and strongly coupled plasmas [23]. The colored surface in Figure 2.1 represents HED states that can be accessed in case of lead with this future machine.

2.2 Methods of temperature measurements

Temperature is one of the key thermodynamical parameters to be determined in the experimental EOS studies of HED states. It is a great challenge to measure temperature in dynamic HED physics experiments, where important processes are happening at the sub-microsecond time scale. Only non-contact and non-intrusive techniques can be applied in this case. Below, several such techniques are briefly introduced.

2.2.1 Existing methods for temperature measurements

Resonance neutron scattering. By adding to the sample a small amount of a certain dopant with known neutron scattering cross section, the temperature of the sample can be deduced from the analysis of the resonance scattering of neutrons at these dopants. The main advantage of this technique is that temperature of interior of the sample can be measured. Employing this technique, temperatures of non-transparent shocked samples, starting from 800 K, have been measured [24]. The main difficulty arising in these experiments is the availability of an intense neutron source, necessity of homogeneous spatial distribution of temperature inside of a target and manufacturing of the doped samples.

Thomson scattering. Temperature measurement in the 100 eV region has been successfully demonstrated by analyzing the Thomson scattering of X-ray beam [25]. In these experiments, both electron and ion temperatures of strongly coupled plasma were determined by monitoring the Doppler shift and broadening of Thompson scattered high energy photons. This method is restricted to extremely high temperatures where the Doppler shift is big enough to be detected by existing equipment. The main problems in this technique are preheating of the sample by the probing X-ray beam and the need for an extremely intense X-ray source that can be generated, for examples, by a petawatt laser system.

Optical pyrometry. The optical pyrometry technique is an alternative method for temperature measurement and has been used in the work presented in this thesis. A pyrometer is a non-contact thermometer, which measures the temperature of an optically thick body based on its emitted thermal radiation, while no disturbance of the existing temperature field occurs.

In pyrometry, the most important radiation wavelengths belong to the visible and infrared radiation bands allowing temperature measurements in the range from 300 K to 100000 K. Usually pyrometers are calibrated absolutely, which also enables them to be used as absolutely calibrated spectrometers. Since the light absorption in optically thick bodies is very strong, only temperature of a surface can be measured.

Pyrometric temperature measurement problems of industrial or scientific interest are often limited by the lack of knowledge of the spectral emissivity of the sample, which depends on temperature and a wavelength. Emissivity is the main issue of the optical pyrometry because it is very difficult to measure it and without its knowledge, except of special cases like black body radiation, temperature will be determined with relatively high error.

2.2.2 Pyrometric temperature measurement.

Figure 2.3: First pyrometric temperature measurement. The simplest and oldest non-contact way of estimating the temperature of a radiating body is by observing its color.

All bodies at non-zero absolute temperature emit electromagnetic radiation. There are three different fundamental radiation processes that continuously take place in a medium, namely, absorption, spontaneous emission and stimulated emission of electromagnetic radiation. The total amount as well as its spectral distribution is determined by the temperature of the body. According to quantum statistic, energy density, $U(\nu)$, of electromagnetic radiation of frequency ν in 1 cm^3 in the thermodynamical equilibrium is described by the Planck distribution

$$U(\lambda) = \frac{8\pi h\nu^3}{c^3} \cdot \frac{1}{e^{\frac{h\nu}{kT}} - 1}.$$

Photons emitted by a surface of an optically thick body originate from a thin radiation layer close to the surface as it is shown in Figure 2.4. The size, d, of the radiative layer is determined by the expression

$$\tau(\lambda) = \int_0^d \kappa(x, \lambda)dx \approx 1,$$

where $\tau(\lambda)$ is optical thickness and $\kappa(x, \lambda)$ is the absorption coefficient of the medium at wavelength λ. Since an absorption coefficient depends on a wavelength, d also depends on

wavelength. In a conducting material under normal conditions, the size of the radiative layer is approximately one tenth of the corresponding wavelength [26]. Temperature of the interior

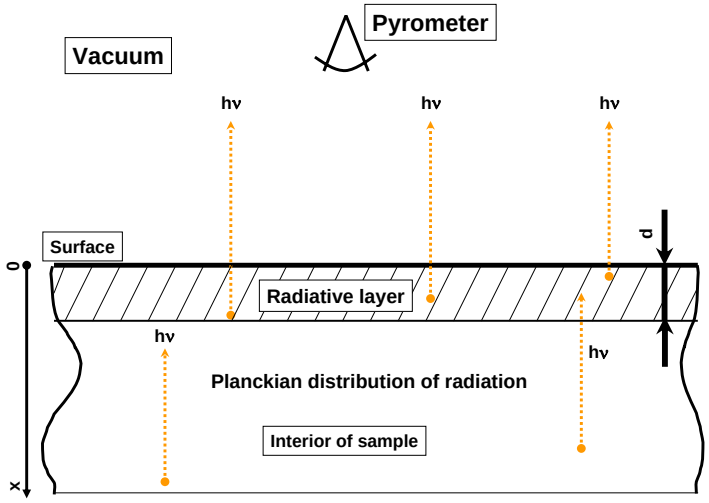

Figure 2.4: Surface radiation of an optically thick body with uniform temperature distribution. Photons detected by the pyrometer are emitted in a thin radiative layer.

(below the radiative layer) cannot be measured, since photons that are emitted in the inner region are absorbed completely before they reach the surface. This is the main limitation of the optical pyrometry technique: only temperature of a thin radiative layer, i.e. of a surface can be determined.

As long as there is a uniform temperature distribution a pyrometer will measure the same temperature at all wavelengths. If this is not the case, for example the temperature of the interior of a body is higher than that of the surface, the measured temperature will become wavelength dependent.

In the example shown in Figure 2.5, a pyrometer detects average temperatures of radiative layers of length X_1, X_2 and X_3. Optical thicknesses at wavelengths λ_1, λ_2 and λ_3 are the same and equal to 1, whereas the physical thicknesses X_1, X_2, X_3 are different. As there is the temperature gradient T(X), the pyrometer will detect different effective temperatures at different wavelengths. Nevertheless, if the temperature gradient at the surface is small, the difference in effective temperature will be negligible. In optically thick object this is true, since the value of thickness X_i is several tenths of nanometers and on such a short length scale, temperature can be considered to be constant.

A strong non-uniform temperature distribution arises when a melted or evaporated material expands to vacuum (Figure 2.6). This happens, for example, during the release of a shocked metal, after a shock wave reaches the free surface.

In general an evaporated metal can be treated to a good approximation as a single-atom gas. Optical properties of such a metallic gas have been studied in detail in the reference [11]. It was shown that absorption of visible light of such a gas strongly depends on temperature, i.e. it increases rapidly with increasing temperature, whereas metal vapor is transparent.

During the release process, the front of the release wave is in a gaseous state, with pressure and density at the boundary with vacuum being equal to zero. Temperature at this point is very low and as a consequence the expansion front is optically transparent. In opposite, in

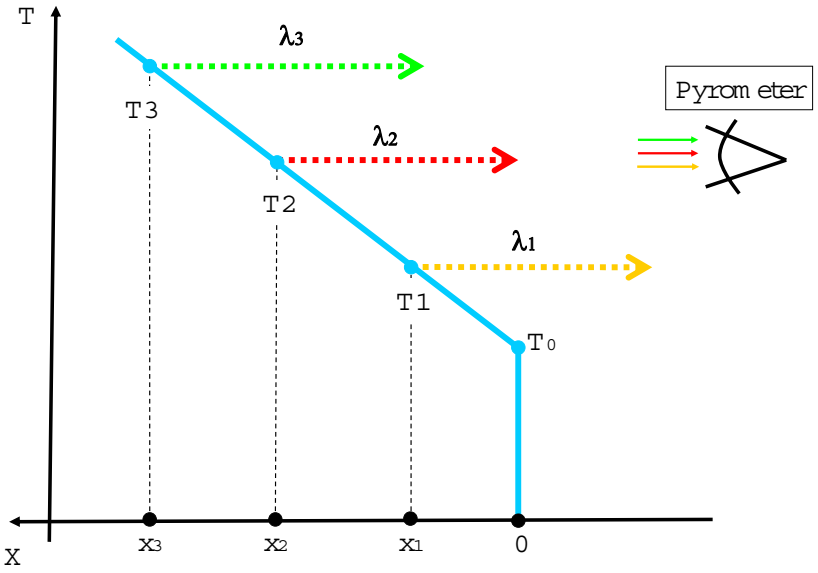

Figure 2.5: Radiation of a body with temperature decreasing towards the surface (blue line – temperature profile). Photons for which the absorption is high are emitted in layers close to surface, while less absorbable photons are emitted in deeper, hotter layers.

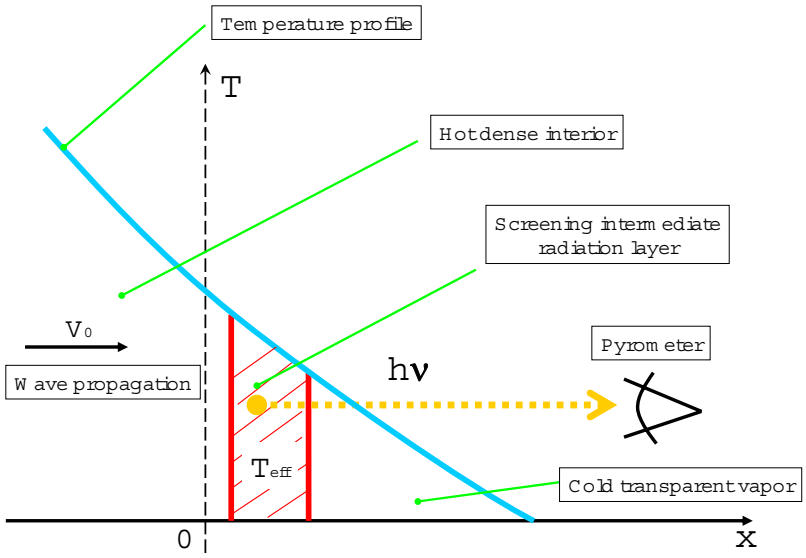

Figure 2.6: Thermal radiation in a release wave. Hot interior is screened by opaque gas. The pyrometer measures temperature of some effective radiation layer.

deeper dense layers, where temperature is higher, the material is non-transparent and becomes the main source of radiation. As the result, the pyrometer detects photons that are emitted in an intermediate radiation layer (the hatched region in Figure 2.6) and measures effective temperature corresponding to this layer.

With time, the release wave embraces a bigger volume, while the geometrical and optical

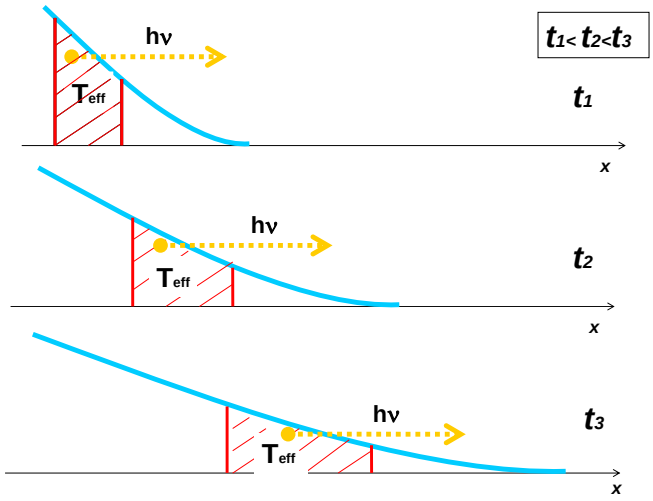

Figure 2.7: Shift and broadening of radiative layer in a release wave at different moments of time.

width of the radiation layer continuously increases and moves to the region with lower temperature, as it is schematically shown in Figure 2.7. In the case of plane isentropic expansion, effective temperature will decrease logarithmically with the time t [11]

$$T_{\text{eff}} = \frac{\text{const}}{\ln(t) + \text{const}}.$$

As it was shown above, the radiation inside of a body, in particular in the radiative layer, has the Planck distribution. However, not all photons emitted in the radiative layer will leave the body. Some of them will be reflected from the body-vacuum interface back to the interior. The reflection occurs due to difference in refraction indexes between the material and surrounding media and is governed by the Fresnel formulas [26]. As the result, the spectral density distribution irradiated by the surface is less than or equal to the Planck distribution.

Generally, a surface radiation is represented as equilibrium Planck or a black-body radiation, R_{lanck}, multiplied by spectral emissivity, ϵ

$$R(\lambda, T, \Omega) = \epsilon(\lambda, T, \Omega) \cdot R_{\text{Planck}}(\lambda, T) = \epsilon(\lambda, T, \Omega) \cdot \frac{C_1}{\lambda^5} \cdot \frac{1}{e^{\frac{C_2}{\lambda T}} - 1}.$$

Here, R is the energy flux, which is radiated per second per unit area into one steradian at the observation angle, Ω, wavelength λ, while C_1 and C_2 respectively are the first and the second radiation constants $C_1 = 1.191083 \cdot 10^{-16}\text{W} \cdot \text{ m}^2 \cdot \text{Sr}^{-1}$ and $C_2 = 1.4389 \cdot 10^{-2}\text{m} \cdot \text{K}$. Formally, ϵ is defined as

$$\epsilon(\lambda, T, \Omega) = \frac{R(\lambda, T, \Omega)}{R_{\text{Planck}}(\lambda, T)} \leq 1.$$

This relation shows the deviation from black body radiation at the same temperature and wavelength. Spectral emissivity of a surface is ideally a function of optical parameters of the material, like refraction and extinction coefficients. In reality, it is in addition strongly influenced by intrinsic surface characteristics such as surface roughness and presence of absorbing and non-absorbing overlayers such as oxides and nitrides. For most clean metals the

emissivity is low, with a value of about 0.1 to 0.4. Generally, spectral emissivity of metals decreases with decrease in temperature and is higher at shorter wavelengths.

Surface temperature of an optically thick body is often described by brightness temperature that is temperature of an ideal black body with the same surface radiation in a given part of the spectrum. This "effective" temperature is indeed wavelength dependent and only in the case of an ideal black body it is the same for all wavelengths and equals to physical temperature.

The main problem in surface temperature measurements using pyrometry is the necessity to know the spectral emissivity. In solid and liquid states, several trends of thought exist on the best approach to minimize this emissivity problem.

The most accurate one available to obtain the spectral emissivity of a solid material is to compare the radiance from the material of interest to a black body at the same temperature. This is practically realized by including a black body hole in the sample of interest and comparing the radiation from the surface with that from the black body hole. This method has been widely practiced and is considered the standard method by which emissivity data of solid materials may be derived [27]. However, one of the serious drawbacks of this approach is that the sample of interest may be too small or inaccessible for the inclusion of a black body hole. Moreover this technique is limited to the solid phase.

Another method for the determination of normal spectral emissivity[1] is the application of an integrating-sphere reflectometer [27]. This method uses a high-speed version of an integrating sphere reflectometer of the comparison type, in which the reflectivity of the sample, which undergoes heating, is measured in relation to the known reflectivity of a barium sulphate reference sample. A modulated laser beam strikes the side of a sample facing the sphere and the reflected beam is collected hemispherically. A fast lock-in technique is used to discriminate between the reflected laser radiation and the continuous thermal component emitted by the sample itself, when it reaches high temperatures. One of the disadvantages of this technique is that the entire integrating sphere setup is rather big and must be placed in the vicinity of the hot sample. Another drawback is low temporal resolution of the measurement, since the fastet lock-in system work on the millisecond time scale.

The ellipsometric technique is another method to measure emissivity [28]. By measuring the change of the polarization of laser light reflected from a sample and applying methods of ellipsometry, normal spectral emissivity can be derived. A polarization state is measured by a division-of-amplitude-photopolarimeter, whose output are the four Stokes vectors. The probing light should be modulated and decoded by a lock-in amplifier. Similarly to the integrating sphere technique, the main disadvantage of this method is the poor temporal resolution.

Above approaches suffer from the problems of complexity, low speed and high cost, but are generally very accurate. Meanwhile, there is another efficient way to measure temperature and minimize the influence of the surface emissivity effect.

Multi-wavelength pyrometry tries to determine both, temperature and emissivity simultaneously by measuring the spectral radiance of a surface at several wavelengths. Since in this case there are always N measured values and $N + 1$ unknowns (emissivity at N wavelengths and temperature), a mathematical relation $\epsilon = f(\lambda)$ of emissivity to wavelength must be assumed in order to determine the true temperature. The problem here is that one needs to know this function.

If the analytical formula of emissivity is known, then the multi-wavelength pyrometry

[1]Normal emissivity is emissivity which is observed normally to the surface

technique allows the temperature determination with an error less than one percent [29]. However if no crude estimation of emissivity is available at all, then the emissivity function is traditionally represented as a polynomial of power n, $\epsilon(\lambda) = P^{\mathrm{n}}(\lambda)$ with respect to the wavelengths. As it was shown in [30], temperature in this case can be measured with an error up to 20 percent.

Usually, qualitative behavior of the emissivity in solid and cold liquid states is influenced equally by surface conditions and optical constants of matter, whereas in hot dense liquid and gaseous states, emissivity is governed mainly by optical constants of the material. A general theoretical representation of emissivity, which would take into account contamination layers and all optical peculiarities of a given material, is not trivial and it cannot be considered in the frame of this work. On the other hand, the multi-channel property of the pyrometer gives a possibility for validating different theoretical models of emissivity.

In the following, a qualitative theory of normal emissivity for metals is reviewed, since in the work presented in this thesis, only metals are studied and it is considered that emissivity is determined by the optical properties of the material only. This means that the surface is ideally smooth and clean. For the sake of simplicity, a homogenous spatial distribution of temperature is considered.

For an optically thick (opaque) body in thermal equilibrium emissivity, ϵ, is related to surface reflectivity, r, as

$$\epsilon = 1 - r.$$

Optical parameters of a conducting medium can be deduced (see for example [26]) from an imaginary dielectric function, $\hat{\varepsilon}$ that arises in Maxwell equations when they are applied to a conductor as

$$\hat{\varepsilon} = \varepsilon + i\frac{4\pi\sigma(\omega)}{\omega} = \varepsilon_1 + i\varepsilon_2,$$

where $\sigma(\omega)$ is the AC conductivity of the medium. The refraction index, n, and extinction coefficient, k, are related to $\hat{\varepsilon}$ by $\varepsilon_1 = n^2 - k^2$, $\varepsilon_2 = 2nk$. The normal spectral emissivity is calculated from n and k via the Fresnel relation and Kirchhoff's law as follows:

$$\epsilon(\lambda) = \frac{4n}{[(n+1)^2 + k^2]},$$

It is seen that emissivity is strongly determined by the electrical conductivity of the medium, and once the conductivity law is known, all optical properties can be obtained easily.

For a rough estimation of emissivity, the classical theory of conductivity proposed by Paul Drude in 1890 may be used [31]. In his free-electron theory, the electrons are accelerated by the electric field of radiation and damped by collisions with the lattice [31], leading to the relation

$$\sigma(\omega) = \frac{\sigma_0}{1 + i\omega\tau},$$

where σ_0 is the DC conductivity and τ is the average time between collisions. After the substitution of the Drude's expression to above formulae, the optical behavior of such an ideal metal falls naturally into three main regions of the spectrum. For each of these regions, useful approximations of emissivity can be made depending on the relation of the wavelength λ to critical parameters, λ_p and λ_τ (wavelengths corresponding to plasma frequency ω_p and $\omega_\tau = 1/\tau$ respectively) [32].

For short wavelengths, $\lambda < \lambda_p$, in the so-called region of transparency one obtains

$$\epsilon(\lambda) \approx 1 - \frac{1}{16}(\frac{\lambda}{\lambda_p})^4.$$

In the intermediate region, $\lambda_p < \lambda < \lambda_p^2/\lambda_\tau$, emissivity is essentially constant and equal to

$$\epsilon \approx \frac{\lambda_\tau}{\lambda_p}.$$

In the infra-red region, $\lambda > \lambda_p^2/\lambda_\tau$, ϵ is expressed in the more familiar form

$$\epsilon(\lambda) \approx 2\sqrt{\frac{c}{\sigma_o \lambda}}.$$

The last expression is the Hagen-Rubens or Drude relation, the validity of which has been the subject of many experimental investigations and finally, a fair agreement with the theory has been found [33]. However, the most important consequence is the appearance of the intermediate region for the commonly adopted model of an ideal metal.

According to conditions relevant to this work, $\lambda_p \approx 400$ nm and $\lambda_p^2/\lambda_\tau \approx 2000$ nm. This shows that there exists a wide range of wavelengths, extending from the visible region up to the near-infra-red region over which the emissivity to a good approximation, is constant. Radiation that exhibits this kind of emissivity behavior is called grey body radiation. This approximation is widely used in metallurgy, when applied to liquid metals [34]. Grey emissivity is also valid in case of several highly reflective solid metals metals like polished aluminium and silver [34]. Reflectivity from 500 to 1500 nm changes there only by few percents).

It is to be noted that grey body radiation follows from the simplest model of conductivity that does not take into account the contribution of bound electrons and peculiarities of the conductivity band structure. A precise model of emissivity that considers all these features and is also applicable in a broad range of temperatures is not trivial. This becomes obvious from the fact that the ionization degree (i.e. number of free charges) of the sample being heated from room temperature to 10000 K according to the Saha ionization formula will increase by the factor of 50 [11], not to mention the complete change in the conductivity band structure during the melting and evaporation of the sample.

Meanwhile, there are special cases when the simple grey body approach may be justified. For example, the contribution of the specific conductive band is simplified for a liquid phase where a disordered state washes out much of the band structure and optical properties can be fitted remarkably well to the simple Drude model [35]. The grey model also seems to be applicable in the the density region around 1 g/cm^3. Such states appear for example during the release of a shocked metal. As it was shown in [35], at this density value the electronic structure is simple enough to be described by the Drude approximation. However more sophisticated frequency-dependent description that takes into account some of the emerging electronic structure, as the density increases, is necessary.

Taking above consideration into account, two empirical models of emissivity were used in this work for the temperature determination. These models are traditionally used in pyrometric temperature measurements where no information about surface emissivity is available [37]. The first one is the grey body approach, as it is specifically justified for liquid and release states of HED matter. The second model assumes a linear law of emissivity, which can be treated as a modified grey model with a linear term added. The linear model incorporates

also black and grey body cases and is a good approximation to some solid metals like tungsten (see Figure A.3 in Appendix).

By increasing number of wavelengths one could in principle use a polynomial of a higher order. However, as it is proved in [29], higher orders are useless since they may lead even to a bigger error due to overfitting, i.e. the increase in number of wavelengths (and orders of a polynomial) will not improve accuracy of the temperature determination. Traditionally, the number of channels used in multi-wavelength pyrometers was not exceeding six [37].

2.3 High energy density matter generated by intense heavy ion beam

An interaction of an intense heavy ion beam with matter is reviewed in detail in [38] and thermodynamical behavior of loaded medium is discussed in [11, 14].

Energy balance. When a sample is irradiated by an intense ion beam, kinetic energy of projectiles is transformed into thermal energy of the target material. Simultaneously with this increase of internal energy, there are three energy dissipation mechanisms : hydrodynamic motion, heat conduction and thermal radiation [11].

The energy balance for an elementary volume dV is given by

$$\frac{\partial \epsilon}{\partial t} = P_{\text{ion}} - P\frac{\partial V}{\partial t} - S_{\text{thermal}} - S_{\text{radiation}}.$$

Here, ϵ is the specific internal energy; P_{ion} is specific energy power deposition of an ion bunch; $P\frac{\partial V}{\partial t}$ is the energy reduction rate due to work done by the heated media as a result of hydrodynamical expansion; S_{thermal} is energy loss rate due to thermal conductivity; $S_{\text{radiation}}$ is energy loss rate due to electromagnetic radiation.

Dissipation processes. Depending on the thermodynamic state of the sample, various dissipation mechanisms become dominant. For example, if the sample is completely evaporated, the main energy dissipation mechanism is the work that the loaded medium performs during expansion. Whereas, if a sample is in a liquid state, following two competing mechanism of energy loss become significant.

In the first one, the energy is taken away by the molecules of a sample being continuously evaporated by the surface. The liquid-vapor phase tends to achieve equilibrium, which occurs when a vapor becomes saturated. Since this process happens in vacuum, no such saturation can take place. Therefore, cooling of a liquid in vacuum is a non-equilibrium process and its description requires use of molecular dynamics, which cannot be considered in the frame of this work.

The second dissipation mechanism is cooling of a sample by photons emitted from the surface (this mechanism is also dominant in solid states). The energy loss due to radiation may be evaluated rather easily [11]. This can be done by treating an idealized problem with a target geometry and material properties close to the experimental ones.

For an optically thick object, energy is lost from a thin (radiative) layer next to the surface. Electromagnetic radiation emitted in the bulk is reabsorbed immediately and thus remains in the system. The energy dissipation rate induced by thermal radiation is governed by the following energy balance equation

$$C \cdot dT = -2\left(\sigma T^4 \cdot S \cdot 2\pi \cdot dt\right).$$

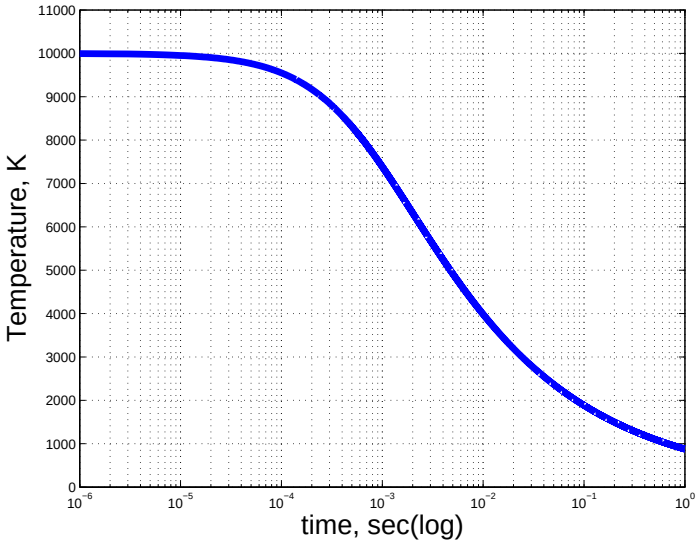

Figure 2.8: Cooling of a sample by thermal radiation. The estimation is done for a sample with material geometry and properties close to those used in experiments.

The left side of the expression is the change in the internal energy and the right one is power dissipated by a black body with surface S to spatial angle 2π. The factor 2 in front of brackets takes into account both sides of the target foil, σ is the Boltzman constant. The molar heat capacity C in this simplified evaluation was taken $3R$.

Figure 2.8 shows the numerical solution of the above equation, where it is seen than the rate of cooling strongly depends on temperature: the lower the temperature, the slower the dissipation rate. In particular, if processes at a microsecond time scale are observed, losses due to thermal radiation can be neglected. For a body with emissivity less than one, the cooling rate will be correspondingly lower.

The specific deposition power of an ion beam is given by

$$P_{\text{ion}} = \frac{\partial}{\partial t}\left(\frac{dE}{dx}\cdot\frac{N(t)}{\rho A}\right),$$

where $\frac{dE}{dx}$ is the energy loss of a single ion, N is number of ions, ρ is density and A is the irradiated surface.

Energy deposition of heavy ion beams. The energy loss of projectile particles to target electrons may be separated into two parts, namely, energy loss due to bound electrons and the energy loss due to free electrons. The first process is called cold stopping, whereas the latter is important when slowing down of an ion beam takes place in a pre-ionized (hot) material. In this work, cold stopping is the major energy deposition mechanism, which is a valid approximation since the target temperature is relatively low. The projectile interacts with the medium via the Coulomb force with the electrons and protons and via the strong nuclear force with the nuclei of the absorber. At the ion energy below 1 AGeV that is used for high energy-density physics applications, nuclear force can be disregarded. The projectile slows down by losing energy to the atoms of the absorbing medium. The electrons take an appreciable amount of energy from the heavy projectile without causing significant deflection, while the nuclei absorb very little energy. However, due to their greater charge, the nuclei cause scattering of the incident particle. Thus energy loss of the projectile occurs in collisions

with the target electrons.

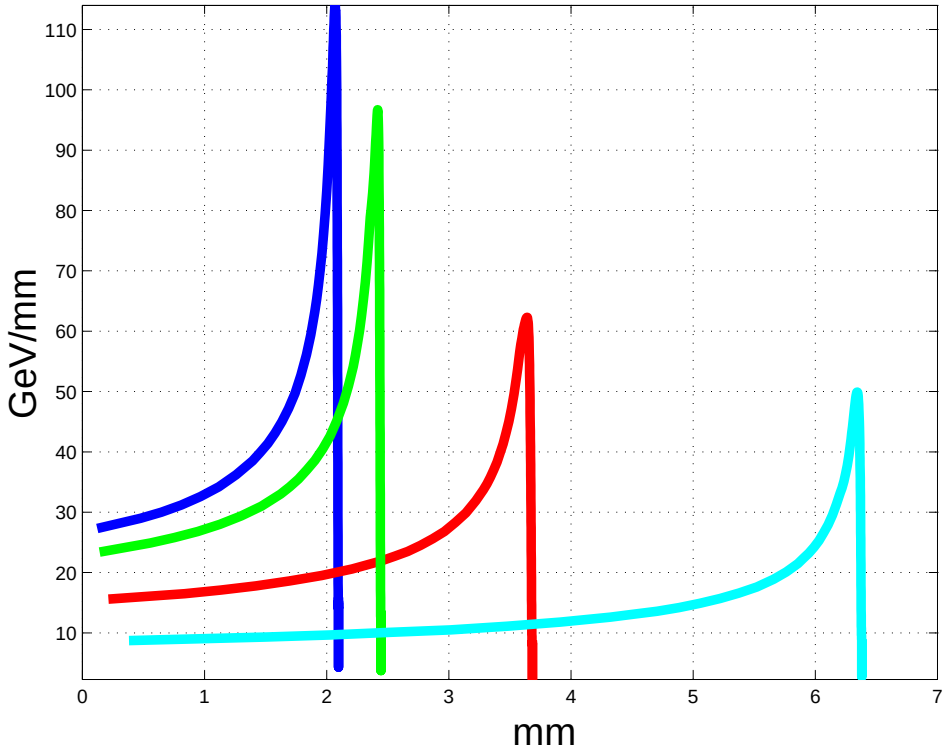

Figure 2.9: Energy deposition (Bragg curves) of an uranium ion with initial energy $E_0 = 350$ AMeV in various materials. Blue — tungsten, green — tantalum, red — lead and cyan — sapphire (Al_2O_3).

For the near solid densities, the electron temperature relaxation occurs after 1 ps and thermalization between electrons and ions will occur in less than 1 ns. The energy deposition in the performed experiments occurs within 120 ns (see more details below) and thus it can be assumed that the deposition takes place locally and instantaneously.

The overall form of an expression describing the electronic energy loss of an ion in a medium can be obtained from classical arguments and in SI units the expression for stopping power S can be written as:

$$-\frac{dE}{dx} = S = \frac{e^4}{4\pi\epsilon_0^2}\frac{\bar{Z}_p^2 n_e^{\text{bound}}}{m_e v^2}\zeta.$$

Here $\bar{Z}_p$ is the effective charge of the projectile ion, v is ion velocity, m_e and n_e^{bound} are the electron mass and number density of bound electrons, respectively and ζ is the stopping logarithm.

In Figure 2.9 is shown energy deposition of the uranium beam with initial energy 350 AMeV for differen materials. As it is seen from this figure, there is a distance along which energy deposition is quasi-uniform that ends with a peak called the Bragg peak. Due to the presence of the quasi-uniform part, it is possible to have uniform energy deposition. However, the Bragg curve shown in Figure 2.9 is idealized. In practice, a Bragg peak is broader. The broadening occurs due to the fragmentation of a uranium ion to lighter ion species, straggling

and scattering of ions [38]. For the exact calculation of the energy deposition of an entire ion bunch in the volume of a sample, in addition to above mentioned effects, three dimensional features like the non-parallel convergence of ions and elliptical shape of focal spot must also be considered.

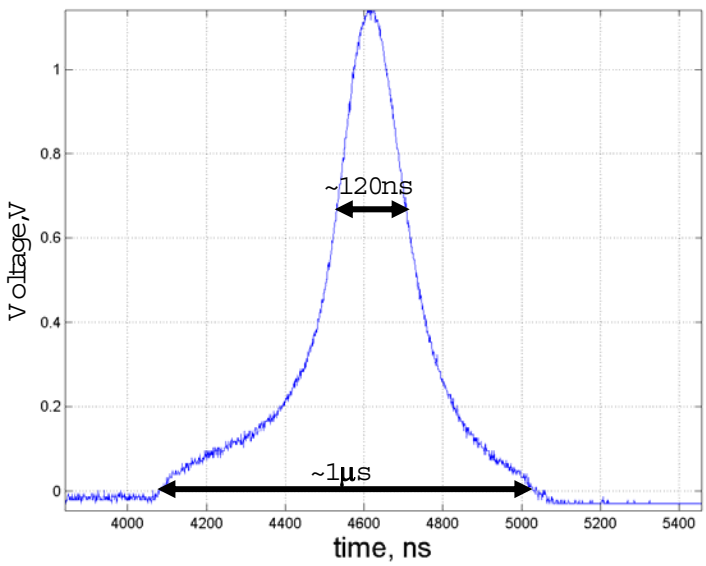

Figure 2.10: Temporal dependence of intensity of a uranium beam recorded by a fast current transformer.

Energy deposition rate. Figure 2.10 shows a typical experimental record of a fast current transformer (FCT), which records temporal intensity of an ion beam. It is seen that approximately 80% of the bunch energy is deposited within 120 ns. The narrow peak sits on a microsecond long plateau, which preheats a target. This plateau is an inherent feature of acceleration of an ion bunch in a synchrotron and cannot be removed completely.

Considering the thickness 0.2 mm of a target (typical thickness used in performed experiments) and a rough estimate of sound velocity, 3 km/s, it can be estimated that approximately after $\tau = \frac{0.2 \text{ mm}}{3 \text{ km/s}} \approx 60$ ns, deposited energy will redistribute in the bulk volume and the sample will start to respond hydrodynamically, i.e. expand. This estimation is based on the fact that this process cannot propagate faster than the speed of sound. τ here is comparable with the time duration of the ion beam, FWHM=120 ns, which means that heating in the experiments is "slow" and not shock-like. However, if one uses thinner foils and a smaller focal spot of the ion beam the energy deposition will approach the shock regime.

Phase states. During the course of the experiment, the sample passes through various phase states. Such processes can be schematically plotted on three-dimensional P-V-T (see Figure 2.1) or two-dimensional, T-P, P-T, T-V phase diagrams. In Figure 2.11 an example of such a phase diagram in P-T coordinates is shown with equilibrium solid, liquid and gaseous states. While crossing the phase-separating solid lines, a phase transition occurs. States of matter that correspond to this line have two co-existing phases in equilibrium. In particular, at the intersection of all three lines to the one common point (called the tripple point) all three phases are present. Figure 2.12 shows a phase diagram plotted in P-V coordinates for liquid and gaseous states having the transitional gas-liquid region in between. In comparison to P-T coordinates, the two-phase states in the P-V plane occupy a certain region.

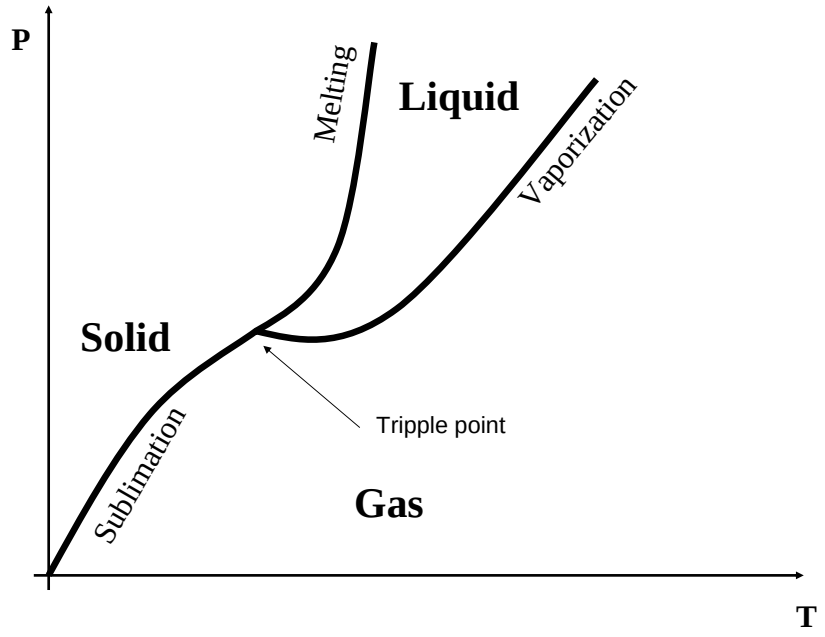

Figure 2.11: Phase diagram in P-T coordinates (shown schematically).

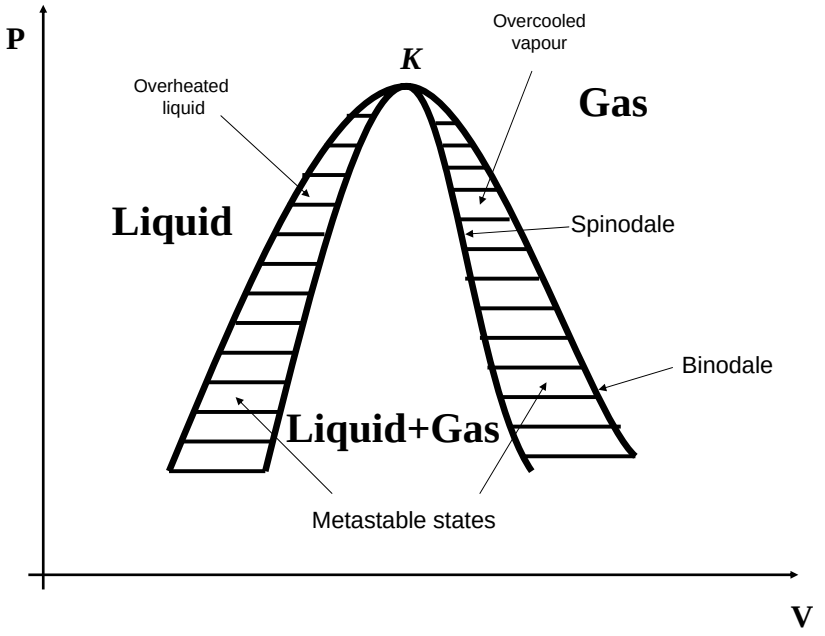

Figure 2.12: Phase diagram for liquid and vapor states in P-V coordinates (shown schematically).

The saturation curve, also called binodale, constrains the liquid-gas region. The left

hatched region represents liquid with bubbles and the right one vapor with liquid droplets. However, single-phase meta-stable states like overheated liquid at the left and overcooled at the right are also possible within the hatched region.

The meta-stable states may exist only till the spinodale curve, which constrains the region, where a single phase state cannot exist. Phase transition to the spinodale area occurs in an activation-free way: no energy is absorbed or released and no condensation or boiling centers are needed. Using high heating rates liquid metals can be superheated up to the spinodale line. Near the spinodale line, volume fluctuations begin with sudden growth of vapor nuclei in the superheated liquid. The area below spinodale line is unstable and therefore a "jump" into the right hatched region, the so-called phase explosion, with a large increase of volume will occur. Crossing the spinodale line causes a sharp increase in the electrical resistivity, as the conducting part of the sample is reduced. The rapid creation of vapor nuclei connected with a powerful expansion produces a shock wave in the surrounding medium. At that moment the surface temperature starts to decrease due to the cooling of the liquid phase, as it loses the more energetic atoms to the vapor phase.

The reason for the decreasing of temperature after reaching a maximum value could be distortions of the radiating surface, which are due to boiling, when the material is reaching the spinodale line at the given pressure [39].

The common point of spinodale and binodale is called the critical point. At this special point, material is in a very interesting state since the specific volume of liquid and gaseous state is the same and no difference between liquid and vapor exists anymore. This region of unstable states is least studied, and it is believed that with the help of intense heavy ion beams this new information will be obtained.

3 Experimental setup and methods

3.1 GSI accelerator facilities and the HHT experimental area

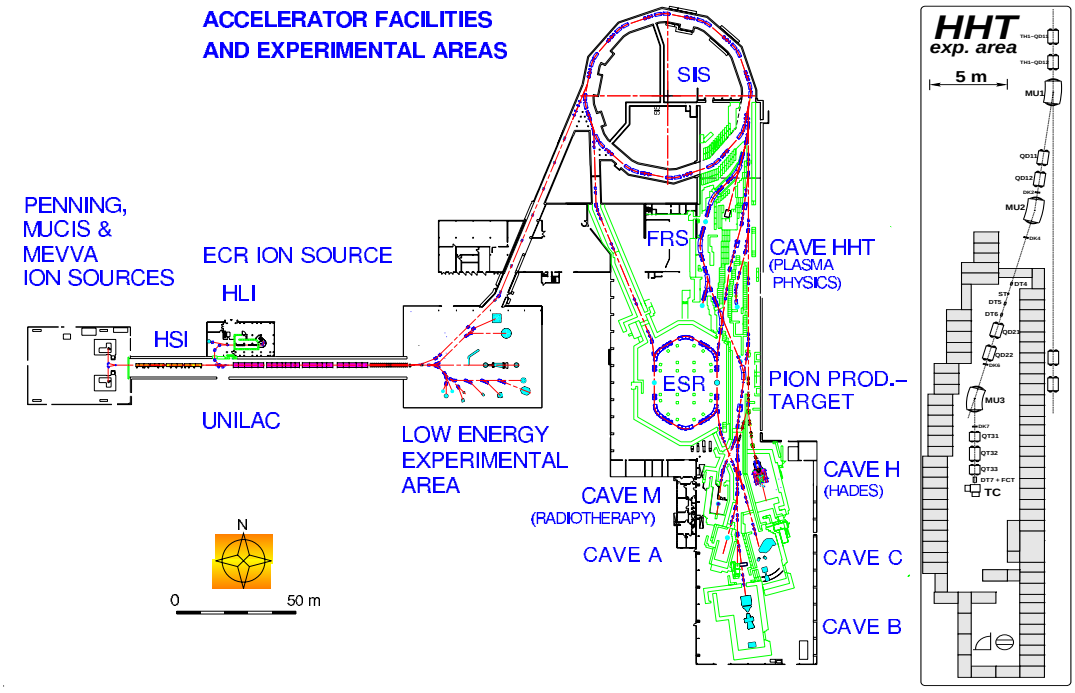

(a) GSI-accelerator facilities

(b) HHT area

Figure 3.1: GSI accelerator facilities and layout of the HHT experimental area.

GSI-Darmstadt is a unique accelerator facility worldwide where practically any nuclei of the periodic table of elements can be accelerated up to relativistic velocities on a routine basis. This accelerator facility offers a unique possibility for HEDP research with a heavy ion beam used as a driver. Intense beams of energetic heavy ions that are delivered by the heavy ion synchrotron SIS-18 are transported to the HHT ("High Temperature") experimental area (cave) and used to heat macroscopic volumes of solid density matter to extreme values of temperature and pressure. During the past three years, intense heavy ion beams of $^{238}U^{73+}$ with parameters shown in Table 3.1 were used to perform HEDP experiments at HHT.

Heavy ion beams are produced and pre-accelerated at the ion source area (see Figure 3.1a). Different types of ion sources including PIG (PennInG ion source), MEVVA (MEtal Vapour

Intensity:	Ion Energy:	Focal spot size:	Bunch duration (FWHM):
$(1-4.2)\cdot 10^9$/bunch	350 AMeV	$150\mu m - 1500\mu m$	120 ns-250 ns

Table 3.1: Parameters of the uranium ion beam used in recent experiments.

Vacuum Arc) and MUCIS (MUlti Cusp Ion Source) can be employed there and two different high-current ion sources can be used simultaneously. For the HEDP experiments at HHT, a source which provides the maximum current of a given ion species is preferable. The ions generated in an appropriate ion source are then accelerated in a linear accelerator UNILAC, (UNIversal Linear ACcelerator). UNILAC has two acceleration stages with different RFQ-accelerating structures optimized for the acceleration of high-current heavy ion beams. UNILAC can deliver beams of heavy ions of the energy from 1.4 AMeV to 20 AMeV. After acceleration, these beams can either be extracted for experiments at the "low energy" experimental hall or can be guided to the transfer channel to the SIS-18 synchrotron for further acceleration (see Figure 3.1a). A stripper installed inside the transfer channel allows increasing of the charge state of ions before injection into the synchrotron.

After acceleration in UNILAC, a heavy ion beam is injected into the synchrotron SIS-18 at the typical injection energy of about 11.4 AMeV per nucleon. In the synchrotron, which has a circumference of 216 m, maximum magnetic rigidity of 18 Tm, heavy ions can be accelerated up to 2 AGeV energy (1 AGeV for uranium ions).

To increase the beam intensity in the SIS-18 ring, a special "multi-multiturn" injection scheme can be used, where the ions are injected over several revolution periods and fill the entire transverse acceptance of the ring. The electron cooler installed in the ring reduces the transverse emittance of an ion beam. This takes place between successive multiturn injections from the UNILAC. Electron cooling increases the phase space density of the beam and therefore the number of particles that can be accumulated at a given acceptance of the synchrotron also increases.

Since acceleration in SIS-18 is performed at the fourth harmonics of the accelerating RF-field, the beam consists of four bunches. With the RF system that is presently available at the SIS-18 it is possible to reduce the duration of the ion beams down to 120 ns (FWHM) using the fast bunch rotation technique. After the acceleration in the SIS-18 synchrotron and rebunching, the beam is extracted and guided to the high energy experimental areas. For the experiments at the HHT, the fast extraction mode is required. In this mode, the entire beam is bent from its synchrotron orbit by a fast magnetic kicker ($\tau < 90$ ns) to an extraction channel. All particles are extracted within one revolution period. After the extraction from the synchrotron, the beam is transported to the target chamber.

The HHT experimental area (see Figure 3.2) is located in the high energy experimental hall ESR (see Figure 3.1). The area is shielded with massive concrete blocks and has all infrastructure necessary for performing experiments with high radioactive activation. Because of the radiation safety measures the area cannot be accessed during the experiments and several days after it and therefore all diagnostics and equipment are controlled from the HHT measuring room located 50 m away from the cave on the top of the concrete shielding.

Generation of HED states takes place in a vacuum target chamber separated from the beam-line via a 150 μm thick aluminium entrance window. The chamber can be evacuated down to 10^{-6} mbar or it can be filled with a gas, (typically Ar or He) with pressure up to 2 bar. It has bottom, up and side observation windows made from optical grade

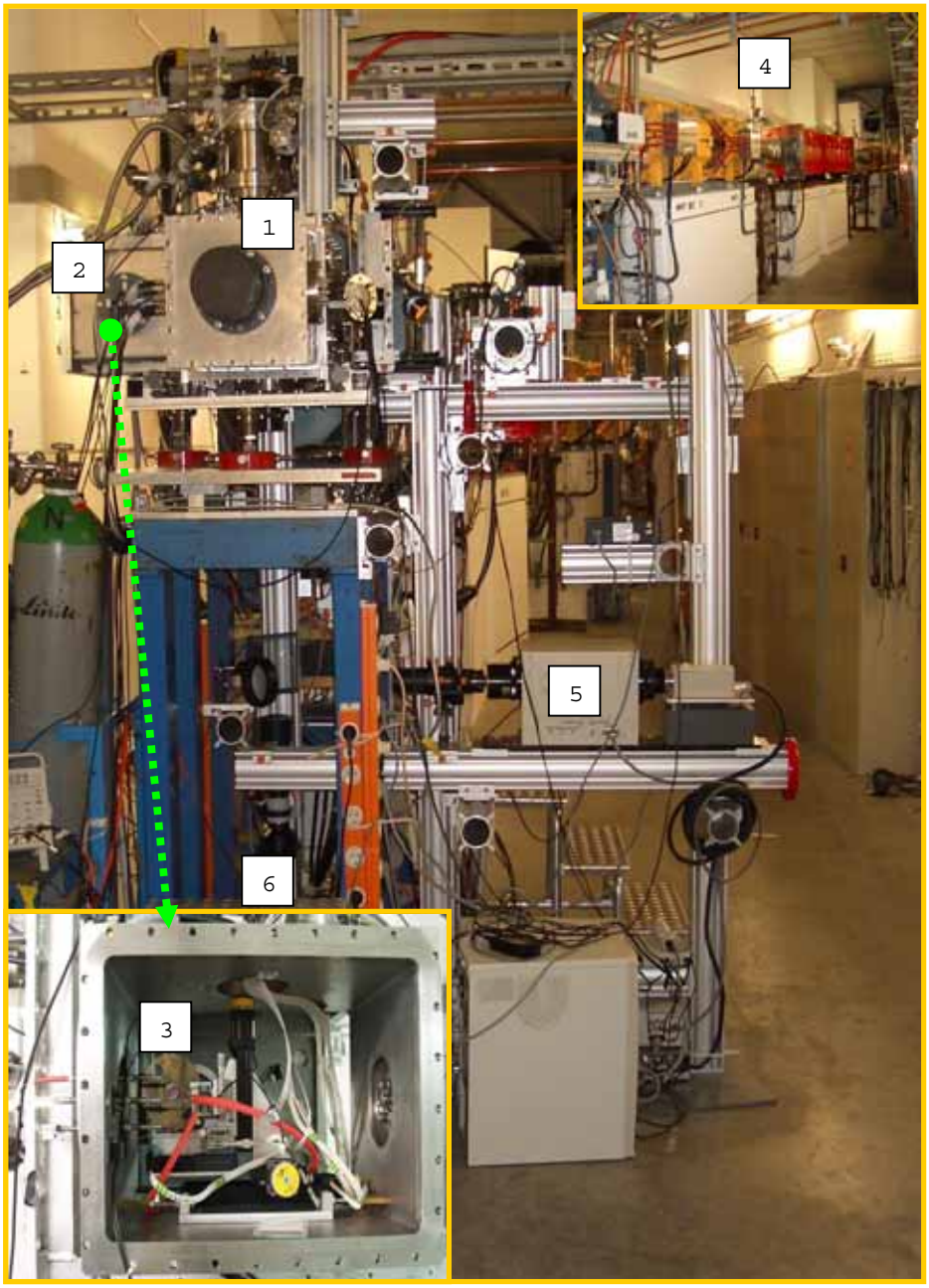

Figure 3.2: The HHT experimental area. 1 —target chamber, 2 —side-extender of the target chamber, 3 —pyrometer light collection optics in the side-extender of the chamber, 5 —HHT beam line, 6 —bottom CCD camera, 7 —backlighting streak camera.

glass and is equipped with electrical and optical fiber vacuum-feedthroughs. At the rear wall of the chamber there is a carbon beam dump where the ion beam is stopped after interaction with a target.

3.2 Target design for HEDP experiments with heavy ion beam

The scheme of the present target design is shown in Figure 3.3. The sample is a thin (0.05 mm – 0.2 mm) foil oriented along the ion beam axis. On either side of the foil, a sapphire block is placed that limits the expansion of the heated target material.

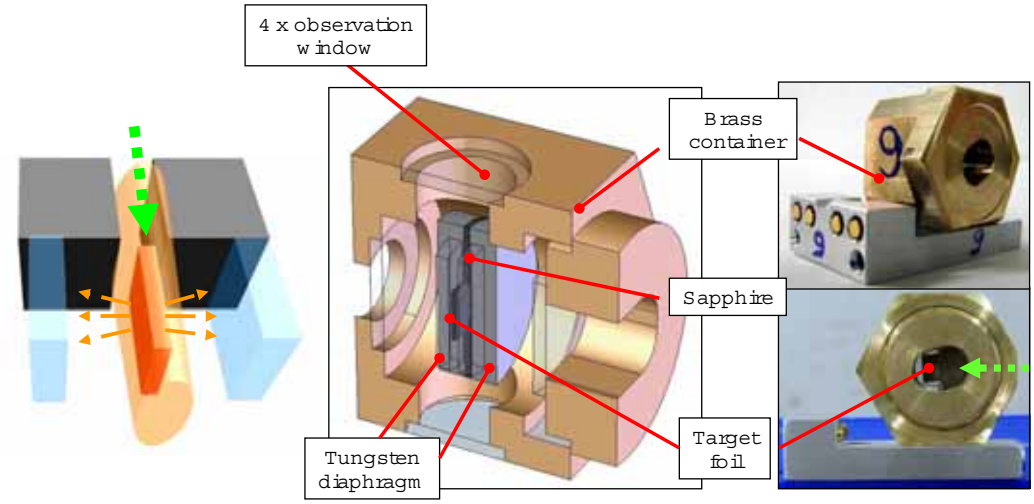

Figure 3.3: Concept, design and implementation of a target for the HIHEX experiments.

Figure 3.4: 4-axis manipulator for precise positioning of targets. Also shown shelves with targets.

The distance between the foil and the sapphires can be varied from zero to several millimeters, thus varying the final volume. To avoid direct irradiation of the sapphires

by an ion beam, a tungsten slit diaphragm is used. The entire physics package consisting of sample material, limiting sapphire blocks and the diaphragm, is mounted in a protective brass container. The primary goal of the container is to protect the valuable optics mounted inside the target chamber from target debris and to avoid their stacking in the components of the target positioning manipulator. While the physics package is destroyed in every shot, the brass container survives and can be used again. The container has four observation windows (left, right, up and bottom) made of 1 mm thick round sapphire (diameter 9 mm). A small modification can transform the container into a high pressure vessel, allowing to pump it with gas up to 100 bar.

Positioning of a sample to the ion beam is done by a custom-made 4-axis manipulator (see Figure 3.4) with accuracy of about 10 μm. A target assembly is mounted on a special table that can be taken by the target manipulator and brought to the focus of the ion beam. The table has four electrical contacts for the simultaneous electrical conductivity measurement. The manipulator and target shelves (27 targets per load) are placed inside the target chamber and can be controlled remotely, allowing exchange of targets without the need to re-evacuate and open the chamber.

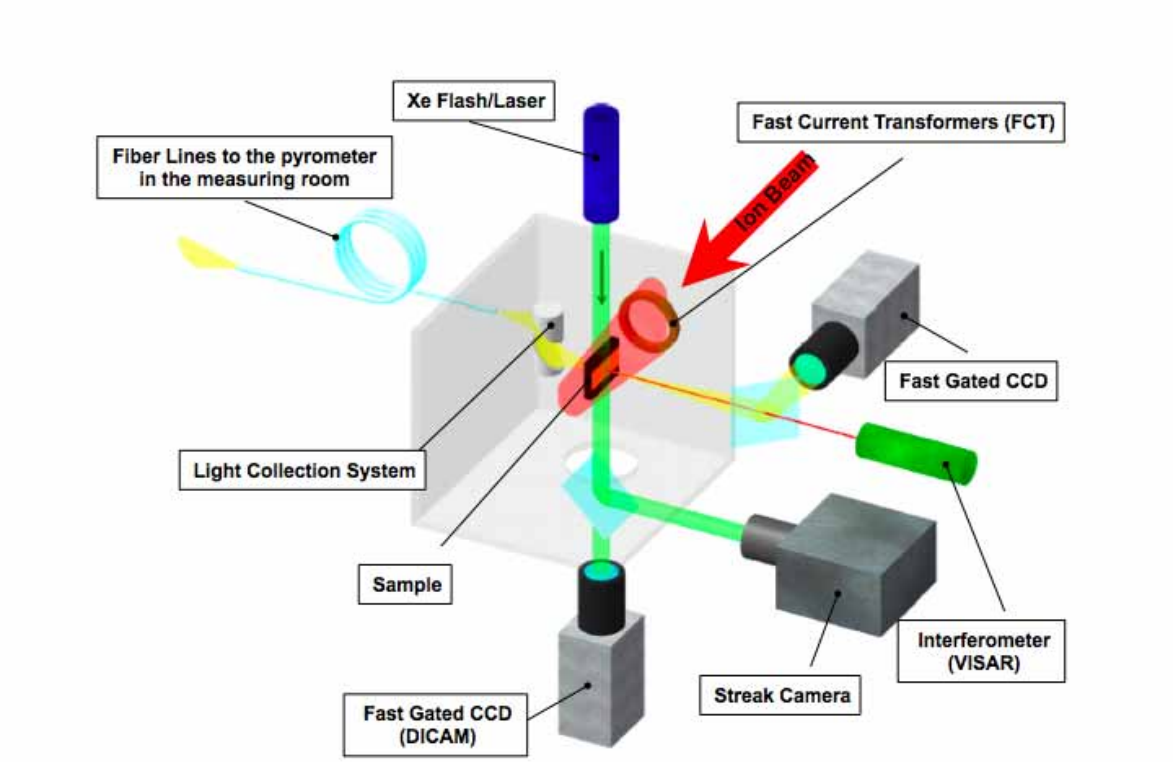

Figure 3.5: Setup of HED physics experiments at the HHT experimental area. Radiation from the sample is collected by a mirror objective and transmitted via glass fibers to the pyrometer in the measuring room.

3.3 Diagnostic instruments for HED physics experiments at HHT

The overall setup arrangement of the HEDP experiments at the HHT area is presented in Figure 3.5. In this scheme diagnostics that are aimed to measure temperature (detailed description in Chapter 4), pressure [40], electrical conductivity [41] of HED matter and also temporal/spatial profile of the heating ion beam [42] are shown.

Two fast gated, cooled, intensified CCD cameras (DICAM-PRO, PCO) look at the sample from the side and bottom. They measure the beam profile in the horizontal and vertical planes by recording ion-beam-induced scintillation of a buffer gas. The cameras are also used for precise beam-target positioning and for taking images of target self-emission during the experiment.

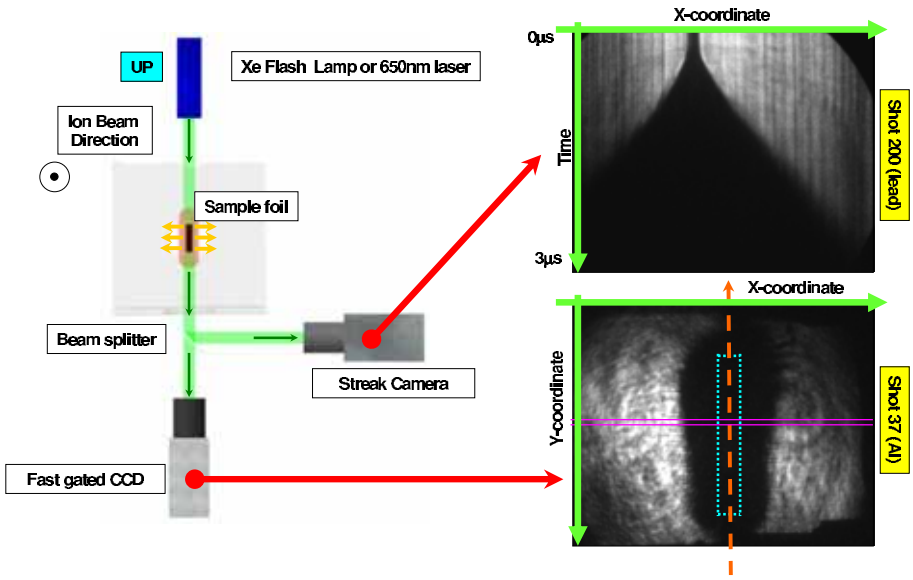

Figure 3.6: Backlighting scheme and images taken by a streak camera (top-right) and DICAM (down-right). The dashed blue line in the CCD record indicates initial dimension of the target foil.

In order to measure target expansion dynamics, the target is illuminated from the top by a xenon flash lamp or a powerful laser as shown schematically in Figure 3.6. The intensity of the blacklighter was adjusted to overcome self-emission of a target. The expansion velocity of a target can be directly obtained from the streak camera records (see Figure 3.6).

In addition to the pyrometer, a streak-camera-based-spectrometer (Figure 3.7) is used for the recording of a continuous spectrum with a high temporal resolution. The spectrum is resolved with a commercially available spectrograph CP140-202, Horiba Jobin Yvon. This spectrometer can record continuous spectra from 200 nm to 700 nm

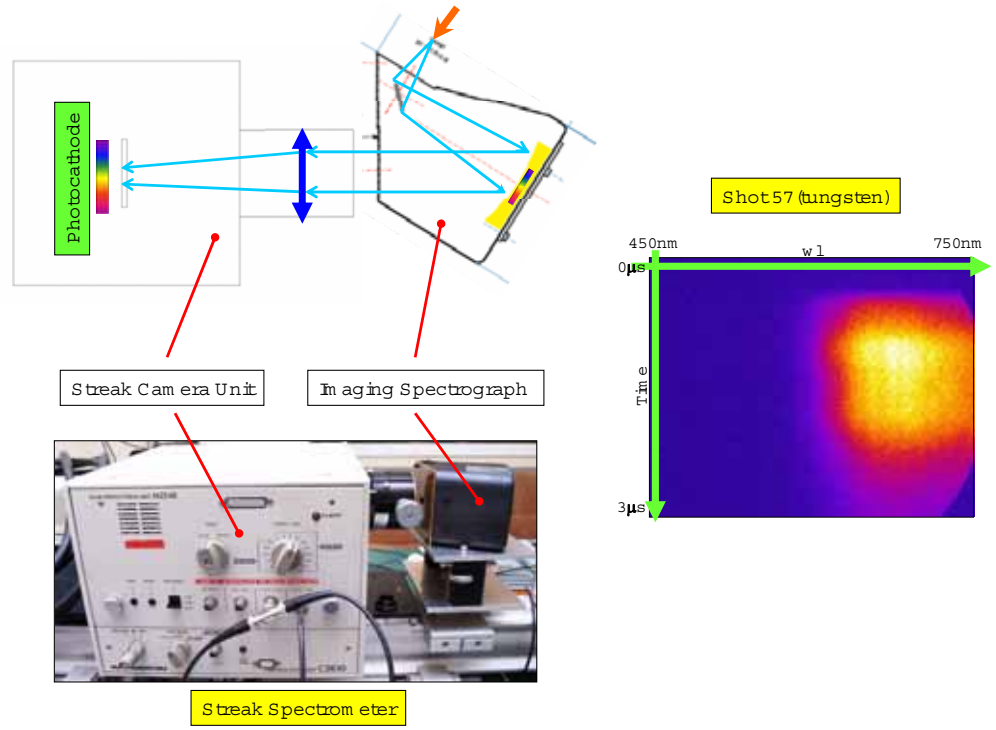

Figure 3.7: Design and implementation of the streak-camera-based spectrometer (left) with a typical experimental record (right).

with a high temporal resolution.

The intensity of the beam and its temporal profile are measured by a number of beam current transformers installed in the HHT beamline, including fast current transformers (FCT), an integrating current transformer (ICT) and a resonant current transformer (RCT). One of the FCTs is placed directly in front of the chamber.

4 Multi-wavelength pyrometer

Review of existing pyrometers. Multi-wavelength pyrometers are used for remote measurement of the temperature of an object whose emissivity is unknown. In general, the radiance of a given target area is required to be measured simultaneously in a number of wavelength bands with high precision. Multi-channel pyrometers can be classified by type of detectors, acquisition speed, dynamic range, the wavelength span of spectra. However, the most crucial point is the method how they resolve spectrum, since it has the main influence on the efficiency of the system.

Several researchers [22,44–46] have designed and constructed multi-wavelength pyrometers and employed least-square analysis of the results. Early instruments used arrangements which time-multiplexed the target radiance onto a single detector using rotating filters [47] or by scanning a spectrometer [48]. Such arrangements are not applicable where the target radiance varies on a time scale comparable with that required to measure each signal sequentially. To obtain simultaneous measurements in a number of wavelength bands, multiple detectors are generally used with filter systems, although dispersive instruments may be also employed. Prism instruments require temperature control for wavelength stability while grating instruments require order sorting and may introduce strong polarization differences between the detected beams.

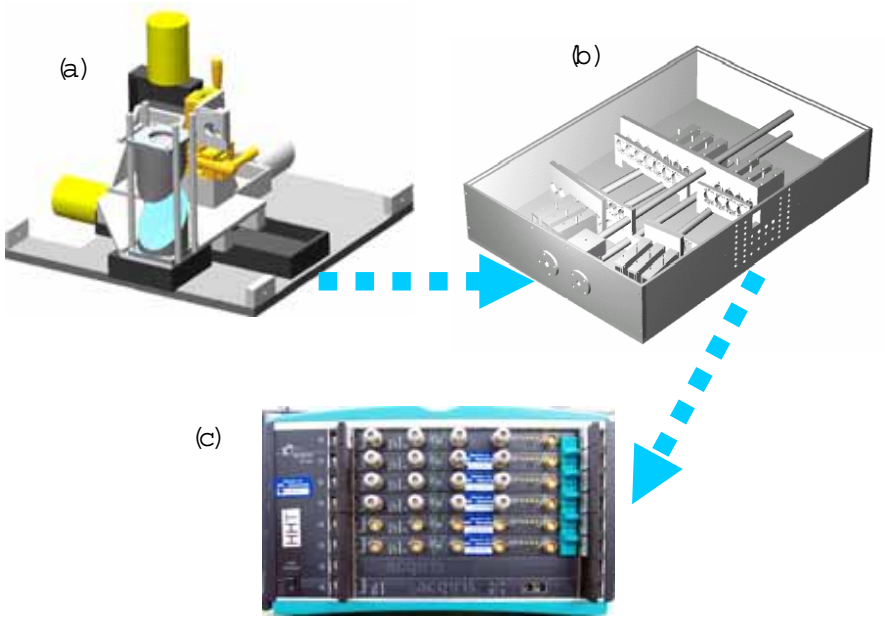

Figure 4.1: The development pyrometric system consist of three functional parts: Light collection system (a), fast spectral analyzer (b) and data acquisition hardware (c).

Optical systems employed together with filters include multiple collimating optics, where each detector receives a filtered image of the target via separate optical paths and fiber optics, used in a design similar to [49] where the target image was dissected by separating the fiber bundles into the required number of beams. More typical optical systems [50] use partially reflecting mirrors as beam splitters generally at a 45-degree angle of incidence, which again can introduce significant differences in the response of the channels where the radiation from the source is polarized. If the beam splitters are spectrally nonselective, the detection efficiency decreases as the number of channels is increased.

At present, the most efficient method is based on multiple reflection from an interference filter array. The first design and construction of such a pyrometer was proposed and implemented by [51]. In this reference a 6-channel pyrometer covering the 750 nm-1700 nm wavelength range was used for statical measurement of an object without prior knowledge of emissivity.

Pyrometer requirements for experiments with heavy ion beams at GSI. The temporal resolution of the pyrometer suitable for the present experiments with heavy ion beams is determined by the 120 ns beam duration. Since a temperature

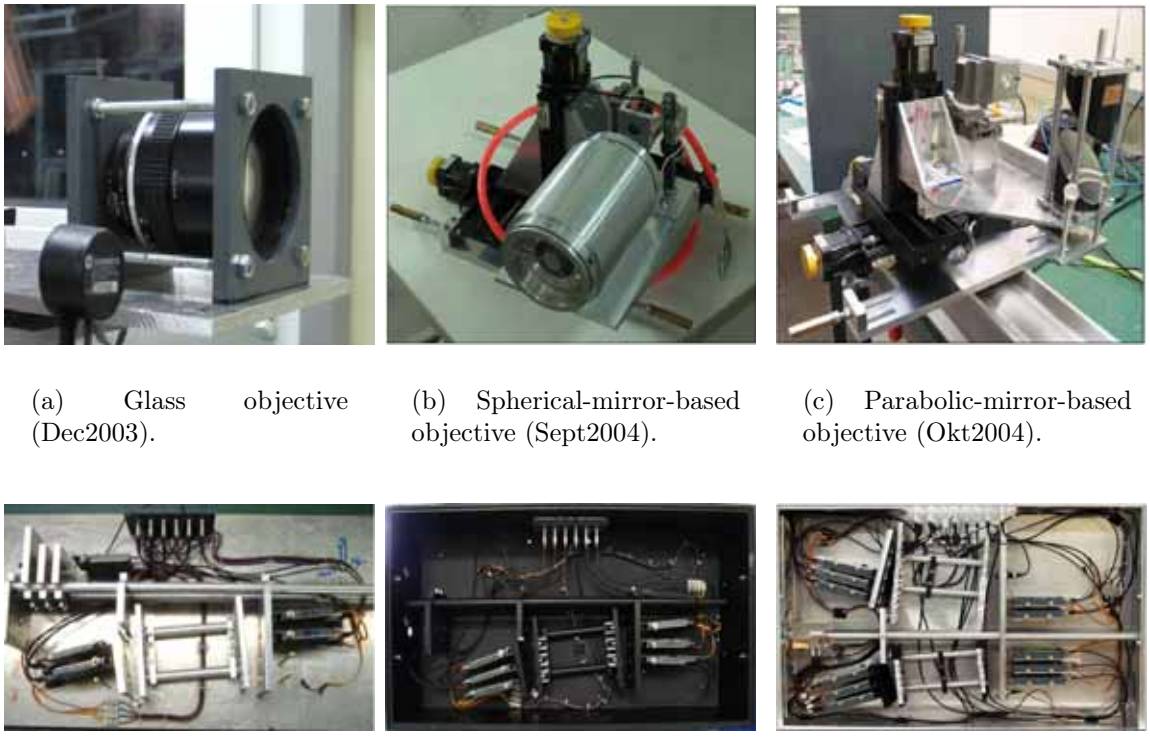

(a) Glass objective (Dec2003).

(b) Spherical-mirror-based objective (Sept2004).

(c) Parabolic-mirror-based objective (Okt2004).

(d) Prototype-I (Dec2003), 4 (6)+1 channels.

(e) Prototype-I (Sept2004) upgraded to 6 channels, anodized.

(f) Prototype-II (Okt2005), 6 (14)+6 channels.

Figure 4.2: Progress of the pyrometric system development.

record is required during the entire experiment, including heating with the beam,

cooling due to expansion, temperature increase due to impact against the sapphire and cooling down at the sapphire, the temporal resolution of the system must be on a nanosecond scale. In addition, the expected broad range of temperature changes requires a broad dynamic range of measurable temperatures from 1000 K to 15000 K.

A pyrometric system that fulfills above requirements has been implemented and it constitutes an important part of this thesis. The system has been developed from scratch and passed through designing, construction and commissioning phases. It is built of commercially available components as well as in-house produced parts. It is fully adapted for *in situ* applications and consists of three functional parts: light collection system, spectral analyzer and data acquisition hardware (see Figure 4.1).

During this work, two prototypes of spectral analyzers and three prototypes of light collection optics (see Figure 4.2) have been developed and tested. Every prototype is an improved version of the previous one and only the latest variant will be described below.

4.1 Design and construction

4.1.1 Light collection system

Effective collection of light plays a very important role in the pyrometric temperature measurement. Collection optics must be compact enough to fit the target chamber, must be very efficient, should be free from chromatic aberrations, have a high spatial resolution and must possess suitable geometry for efficient coupling of light to a glass fiber. To fulfill these requirements, a mirror based optical objective was designed and constructed. Every optical fiber has its numerical aperture that is a relative measure

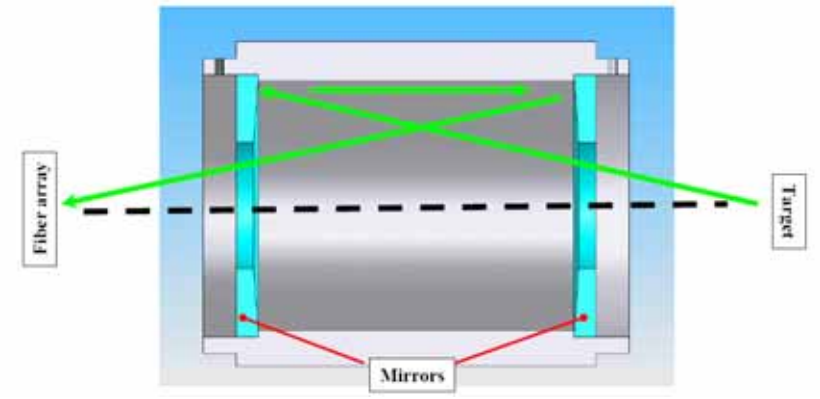

Figure 4.3: Working scheme of the sphere mirror objective.

of how much light a fiber can gather. All fibers used in experiments have a numerical aperture of 0.22 which equals an acceptance angle of 24.8°. This determines the solid angle of an objective and imposes an inevitable restriction of efficiency. Based on this limitation, two objective systems were developed with parameters listed in table 4.1.1 and working schemes explained in Figure 4.3 and Figure 4.4.

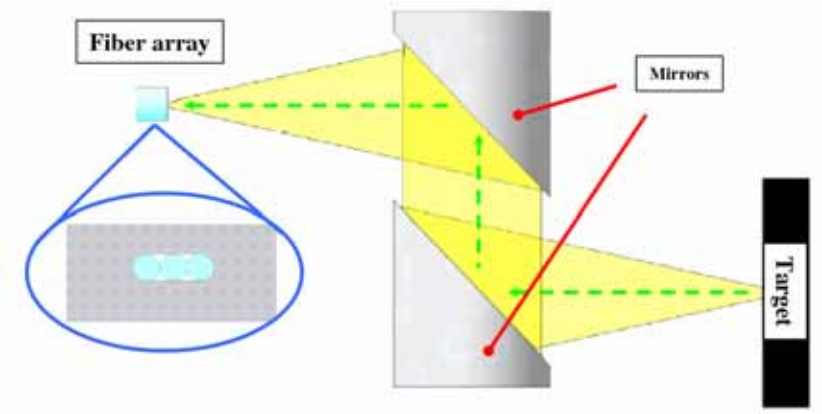

Figure 4.4: Working scheme of the parabolic mirror objective.

	Objective I:	Objective II:
Type of mirrors:	spherical	parabolic, 90-degrees, off-axis
Focus:	200 mm	101 mm
Diameter:	80 mm+central hole 40 mm	50 mm
Coating:	Protected silver	Protected silver
Numerical aperture:	f/5	f/2
Manufacturer:	Laser Components GmbH	Janos Tech Ltd.

Table 4.1: Parameters of the developed mirror objectives.

All dimensions and optical parameters of mirrors are chosen to fit the target chamber, fiber glass aperture and to provide the maximum performance at the same time. The spherical mirrors are a custom product and were manufactured after the in-house drawn sketches, whereas parabolic mirrors were available commercially. The protected silver coating of mirrors guarantees maximum reflectivity at wavelengths in the visible and near-infrared parts of the spectrum. The geometry of the mirrors is such that when a source is placed at the focus, beams in the image plane converge at 25 degrees.

Initially a spherical mirror-based objective was used. With time an idea of on objective based an parabolic mirrors appeared. The latter design has been used in recent experiments, since it is more compact and has a higher efficiency in comparison to the early version consisting of spherical mirrors.

The surface of a sample was 1:1 imaged to an array of three fibers (fused-silica, multimode) with 400μm of the core diameter oriented horizontally. These fibers (optimized for VIS/NIR light) then go via vacuum feedthroughs to spectrographs in the measuring room. As the mirror system is free from chromatic aberrations, the magnification value has no wavelength dependance and the same target area was probed at all wavelengths. This guarantees that light coupled to a fiber is collected from the area of interest only.

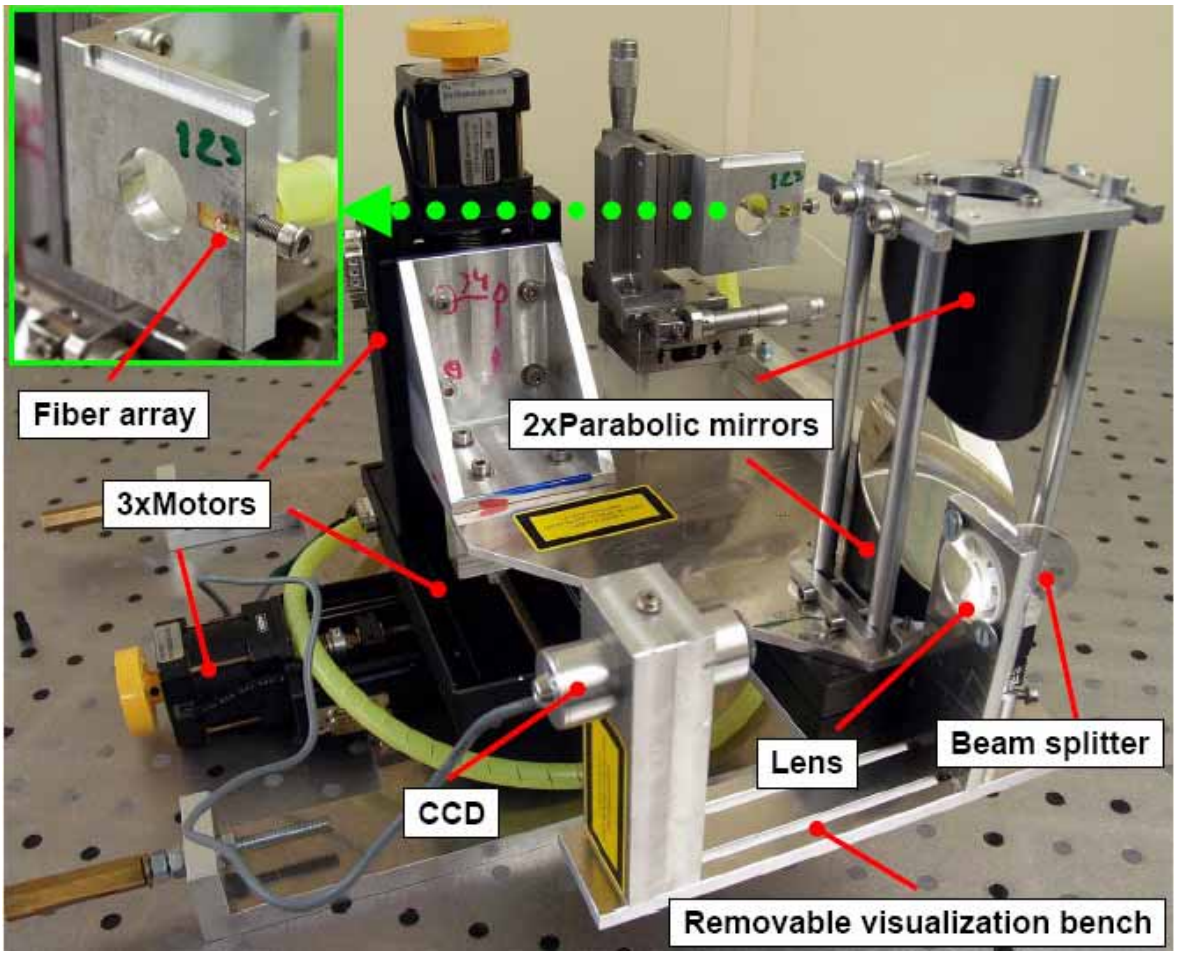

Figure 4.5: Parabolic-mirror-based light collection system mounted on the 3-axis motorized table. The visualization bench is used only for the calibration.

For remote adjustment and positioning, the optics is mounted on a motorized table (shown in Figure 4.5) that can be moved along three axes with 1 μm precision. The entire setup is placed inside the vacuum chamber and can be controlled remotely. The precise alignment of the light collection system to the calibration source (more details are in the "Calibration" section of this chapter) is achieved using a removable visualization bench, which is removed in during an experiment.

4.1.2 Spectral analyzer

The principle scheme of the spectral analyzer is shown in Figure 4.6. It consists of two independent sub-spectrographs (legs) with an identical spatial arrangement of optical elements mounted in one casing. Every leg has its own fiber input of the SMA type that discriminates spectrum at six wavelengths (channels). A pair of achromatic lenses collimates the light to a quasi-parallel beam, which then experiences successive reflections from six interference filters. The mechanism of spectral resolution is based on the property of an interference filter being transparent for a narrow part of spectrum and

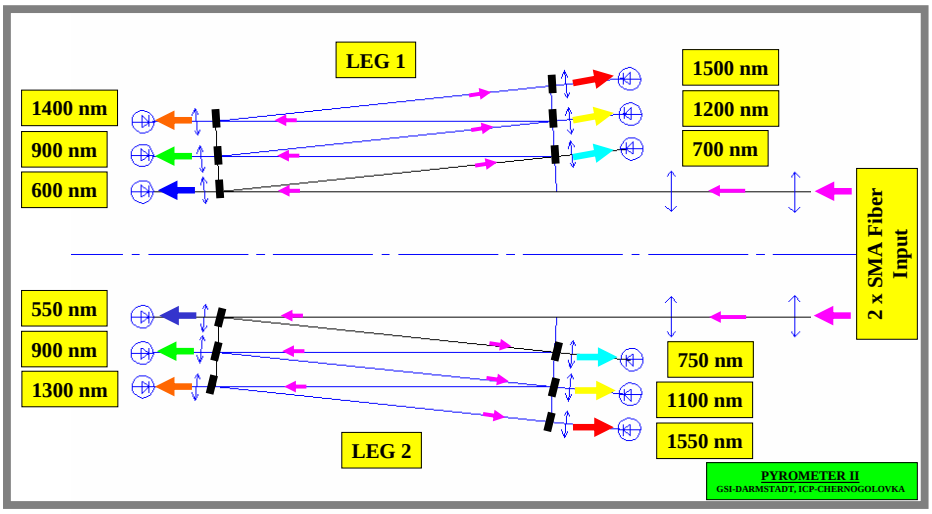

Figure 4.6: The principle working scheme of the spectral analyzer.

acting as a mirror for the rest [26, 51].

It is to note that the pyrometer has been developed for temperature measurement of bodies whose emissivity is not known. In the work [29] was shown that, as long as there is no information about emissivity available, an increasing number of wavelengths does not increase the accuracy of temperature measurements. That is the reason why traditionally, the number of channels used in a pyrometer does not exceed six.

The choice of wavelengths is determined by the spectral position of the maximum of the Planck curve. As the main radiation dynamics happens within this range, the system must operate in the wavelength range that contains or is close to this peak. For the temperature range of interest from 1000 K to 15000 K, the peak lies between 200 nm - 2000 nm. The spacing between wavelengths of channels and their width was selected experimentally. The guideline of this selection were optimum efficiency of all channels simultaneously and a uniform coverage of the visible and near infrared part of spectrum. Following these considerations, two filter sets listed in table 4.2 and 4.3 were installed.

Channel number	CH1	CH2	CH3	CH4	CH5	CH6
Wavelength, nm	600	700	900	1200	1400	1500
FWHM, nm	10	10	10	10	10	20
Diode type	Si	Si	Si	InGaAs	InGaAs	InGaAs

Table 4.2: List of pyrometer channels in Leg-1.

Channel number	CH7	CH8	CH9	CH10	CH11	CH12
Wavelength, nm	550	750	900	1100	1300	1550
FWHM, nm	40	40	40	25	25	25
Diode type	Si	Si	Si	InGaAs	InGaAs	InGaAs

Table 4.3: List of pyrometer channels in Leg-2.

The filter array covers a spectral span from 500 nm to 1500 nm with an average step of ∼100 nm. All filters are a commercial product purchased from the Andover Corporation. The order of filters in the array was chosen to provide optimal signal levels at all channels simultaneously. The order is determined by absolute sensitivity of each detector (see Figure A.1 in Appendix) and relative spectral intensity of the calibration source (see Figure 4.9). The maximum number of channels is in principle limited by an average loss of 20 % at every reflection. In addition, seven free slots in leg-1 are available and the number of channels in this leg can be extended to 13. This extension may be valuable when more complicated emissivity models will be applied in the future.

Filtered light is focused by an 18 mm aspherical lens to the crystal of a solid state photodiode. Parameters of collimation and focusing optics inside the spectrometer are such that the focused spot at the crystal of the diode is smaller than the size (~ 1 mm^2) of the crystal itself.

For high sensitivity over the broad range of the spectrum, two kinds of low-level-dark-current photodiodes with 5 ns rise-time are used. For channels from 500 nm to 900 nm, Si-diodes (Hamamatsu S7836-01) and for channels from 1000 nm to 1550 nm, InGaAs-diodes (Hamamatsu G8376-05) were installed. All diodes are run in a linear regime and are coupled to a custom, broad-band, low-noise current amplifier with two 50 Ω-outputs. The first output has a maximum possible amplification degree that does not reduce the inherent bandwidth of the diode. Its highest voltage output is 1.9 V, while the noise level is ± 20 mV. The amplification of the second output is adjustable and in last experiments, the ratio of amplification between the second and the first output was 10. This makes the second output more suitable for lower temperature measurement. However, in case of fast changing signals this output is not suitable, since higher amplification means higher temporal integration.

The first channel of leg 2 (550 nm) was installed on purpose without any amplifiers. As a consequence it has an increased dynamical range up to 5 V (noise level 1 mV) in comparison to 1.9 V. It is therefore of great value in experiments where the range of temperatures is extremely broad. The 5 V value is the limit imposed by the maximum voltage that a conventional oscilloscope can accept at the 50-Ω load.

A mechanical chopper for light modulation is installed right after the fiber input (see Figure 4.7b). This component is necessary for the calibration of the system with a DC tungsten ribbon lamp and is removed during actual temperature measurement.

Red laser diodes (λ=637 nm) are installed in every leg of the spectral analyzer. A laser is mounted in the next free slot of a filter array and its position is adjusted so that its optical path is the same as that of the light to be analyzed (lasers emits in the

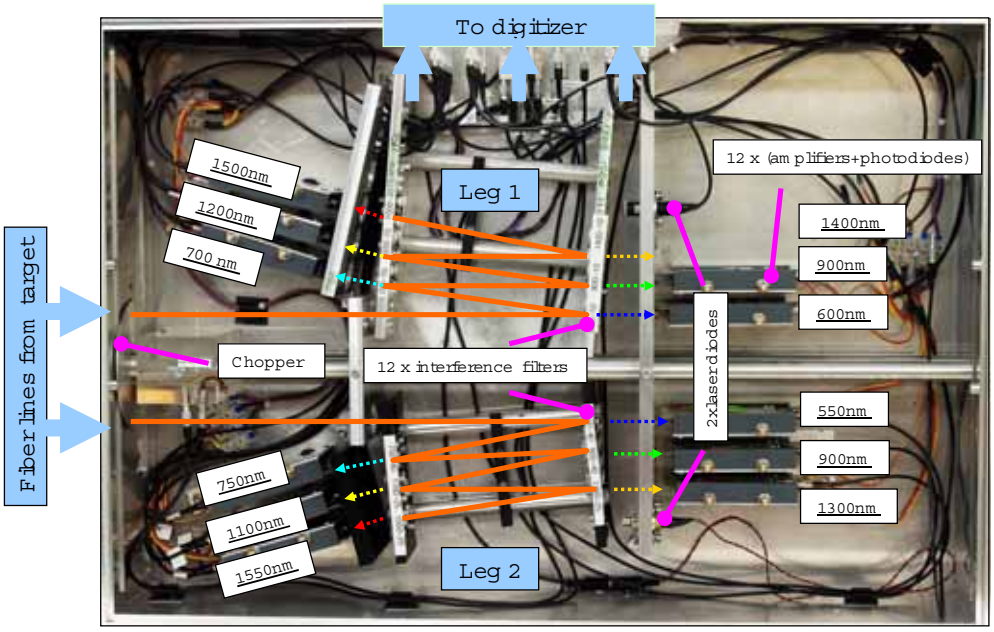

(a) Top view.

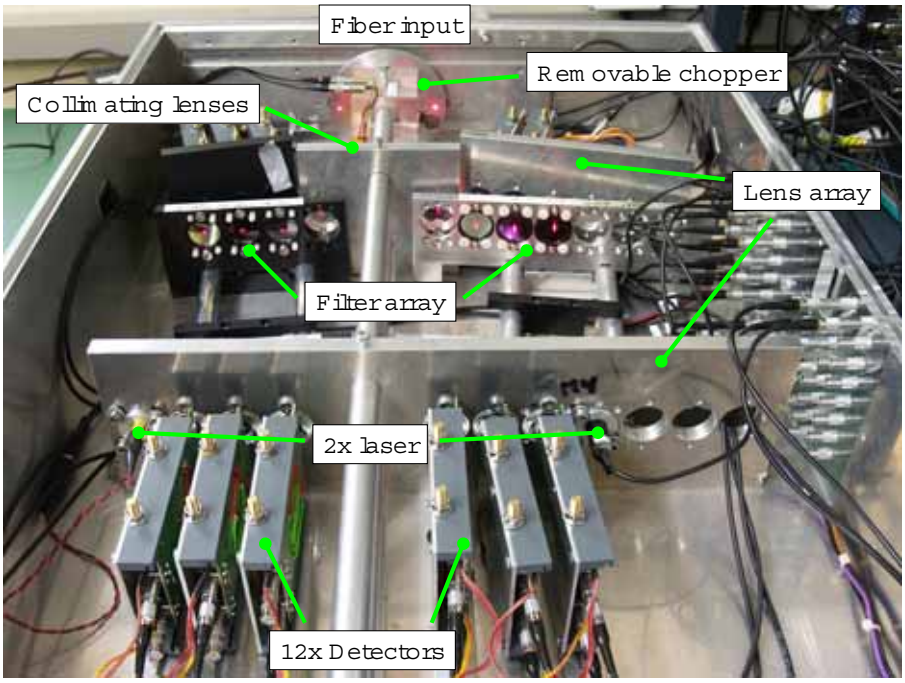

(b) Front view.

Figure 4.7: The 12-channel spectral analyzer.

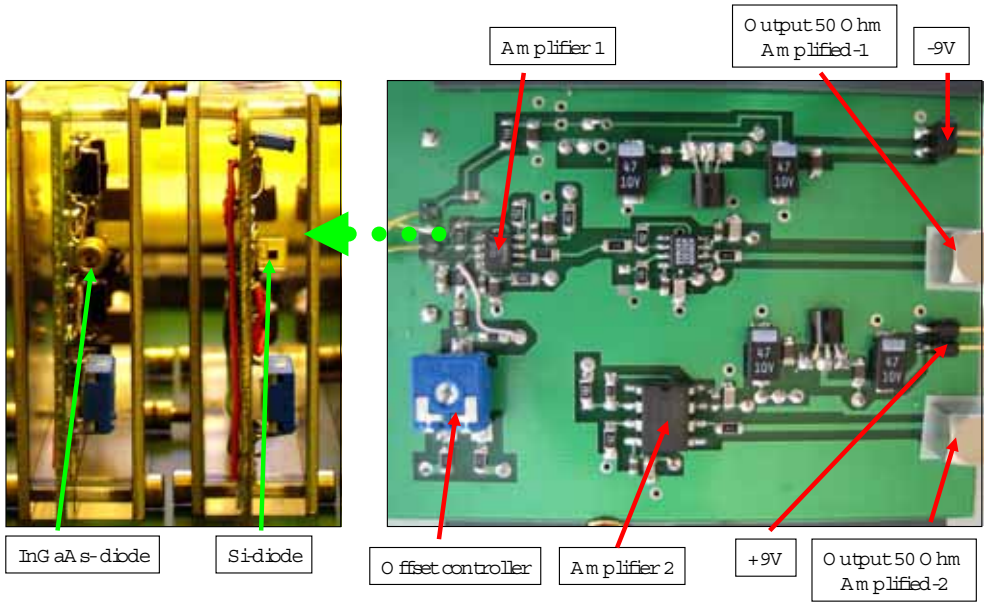

Figure 4.8: Si and InGaAs photodiodes used for the light detection in visible and near parts of the spectrum respectively (right). These photodiodes are coupled to the broad-band, low-noise current amplifier (left).

reverse direction). Effectively, the image of a diode is transmitted to the fiber entrance after multiple reflections at all filters of the array (see Figure 4.7 b). One of the main purposes of these lasers is a quick control of the alignment of the filters in the array: the intensity of laser at the fiber input is measured with powermeter and compared with the value obtained for an optimal alignment of all filters.

In comparison to existing pyrometric systems mentioned in the beginning of this chapter, the present one has several advantages. Usually, the entire optics is assembled next to the target chamber with a direct coupling of the light to the system. Such an arrangement is not moveable, very sensitive to misalignments and tied to a certain geometry of a radiating sample. The described pyrometer is mounted in a separate transportable box with a fiber input. It can be treated as a fast absolutely calibrated spectrometer, making it applicable to any kind of source with a random geometry. The fixation of optics is very reliable and in generally only a single-time adjustment of optical components is required. Depending on expected temperatures, an appropriate set of filters can be re-mounted and if processes faster than 5 ns are expected, diodes and amplifier with corresponding speed characteristics can be re-installed. In addition, two independent legs make possible to probe two different spots on a sample simultaneously. If a radiating object has a homogeneous surface temperature distribution, both legs of the pyrometer measure the same temperature and the system transforms to a single 12-channel pyrometer.

4.1.3 Data acquisition hardware

In total there are 24 detector outputs that are recorded by a 24-channel, 8-bit digitizer (Acqiris DC271, 1 GHz, 1-4 GS/s) which is fully controlled from a PC. All 24 inputs of the digitizer are synchronized to one picosecond. The controlling and storing of data is realized by a specially written software implemented in LabView. The program has a graphical interface that permits setting of basic parameters of an ordinary oscilloscope. The digitizer has also an option to make averaging of many waveforms, which is required for the calibration procedure. During experiments, signals from the spectral analyzer are recorded after the arrival of a trigger signal and then stored on a PC. Data from each channel is stored in a separate ASCII file consisting of two columns, time in nanoseconds and voltage in volts. One of the advantages of the digitizer is that the record length is unlimited. The smallest time step is 100 picoseconds. The typical time step used in the experiments has been one nanosecond.

4.2 Data processing and analysis

4.2.1 Calibration

The general method of pyrometer calibration is discussed in details in [36, 37] and is based on application of the entire system, including light collection system, fibers, to a radiating object with a geometry similar to a real target and known absolute spectrum. While providing conditions similar to the ones in the experiment, voltage response at each detector is recorded.

The pyrometer is calibrated by a tungsten ribbon lamp of the "Pharaoh type", Osram W17/G (figure 4.9a). The lamp is powered by a special current-stabilized-power supply, which maintains fairly constant and stable radiation in time. The precise absolute spectrum of the lamp, R_{osram}, is provided by the manufacturer and plotted in the Figure 4.9b (includes transmission of the observation window). The spectrum is measured at brightness temperature, T_{650}=2400 K at 650 nm that corresponds to physical temperature of 2600 K.

The tungsten ribbon can be treated as a Lambertian source, meaning that the demonstrated spectrum is the same at every angle of observation.

Brightness temperature of the lamp at 650 nm can be measured independently with comparison pyrometer Keller Micro PV11. Powering voltage that corresponds to $T_{650} = 2400K$ is determined with the help of this pyrometer and every calibration procedure is carried out at this value (see Figure 4.10).

Date of measurement:	16.03.04	20.09.04	22.09.05
Calibration voltage, mV:	34.80	34.83	34.92

Table 4.4: Calibration voltages of the tungsten lamp.

With time the tungsten ribbon changes its properties and there fore this measurement should be carried out regularly in order to obtain the correct calibration voltage

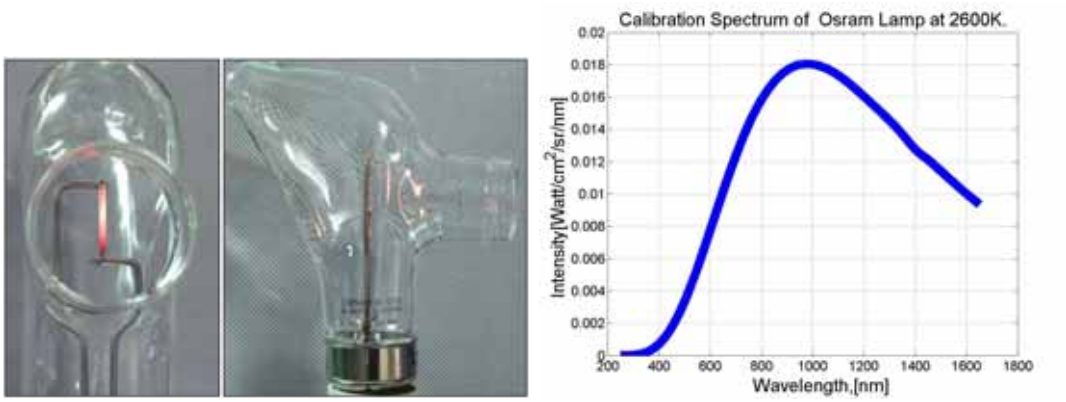

(a) Tungsten ribbon lamp.

(b) Spectrum of Osram W17/G tungsten ribbon lamp at $T_{650} = 2400K$.

Figure 4.9: Osram W17/G tungsten ribbon calibration lamp.

and to track the degradation of the lamp (see Table 4.4).

In real experiments, the system has been used in a single-shot (impulse) mode, whereas during the calibration, the lamp is working in the continuous mode. In order to approach experimental conditions as close as possible and to avoid any effects occurring in photodiodes under continuous intense irradiation (charge accumulation, saturation), the continuous radiation of the lamp was modulated by a mechanical chopper. The chopper allows to irradiate periodically all detectors for several milliseconds and generates a trigger when the irradiation starts. For reducing errors of calibration caused by time instabilities of the lamp and noise of the detectors, the calibration voltage is deduced from the averaging of thousand "identical" curves (see Figure 4.11). The difference between zero level and the "plateau" defines calibration voltages V_0^i for a given channel i.

Channel, nm:	600	700	900	1200	1400	1500
Voltage, V, ±1.5%:	0.010	0.021	0.037	0.041	0.035	0.0188
Channel, nm:	550	750	900	1100	1300	1500
Voltage, V, ±1.5%:	0.004	0.290	0.190	0.143	0.284	0.201

Table 4.5: Example of typical calibration values of voltages (unamplified).

During experimental shots the optics views the target through the sapphire observation window which has its own optical transmission properties. To take this into account, sapphire, identical to sapphires used for these windows, was placed in front of a fiber array during every calibration procedure. Thus, it is not necessary to consider optical properties of sapphire during data processing, since they are already included in the calibration coefficients.

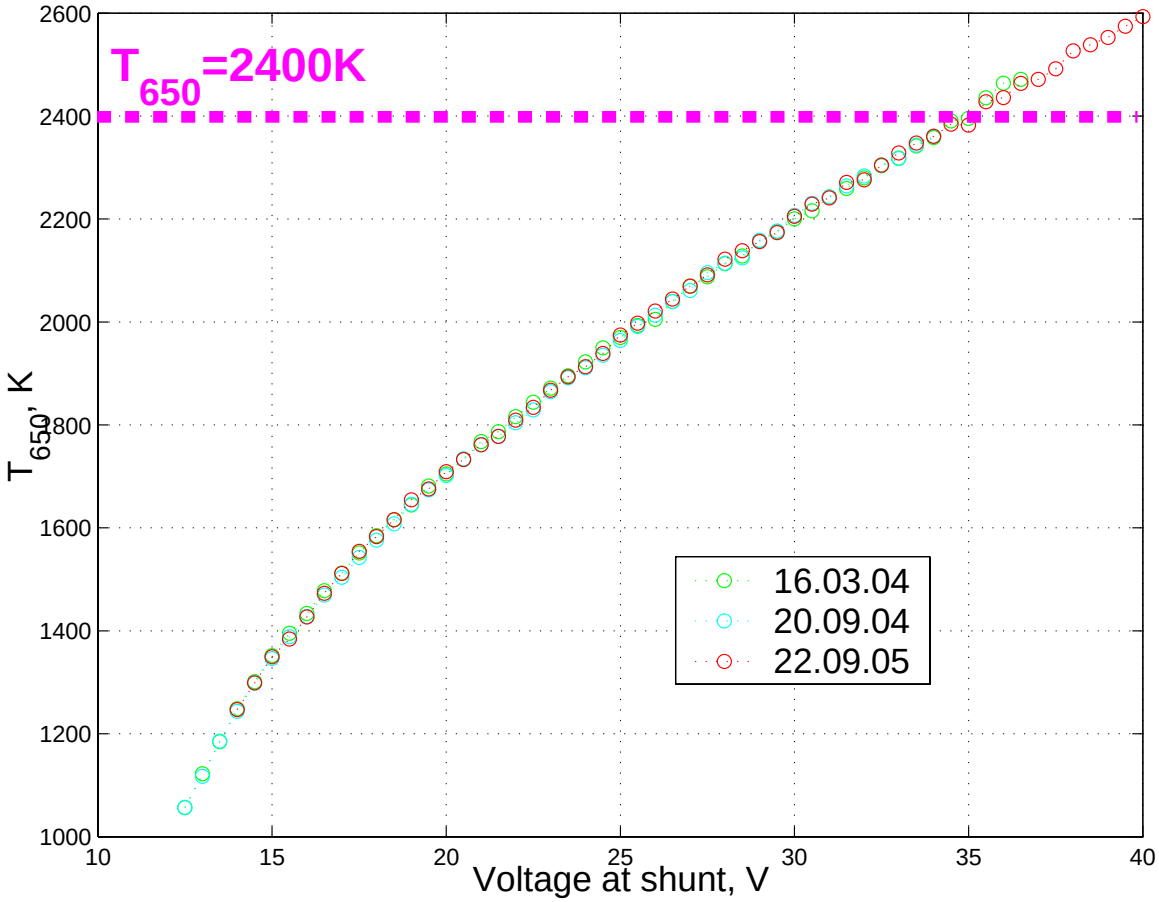

Figure 4.10: The 650 nm brightness temperature of tungsten lamp as a function of power supply voltage.

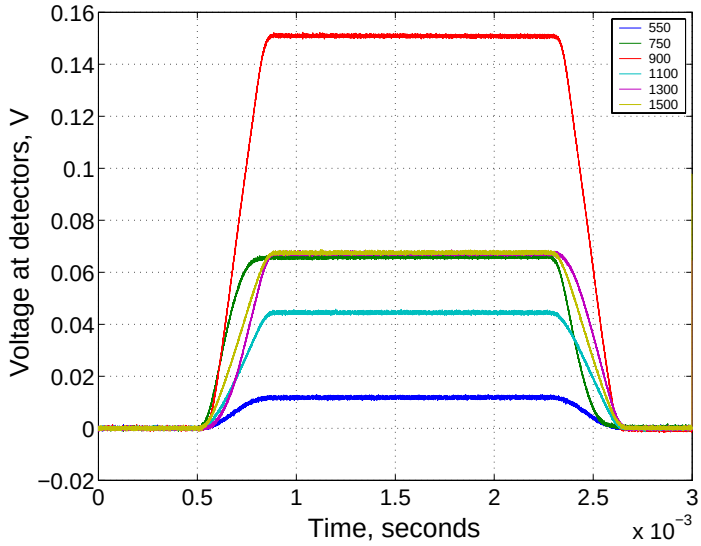

Figure 4.11: Example of typical calibration curves of the pyrometer.

The quantity of light I^i introduced to the system at channel i is equal to

$$I^i = \int_0^{=\Omega_0} \int_0^{\infty} L(\lambda) \cdot F_i(\lambda) \cdot R(\lambda, T, \Omega) \cdot d\lambda d\Omega,$$

$$i = 1, 2, 3, ..12.$$

Here $L(\lambda)$ - the overall transmission of optics, vacuum feedthrough and fiber, $F_i(\lambda)$ - the transmission of an interference filter, $R(\lambda, T, \Omega)$- radiation density of an object(energy irradiated during one second from unit square into one steradian at wavelength λ), Ω_0-is a spatial angle that corresponds to the 24°-aperture of the collection optics. $F_i(\lambda)$ can be well approximated with a Gauss curve centered at the maximum of the filter transmission band and with width equal to the FWHM of the filter. From the consideration that the radiating object is a Lambertian source follows that $R(\lambda, T, \Omega) = R(\lambda, T)$ and

$$I^i = \Omega_0 \int_0^{\infty} L(\lambda) \cdot F_i(\lambda) \cdot R(\lambda, T) \cdot d\lambda,$$

The voltage output of the detector is then

$$V^i = \Omega_0 \int_0^{\infty} S_i(\lambda) \cdot L(\lambda) \cdot F_i(\lambda) \cdot R(\lambda, T) \cdot d\lambda,$$

where $S_i(\lambda)$ - sensitivity of the detector, which depends on a wavelength only as the diode is used in a linear regime.

Since the transmission band width of filters is very narrow (40 nm) and no significant changes of $L(\lambda), S(\lambda)$ and $R(\lambda, T)$ occur on a 40 nm scale, the following approximation can be used

$$V^i = \Omega_0 \int_0^{\infty} S_i(\lambda) \cdot L(\lambda) \cdot F_i(\lambda) \cdot R(\lambda, T) \cdot d\lambda \approx$$

$$\approx \Omega_0 \int_0^{\infty} S_i(\lambda_i) \cdot L(\lambda_i) \cdot F_i(\lambda) \cdot R(\lambda_i, T) d\lambda =$$

$$= \Omega_0 \cdot S_i(\lambda_i) \cdot L(\lambda_i) \cdot R(\lambda_i, T) \cdot \int_0^{\infty} F_i(\lambda) d\lambda =$$

$$= 1/K^i \cdot R(\lambda_i, T),$$

where λ_i is the wavelength that corresponds to the maximum of transmission of $F_i(\lambda)$ and

$$1/K^i = \Omega_0 \cdot S_i(\lambda_i) \cdot L(\lambda_i) \cdot \int_0^{\infty} F_i(\lambda) d\lambda$$

is the coefficient that relates voltage output to radiation. It represents the sensitivity of a channel and does not depend on a radiation source. The values of the coefficients are obtained from

$$K^i \equiv \frac{R_{\text{osram}}(\lambda_i)}{V_0^i}.$$

4.2.2 Data processing

The temperature determination from the raw experimental output of the pyrometer is explained in this section. Results presented here were obtained utilizing the MATLAB environment and all experiments carried out in this work were processed in the same way.

The processing of real experimental data (Shot 57, Oktober 2005, Leg1) is given below as an example. In this experiment a tungsten foil was heated by an ion beam and was allowed to expand freely in vacuum without any constraining sapphire walls. Recorded voltages, V^i (Figure 4.12a) are converted to intensities, R^i (Figure 4.12b) by using the calibration coefficients K^i:

$$R^i(t) = K^i \cdot V^i(t).$$

After the conversion to intensities, every curve was eventually smoothed with third power polynomials. In order to avoid artefacts the smoothing window was selected individually for every record, taking into account the slope of each curve.

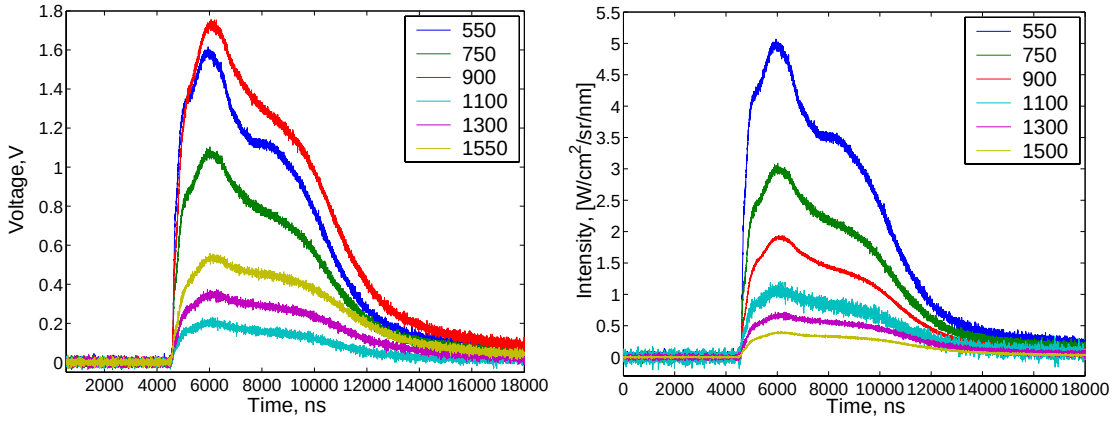

(a) Raw experimental data in volts.

(b) Intensities in absolute units.

Figure 4.12: Recalculation of raw data (left) to absolute intensities (right). The records show six channels of the pyrometer. Curves are not smoothed.

The primary experimental output of the pyrometer are brightness temperatures T_i^{br} at six wavelengths resulting as a solution of the equation

$$R^i(t) = R_{\mathrm{Planck}}(\lambda_i, T_i^{\mathrm{br}}(t)).$$

As it was already mentioned in the beginning of Chapter 2, in case of non-black-body radiation, brightness temperature is channel dependent and is different from the physical temperature of the body. It was also noted that in order to approach the true temperature, some analytical model of emissivity must be used. In this case, recorded intensities must be fitted to a function consisting of the Planck formula multiplied by

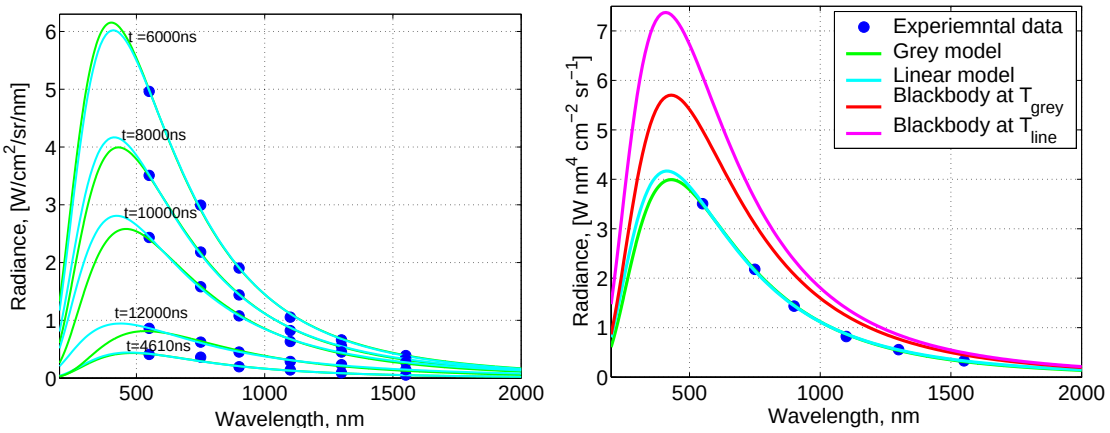

(a) Fitting of experimental points to radiation models at different moments of time.

(b) Fitting of experimental points to radiation models at $t = 8000$ ns. Also plotted black-body spectrum corresponding to fitted temperatures.

Figure 4.13: Fitting of experimental data at different moments of time. Blue circles are experimental data, green curves are fitted grey body radiation, blue curves are fitted linear model of radiation. Errors of measured radiances are of the same order as the diameter of the circles.

a model emissivity. The fitting algorithm and its peculiarities when applied to a six-channel pyrometer have been studied in detail by many researchers, see for example [52].

The simplest model assumes that emissivity is independent of the wavelength, the so-called grey body radiation. In this case, the "grey" temperature is determined by fitting six experimental values to a system of six equations, where ϵ and T_{grey} are free parameters:

$$\epsilon(\lambda) = \epsilon,$$

$$\{R^i(t)\} \longrightarrow \{\epsilon(t) \cdot R_{\text{Planck}}(\lambda_i, T_{\text{grey}})\}, i = 1, 2, ..6.$$

A simplified version of the grey body approach is the so-called "ratio pyrometry" method. In this method intensities at only two close wavelengths (traditionally, the maximum distance between neighboring channels does not exceed 100 nm) $R(\lambda_1, T)$ and $R(\lambda_2, T)$ are recorded, and a grey emissivity behavior within this short wavelength interval is assumed [43]:

$$\epsilon(\lambda_1) = \epsilon(\lambda_2).$$

This assumption leads to the following formula, where T is the only unknown variable:

$$\frac{R(\lambda_1, T)}{R(\lambda_2, T)} = \frac{\epsilon(\lambda_1) \cdot R_{\text{Planck}}(\lambda_1, T)}{\epsilon(\lambda_2) \cdot R_{\text{Planck}}(\lambda_2, T)} = \frac{R_{\text{Planck}}(\lambda_1, T)}{R_{\text{Planck}}(\lambda_2, T)}.$$

A nice feature of a multi-wavelength pyrometer is that it automatically incorporates several ratio-pyrometers.

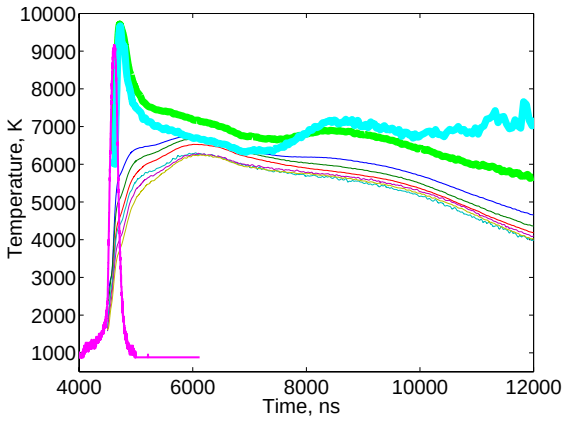

(a) Brightness,"grey" and "linear" temperatures.

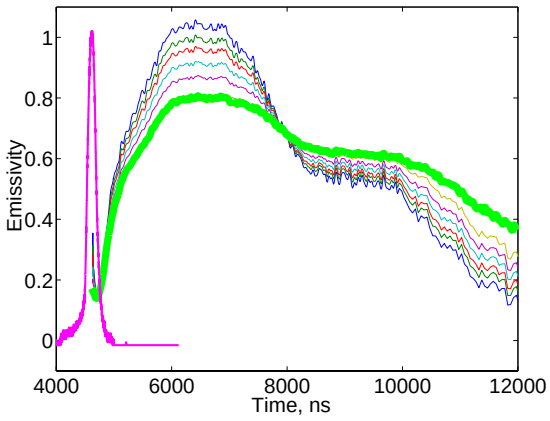

(b) Emissivity.

Figure 4.14: Temperature and emissivity produced by the fit. Dark blue is brightness temperature at 550 nm, dark green at 750 nm, red at 900 nm, blue at 1100 nm, magenta at 1300 nm, brown at 1500 nm. The green curve is the grey temperature, cyan is the linear temperature. The thick magenta curve is the record of the synchronized fast current transformer that represents the temporal intensity of a beam in arbitrary units.

An extension of the grey emissivity model is the assumption of a linear dependance of emissivity on wavelength. In this case there are three free parameters A_1, A_2 and T_{line}:

$$\epsilon(\lambda) = A_1 \cdot \lambda + A_2.$$

$$\{R^i(t)\} \longrightarrow \{(A_1(t) \cdot \lambda_i + A_2(t)) \cdot R_{Planck}(\lambda_i, T_{line})\}, i = 1, 2, ..6$$

From a mathematical point of view, fitting is minimization of a function

$$\sum [R^i(t) - \epsilon \cdot R_{Planck}(\lambda_i, T)]^2.$$

However, a more correct way is to fit a weighted function as it was demonstrated in [52]. If the uncertainties, ΔR^i, of radiances are given, minimization of the following function will produce a more reliable result

$$\sum [\frac{1}{\Delta R^i}(R^i(t) - \epsilon \cdot R_{Planck}(\lambda_i, T))]^2.$$

Figure 4.13a shows how experimental points fit to the analytical models of radiation. Fitting has been carried out for different times with respect to the ion beam pulse.

The final output of the entire data processing procedure is summarized in Figure 4.14. Brightness, "grey", "linear" and "ratio" temperatures are plotted in Figure 4.14a and "linear" emissivity at six working wavelengths along with "grey" emissivity obtained from the fits is shown in Figure 4.14b.

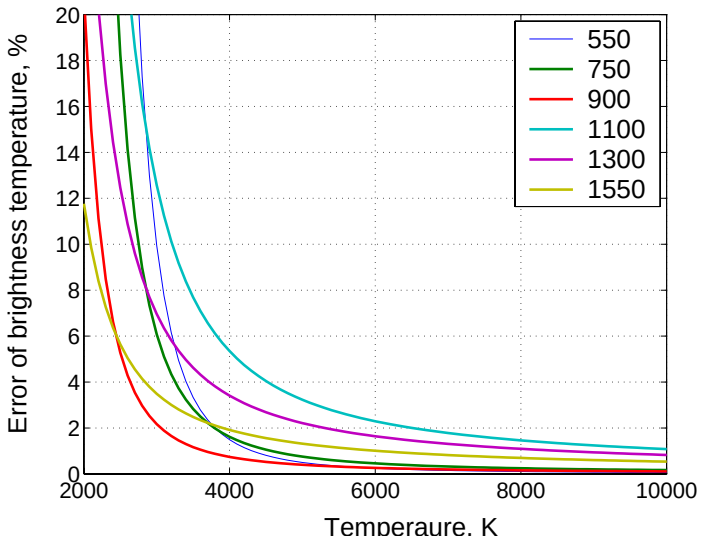

Figure 4.15: Accuracy of brightness temperatures versus temperature (level of signal).

4.3 Accuracy of measurements and data processing

Accuracy of brightness temperatures. The accuracy ΔT^i_{br} of the brightness temperatures, T^i_{br} is determined by the accuracy, ΔR^i of measured intensities, R^i. ΔR^i is given by accuracy of calibration coefficients, ΔK^i and measured voltage, ΔV^i:

$$\Delta R^i = \Delta V^i + \Delta K^i.$$

Error of voltage, ΔV^i is determined by the statistical dispersion of noise, σV^i and 8-bit resolution of the acquisition hardware. For the data processing described in the pervious section, dispersion is calculated from the first 4000 ns of the records in Figure 4.12a and equals ≈50 mV. The roughest digitization resolution is 5 mV. Accuracy of calibration coefficients is determined by multiple re-alignment of the optics to the calibration tungsten lamp, i.e. the same calibration procedure was performed several times. It has been found that calibration coefficients K^i can be reproduced with accuracy $\Delta K^i/K^i = 3\%$. Thus accuracy of brightness temperature measurement is

$$\Delta T^i_{br} = \left[\frac{\partial R_{Planck}}{\partial T}\right]^{-1} \cdot \Delta R^i$$

The result of the estimation with relevant in experimental values of ΔK^i and ΔV^i are shown graphically in Figure 4.15.

Temporal accuracy of the measurement is given by the rise-time of the detectors that equals 5 ns.

Influence of non-uniform temperature distribution. In data processing, it is always considered that there is a uniform temperature distribution within the area that is being probed by the pyrometer. However, there may exist a non-uniform temperature distribution of the target surface and in this case the pyrometer will measure some effective brightness temperature.

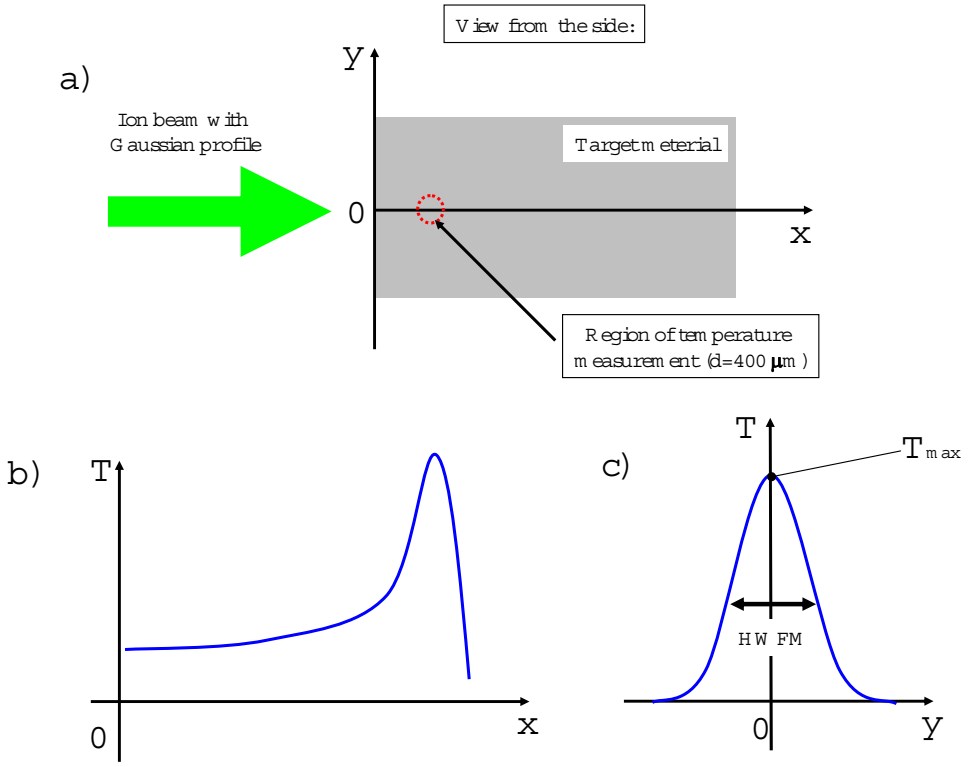

Figure 4.16: Typical spatial temperature distribution arising in experiments with heavy ion beams. Target-beam geometry as it is seen from the side (a), temperature distribution in the x-direction (b) and y-direction (c).

Typical temperature distribution in the experiments with heavy ion beam is shown schematically in Figure 4.17. Distribution in the x-direction is similar to the Bragg curve and can be considered to be constant within 400 μm-probed region. Temperature distribution in the y-direction is determined by the ion beam profile and is close to the Gaussian distribution with a certain FWHM and maximum temperature, $T_{\max}$ (see Figure 4.17). Typical value of FWHM in the performed experiments was 1.5 mm, in few experiments the beam was focused to 0.6 mm FWHM.

Taking this into account, effective brightness temperatures measured by the pyrometer in case of the Gaussian temperature profile in y-direction and constant distribution in x-direction were evaluated. In this evaluation three values of FWHM were considered: 0.6 mm, 1 mm and 1.5 mm (most typical). Deviation of calculated effective brightness temperatures from the maximum temperature, $T_{\max}$ is shown in Figure 4.17. In this figure is seen that in case of the typical value 1.5mm FWHM, the considered inhomogeneous temperature distribution gives error of brightness temperature measurements less than one percent.

Influence of angular dependance of radiation. Another consideration that is done during the calibration of the pyrometer is that there is no dependance of radiation versus observation angle. Normally the radiation depends weakly on angle and the angle dependance can be neglected. For example, in case of solid tungsten, whose

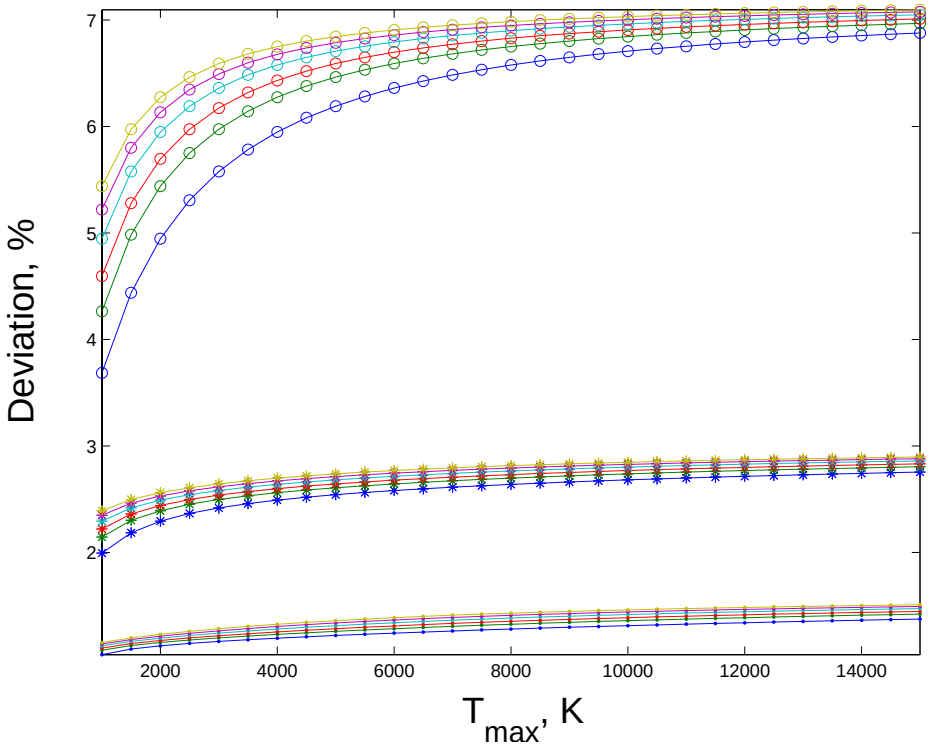

Figure 4.17: Deviation of effective brightness temperatures from the maximum temperature arising due to inhomogeneous heating of the sample with heavy ion beam (see text for more explanations). Blue color — brightness temperature at 550 nm, green — at 750 nm, red — at 900 nm, cyan — at 1100 nm, magenta — at 1300 nm, brown — at 1500 nm. '•' — corresponds to HWFM=1.5 mm, '*****' — HWFM=1 mm, '**o**' — HWFM=0.6 mm.

emissivity differs slightly with the angle: according to [37], the difference between emissivity observed normally to surface and under 90 degrees (in respect to normal) is 2% only.

Stability of fitting procedure. The way to determine the influence of noise on the fitting algorithm is to solve a model problem, in which radiation of the body is represented as black body radiation multiplied by emissivity function whose stability is to be tested [29, 52]. This method is explained schematically in Figure 4.18.

Firstly, black body radiation at working wavelengths of the pyrometer is considered and a certain emissivity model is imposed on it. Grey emissivity is added for uncertainty estimation of "grey" and "ratio" models, linear emissivity is added for uncertainty estimation of the "linear" model. In this way modelled radiation is then recalculated to voltages using calibration coefficients. After this a experimental noise is added to the generated voltages. This data serves as an input to the standart processing algorithm (smoothing, fitting) described in Section 4.3.1. Finally the fitted temperature and emissivity are compared with temperature and emissivity established in the model initially.

Grey emissivity in the presented simulations was set to be 0.3 and linear emissivity was represented as $\epsilon(\lambda, T) = (-2.5 \cdot 10^{-4}) \cdot \lambda + 0.3$. Other model functions of emissiv-

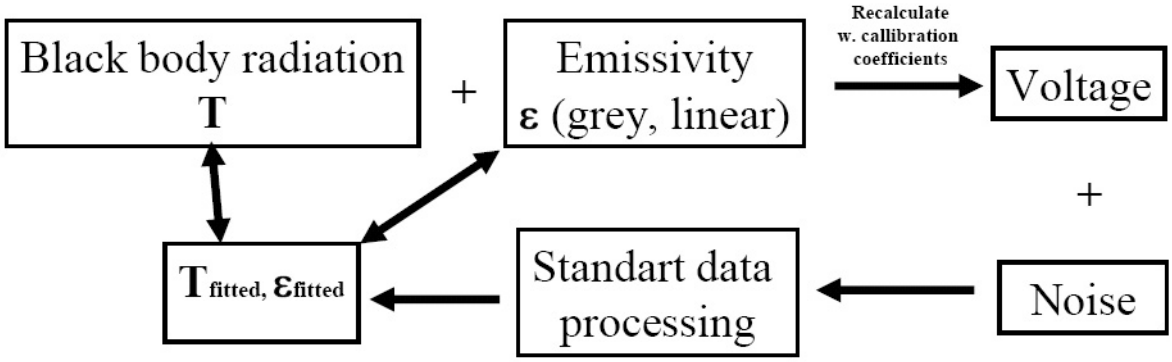

Figure 4.18: Scheme used for errors estimation of fitted temperature and emissivity, see text for more explanation.

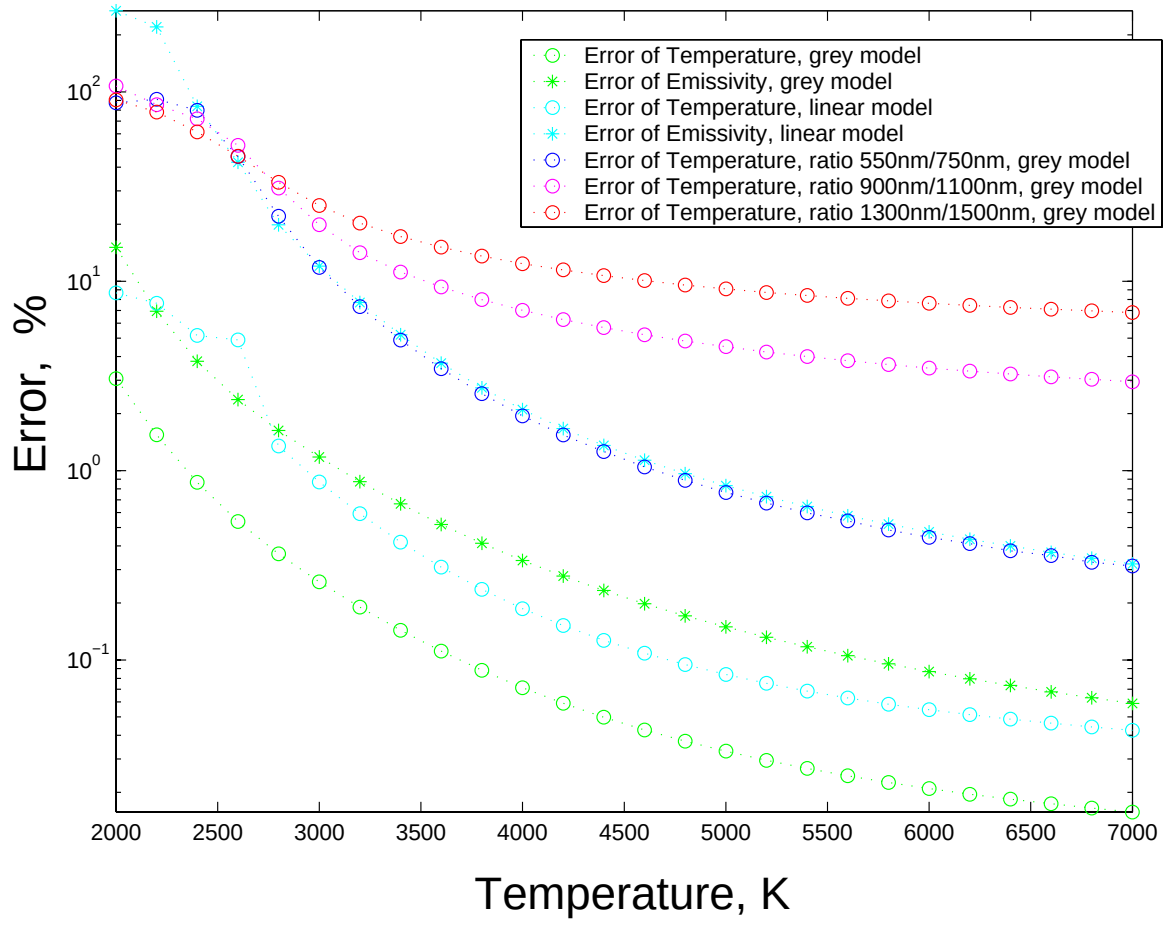

Figure 4.19: Errors of grey, linear and ratio emissivity models induced by the experimental noise. This graph show stability of fitting algorithms in respect to temperature (or signal to noise ratio) obtain from the solution of a model problem (see text for more details).

ity (also temperature dependent) were investigated, but quantitatively they produced similar results.

The results of the error estimations carried out for temperature varying from 2000 K to 7000 K are presented in Figure 4.19. In case of grey and linear fitting functions of emissivity, at T<2500 K noise causes big errors of temperature $\sim$ 10% but starting from 3000 K its influence becomes negligible <1%. Emissivity is more sensitive to the noise and can be trusted completely starting from 4500 K. The "550 nm/750 nm-ratio" temperature can be determined with less than 1% accuracy, whereas the rest combinations, with longer wavelengths, are more sensitive to noise and cannot be measured with precision better than 10%.

As expected fitting of the grey function of emissivity is less affected by noise than the fitting of the linear one. Also it is seen that higher temperatures, means better signal to noise ration, lead to smaller systematic errors.

Errors induced by models of emissivity. Errors in the Figure 4.19 can be understood as follows. If radiation would be exactly linear or grey then the fitting algorithm would give temperatures and emissivity with uncertainty given in this figure. However, one cannot say how close are these models to the true emissivity. In this case the strategy is to compare fitted temperatures with the true temperature determined with some other reliable method [30, 37, 53]. The problem here is that only in limited cases (for example in a static experiments at low temperatures) a pyrometer can be controlled by some other technique.

Nevertheless, a rough estimation based on general representation of radiation of a random body $R = \epsilon \cdot R_{Planck}(\lambda, T)$ (see Section 2.2.2 for more details) can be done. Relation between uncertainty of temperature and emissivity can be then deduced from expression

$$dR = d\epsilon + dT = \frac{\partial R}{\partial \epsilon} \cdot d\epsilon + \frac{\partial R}{\partial T} \cdot dT = R_{Planck} \cdot d\epsilon + \epsilon \frac{\partial R_{Planck}}{\partial T} \cdot dT,$$

which lead to

$$\frac{dT}{T} \approx \frac{\lambda T}{C_2} \cdot \frac{d\epsilon}{\epsilon}.$$

For example, if emissivity calculated by the fit, reproduces the true emissivity with 50% error, then error of temperature, according to the formula will be 20%; if error of emissivity is 20% then error of temperature is 5%. These estimation are done for values of T and λ relevant to performed experiments.

In the following, several cases of application of linear and grey fitting functions to a body with deliberately different emissivity are discussed. The estimation was performed similarly to the scheme in Figure 4.18 with only difference that the fitting function of emissivity and imposed emissivity were on purpose set to be different.

Figure 4.20 illustrates, for example, what happens when a grey model is applied to a body having linear emissivity. It can be seen that in this situation, grey model produces on average 10% of error in temperature determination and $\sim$ 50% in emissivity. The big discrepancy at low temperatures is dominantly due to noise and at higher temperatures, from 2000 K, is already due to an invalid model. In the figure are also shown results for the linear fit, which in an ideal case must converge exactly to the true, modelled

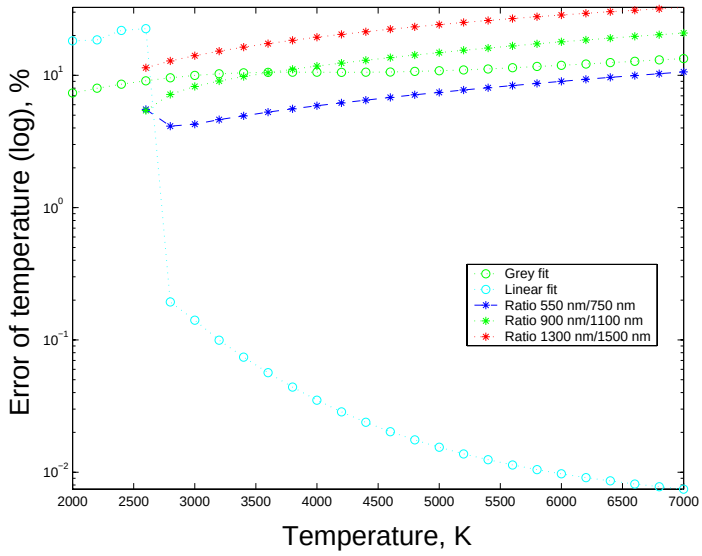

(a)

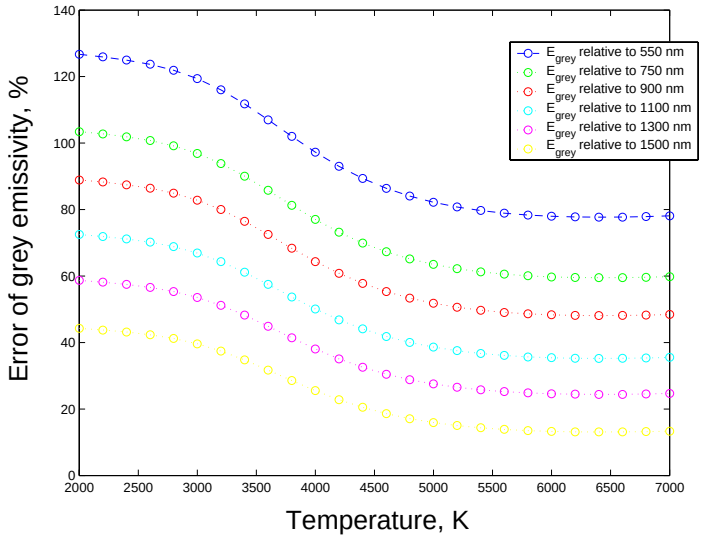

(b)

Figure 4.20: Errors of temperature and emissivity obtained from the solution of model problems for grey, ratio and linear models of emissivity in case when they are applied to a body with a linear behavior of emissivity.

values, but due to presence of noise, there is always a small deviation. Also remarkable in this figure that ratio temperatures based on two wavelengths give in general a bigger error than the grey fit based on six wavelengths.

In addition, to support above estimations experimentally, temperature of the tungsten ribbon lamp (physical temperature of the ribbon versus powering voltage is known)

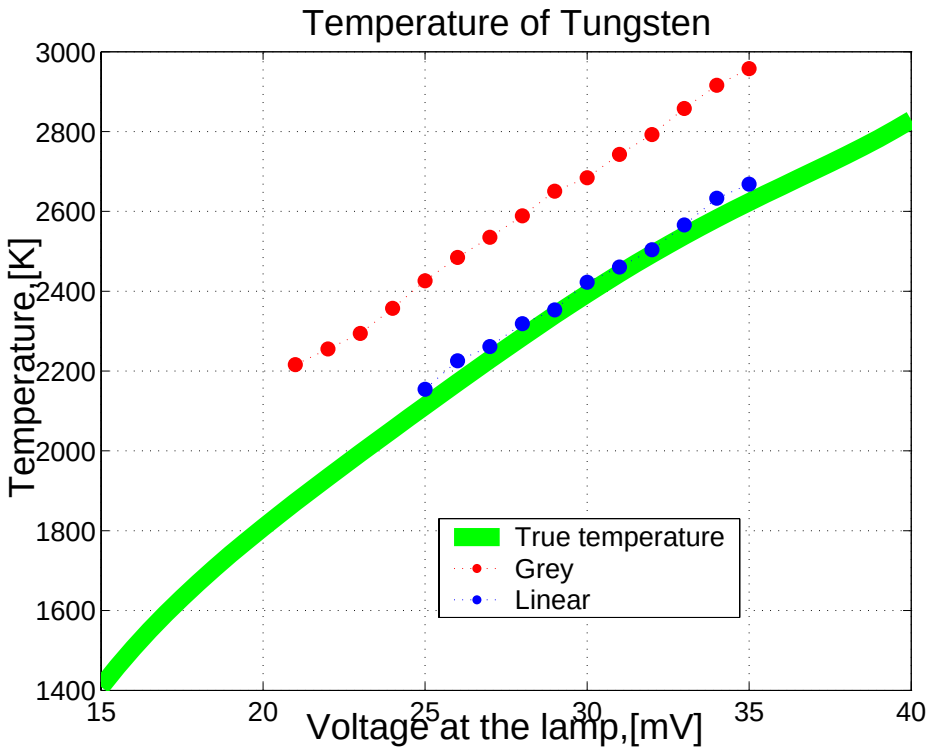

Figure 4.21: Comparison of true and fitted temperature of the tungsten ribbon of the calibration lamp. Radiation of the calibration lamp was measured with the pyrometer and fitted to grey and linear models of emissivity. Physical temperature of the lamp versus powering voltage is known.

was measured with the pyrometer. It is seen in Figure 4.21 that in case of solid tungsten, grey and linear model lead to uncertainties of 15 % and 3 % respectively. These values are consistent with the above simulation. It is to note that, the error of the linear fit in this case is already close to the limit of precision of measured radiances.

	grey radiation	"linear" radiation	tungsten-like radiation
T_{grey}	1%	10%	15%
T_{line}	1%	1%	3%
$T_{550/750}$	3%	10%	7%
$T_{900/1100}$	7%	15%	22%
$T_{1300/1550}$	10%	25%	60%
ϵ_{grey}	2%	-	-
ϵ_{line}	2%	2%	5%

Table 4.6: Summary of all temperature and emissivity errors obtained from the solution of model problems.

Meanwhile, several authors [30, 37, 53] have also applied multi-wavelength pyrometers to various metals and utilized linear and grey models of emissivity for the temper-

ature determination. These experiments included measurements of melted and solid metals with different surface conditions. In these studies temperature could be determined by some different reliable technique (thermocouples, integrating spheres) and due to this, fitted temperatures could be eventually compared with the true value. To summarize, it has been found that fitted temperature had an error varying from 1% up to 20% in the worst case.

Summary All simulation results performed in this section are summarized in Table 4.6. The influence of inhomogeneous heating of the target due to the Gaussian and angular dependance of radiation is less than 1% and thus can be neglected. Errors of brightness temperatures are determined mainly by noise and in average equal to 2%. The stability of fitting algorithms relative to noise is 1%.

5 Experimental results and discussion

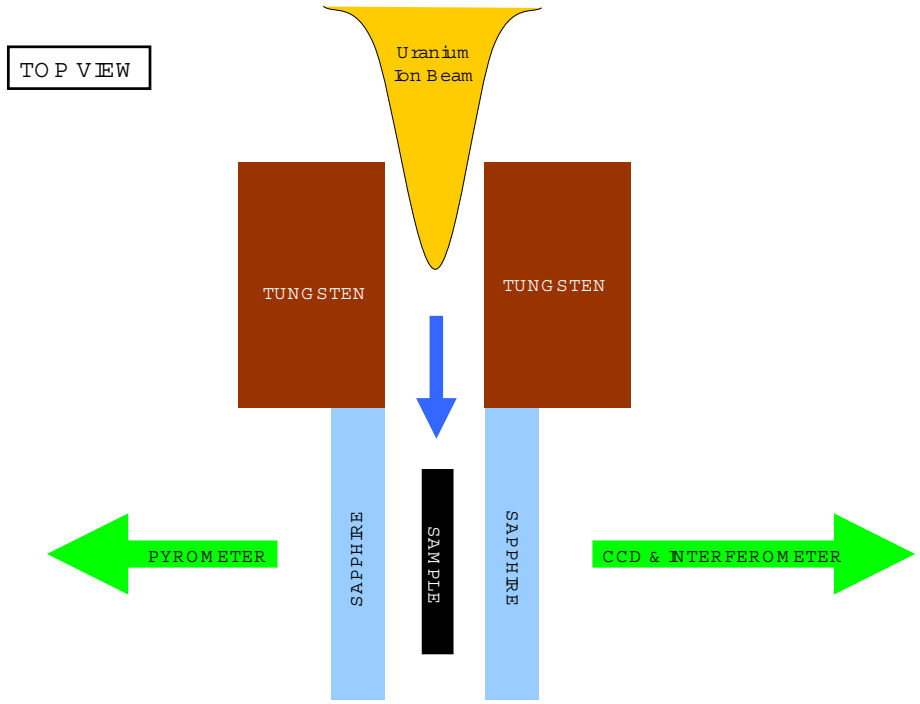

Figure 5.1: Scheme of the plane HIHEX experiment (top view, not scaled). An intense uranium ion beam is focused to a small spot with elliptical profile at the center of a target, thereby heating it rapidly up to rather high temperature, which was measured by the fast multi-channel pyrometer. The uranium beam has a Gaussian-like profile. Sapphire blocks (can be placed at different distances from the sample) and tungsten diaphragm are optional.

Within the work presented in this thesis, HED states in various target materials including copper, aluminum, tungsten, tantalum, sapphire and uranium dioxide were generated by intense, focused uranium ion beams. The results of few representative experiments on studies of thermodynamical properties of tantalum, lead tungsten and sapphire are presented in this section. The beam-target geometry used in these experiments corresponds to the plane HIHEX (see Figure 5.1) concept. The optics of the pyrometer always probed the quasi-constant region of the Bragg-curve of the studied material. For some experiments, in addition to pyrometric records, images of target self-emission and expansion are also presented. The beam profile was deduced from analysis of scintillation of residual argon gas as an approximation of the real profile.

The temporal intensity profile of the heavy ion beam has been recorded by the FCT and absolute amount of particles by the RCT. The FCT signal in always plotted in arbitrary units. All experiments presented below were carried out in vacuum. Melting and boiling temperatures mentioned in the text correspond to normal conditions.

5.1 Experiments with tantalum targets

Energy deposited by the ion beam in experiments with tantalum was sufficient to heat the sample slightly over the melting temperature. Since no rapid expansion of the target can occur, no limiting sapphire walls were installed. A pyrometric record of a typical experiment with tantalum is presented in Figure 5.2 and self-emission image of the target, as recorded by the CCD camera, is shown in Figure 5.3. The streak backlighting record has shown no expansion during the entire 3 μs record time.

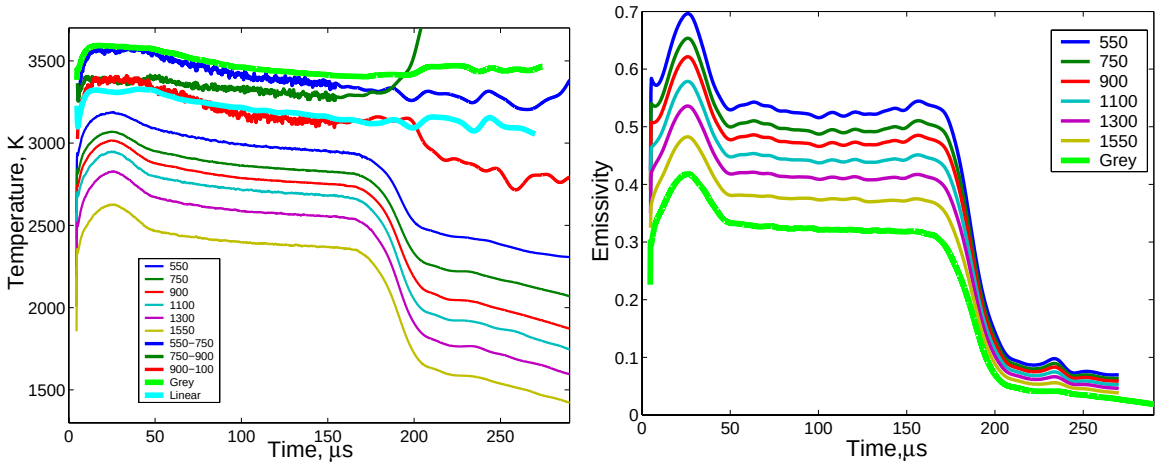

(a) (b)

Figure 5.2: Temperature (a) and emissivity (b) in a typical experiment with a tantalum target. Most of the time the target is in the liquid state. The drop of temperature at 170 μs is attributed to the start of solidification process.

It is seen from Figure 5.2 that all temperature variations occur near the normal melting temperature of tantalum ($T_{melt} = 3290\ K$). Thus, thermodynamical states of the sample during the experiment are located on the phase diagram close to the melting curve and most of the record length 170 μs, the pyrometer measures temperature of liquid tantalum.

The grey, linear and ratio temperatures in Figure 5.2 build a discrepancy corridor which has a width of approximately 200 K. This value can be accepted as a rough error estimation of 5% of the temperature measurement in this experiment.

There are two main mechanisms of energy dissipation from the sample in this experiment: thermal radiation and material evaporation. These processes both occur at the surface of the sample and hence, the sample loses energy only from the surface.

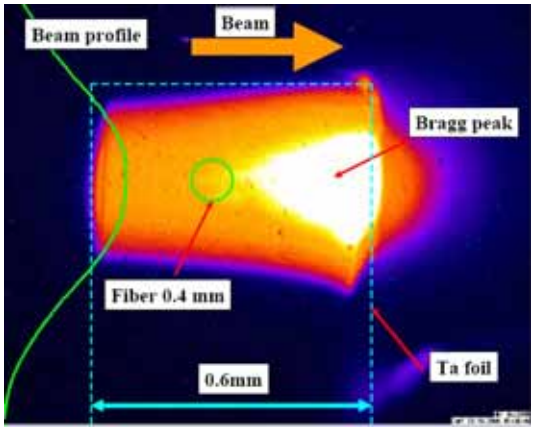

Figure 5.3: Image of a tantalum target during ion-beam irradiation recorded by the side CCD camera. The blue dashed line represents the initial dimension of the tantalum foil (0.05 mm thick). Also shown: the ion beam profile determined from the scintillation in argon gas (green curve) and the position of the 400 μm probing fiber (green circle). The stopping range of an uranium in tantalum is 2.44 mm; beam intensity was $1.55 \cdot 10^9$ particles/bunch.

The bulk of the target is cooled by the continuous heat flow from the hot interior to the colder surface (temperature distribution in this case is similar to the profile depicted in Figure 2.4 of Chapter 2).

According to evaluation formulas in Chapter 2, the specific energy lost in this experiment by thermal radiation during 200 μs at 3500 K is $\approx 10^{-3}$ J. Meanwhile the specific internal energy of the foil at 3500 K is $U_s = C_s \cdot T \approx 400$ J, where C_s is the specific heat capacity of tantalum. It is seen that energy radiated by the sample during 200 μs is a tiny fraction of the total internal energy and thus energy dissipation due to surface radiation is negligible at the time scale of the measurement. Therefore, thermal surface evaporation of material to vacuum is the dominant dissipation mechanism here.

The vapor pressure near the surface equals pressure of the saturated tantalum vapor (low, since tantalum is a heavy element [11]). Due to the relatively low temperature of the vapor, its ionization degree is negligible. Such vapor is optically transparent and does not obscure the hot liquid component.

The temperature growth, during the first 10 μs is in contradiction with the 120 ns FWHM duration of the ion beam pulse (see Figure 5.2). The nature of this phenomena becomes clear by observing Figure 5.3. Since the length of the target is almost the same as the range of the uranium beam, a much hotter part of the target exist which corresponds to the Bragg-peak of the uranium beam in tantalum. Thus the temperature increase detected by the pyrometer is simply due to heat flow from the hotter (Bragg-peak) part towards the cooler part of the target.

During the time interval from 50 μs to 150 μs in Figure 5.2, temperature continuously goes down while emissivity remains unchanged. Such a behavior of a liquid metal next to the melting temperature is well known. It represents an experimentally validated fact that emissivity of a melted metal above the melting temperature equals

to emissivity at the melting point (see [34, 39] and references therein).

At approximately 170 μs, the pyrometer detected a rapid decrease of brightness temperatures and emissivity, while fitted "grey" and "linear" temperatures show no change. Such a behavior could be attributed to a phase transition, most probably solidification. This event was observed in all experiments with tantalum, from which it can be concluded that during the relaxation process from liquid to solid state, tantalum sample was always passing through the same phase state.

Several authors have studied solidification of tantalum droplets during a free fall, utilizing a ultrahigh vacuum drop tube technique [54,55]. In these experiments, brightness traces of the solidification of highly undercooled tantalum droplets gave an evidence of two successive phase transitions on the way from liquid to solid state. Each of these transitions showed a temperature increase of approximately 300 K in brightness temperature at 800 nm. Intermediate meta-stable phases between these temperature changes were interpreted as a liquid phase having fraction of *A15* (at 2770 K) after the first temperature increase and *bcc* (at 2930 K) crystalline structures after the second temperature increase respectively.

However, in the experiments with heavy ion beams no such peculiarities were observed. One of the explanation could be that the energy loss rate in these experiments was low, due to the plane geometry in comparison to the spherical (drop) geometry and thus meta-stable undercooled states could not be generated.

5.2 Experiments with lead targets

In experiments with lead, different target configurations having various foil thicknesses and gap sizes between the target and the constraining sapphire have been implemented. Obtained temperature measurement results of three typical experiments are shown in Figure 5.4, Figure 5.5 and Figure 5.6 respectively. In addition to temperature, the relative expansion of targets[1] measured with the streak backlighting technique is shown in Figure 5.5 and Figure 5.6. Beam-target parameters in these experiments are listed in Table 5.2.

Experiment:	Width:	Intensity:	Gap:	FWHM:	Shot name:
1	240 μm	$1.28 \cdot 10^9$	220 μm	200 μm	Shot25, December 2004
2	240 μm	$1.36 \cdot 10^9$	2300 μm	200 μm	Shot22, December 2004
3	100 μm	$1.61 \cdot 10^9$	2500 μm	120 μm	Shot192, December 2005

Table 5.1: Parameters of ion beam and target in experiments with lead.

In all three experiments energy deposited by the uranium ion beam was enough to melt ($T_{melt} = 600\ K$) and to evaporate ($T_{boil} = 2000\ K$) the sample. The thermodynamic state of the target changed from solid (at room temperature) to hot gas, passing through an intermediate liquid phase. All pyrometric records have a similar

[1] i.e. the width of the foil at different times normalized by the initial width

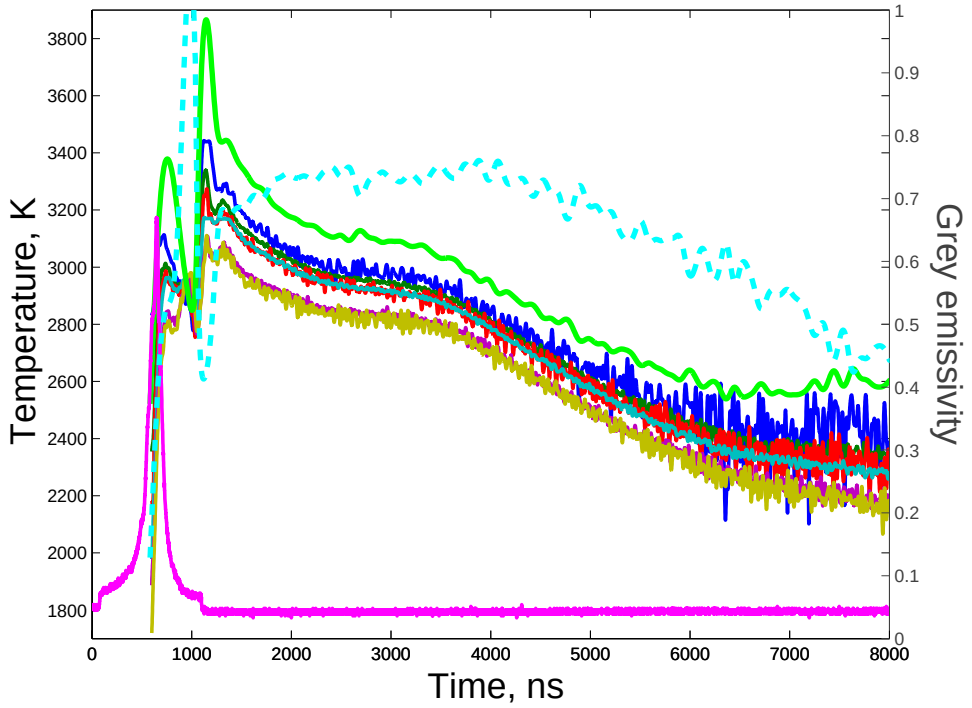

Figure 5.4: Temperature and grey emissivity of the lead target in Experiment-1 (see Table 5.2 for more experimental details). Blue line – brightness temperature at 550 nm, green – at 750 nm, red – at 900 nm, cyan – at 1100 nm, violet – at 1300 nm and brown – at 1500 nm. Magenta line – FCT signal, thick green – grey temperature, dashed cyan – grey emissivity.

behavior which may be interpreted as follows. The initial increase of the temperature can be related to melting and evaporation of the whole target accompanied by expansion of the sample. While expanding, vapor is rapidly cooling down and at the time when its temperature becomes sufficient for homogeneous nucleation (near the vapor spinodale line), liquid droplets appear inside the vapor and the material becomes a two phase (gas-liquid) mixture [11]. Since the expansion takes place in vacuum, the liquid and vapor states are not in equilibrium and the vapor cannot become saturated. This causes continuous material surface evaporation of droplets, which is responsible for temperature decrease clearly seen in the pyrometric records.

As it is shown in reference [56], up to 10000 K lead vapor is weakly ionized and optically transparent. During the expansion the pyrometer measures radiation of hot lead droplets, which have thermodynamical states close to the binodale line. Such a radiation object consisting of many droplets is very complicated and lies far beyond the working conditions of the pyrometer, as no distinct radiation layer and surface are available. Consequently the grey and linear model are not capable to describe such a process and fail by producing values of emissivity larger than 1 and fitted temperatures lower than brightness ones (see Figure 5.4 and Figure 5.5).

At some moment in time, the expanding target material that consists of a mixture of vapor and droplets, impacts against the sapphire wall. This impact leads to compression and heating of the sample. According to the EOS model [57], such weak

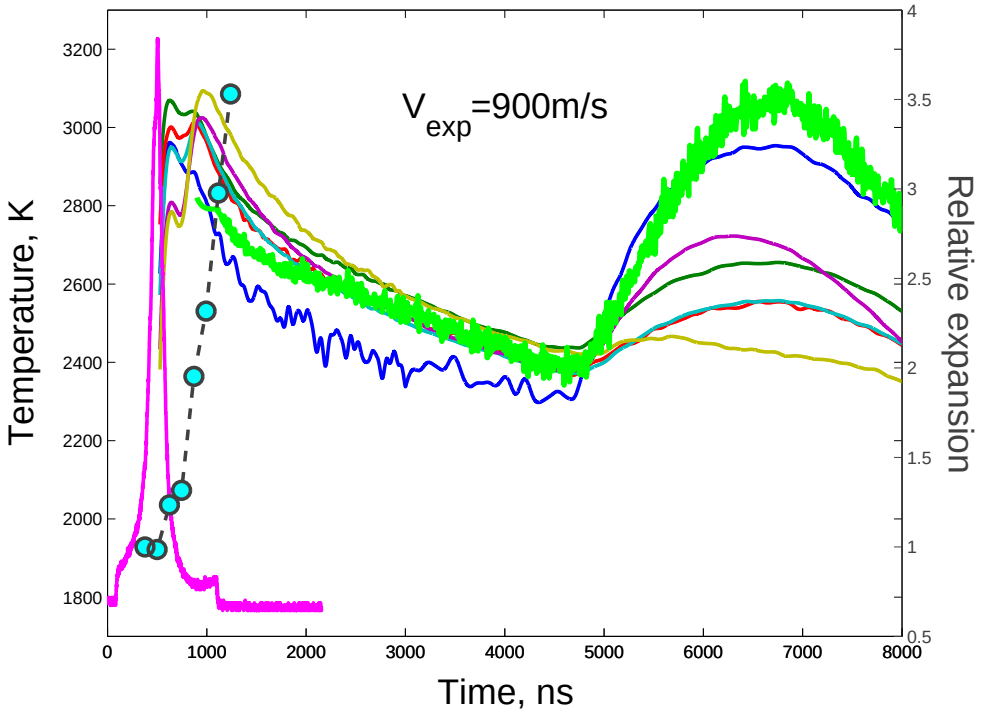

Figure 5.5: Temperature and expansion of the lead target in Experiment-2 (see Table 5.2 for more experimental details). Blue line – brightness temperature at 550 nm, green – at 750 nm, red – at 900 nm, cyan – at 1100 nm, violet – at 1300 nm and brown – at 1500 nm. Magenta line – FCT signal, thick green – grey temperature, filled circles – relative expansion of target.

quasi-isentropic compression will transform the material into pure vapor state and the droplets will disappear. On the other hand, a certain time is needed for such a transformation. Therefore, if the heating rate is high enough, the liquid droplets can be overheated up to spinodale temperatures. To realize such overheated states at pressures below the critical point, one would need a heating rate dT/dt which is at least higher than 10^9 K/s [58].

In the experiment with short expansion length (Figure 5.4), at the time of impact on the sapphire window, the heating rate was about $dT/dt = 2.2 \cdot 10^{10}$ K/s and the overheating may have taken place according to [58]. In the experiment with the longer expansion length, the heating rate at the time of impact was considerably smaller, $dT/dt = 1.5 \cdot 10^9$K/s (Figure 5.5) and $dT/dt = 3.5 \cdot 10^9$ K/s (Figure 5.6) respectively and the overheating process must have not taken place.

In all experiments with a 200 μm thick target foil, brightness temperatures at times corresponding to the first peak of around 1000 ns have a distinct wavy structure as it is seen in Figure 5.4 and Figure 5.5. Meanwhile this structure was not observed in experiments with thinner, 100 μm thick foils, i.e. the first peak was smooth as it is in Figure 5.6.

A qualitative, plausible explanation is that for thicker foils, the energy deposition is not uniform in the transverse direction, with most energy deposited in the center of the target. This leads to pressure gradients, which create compression waves that

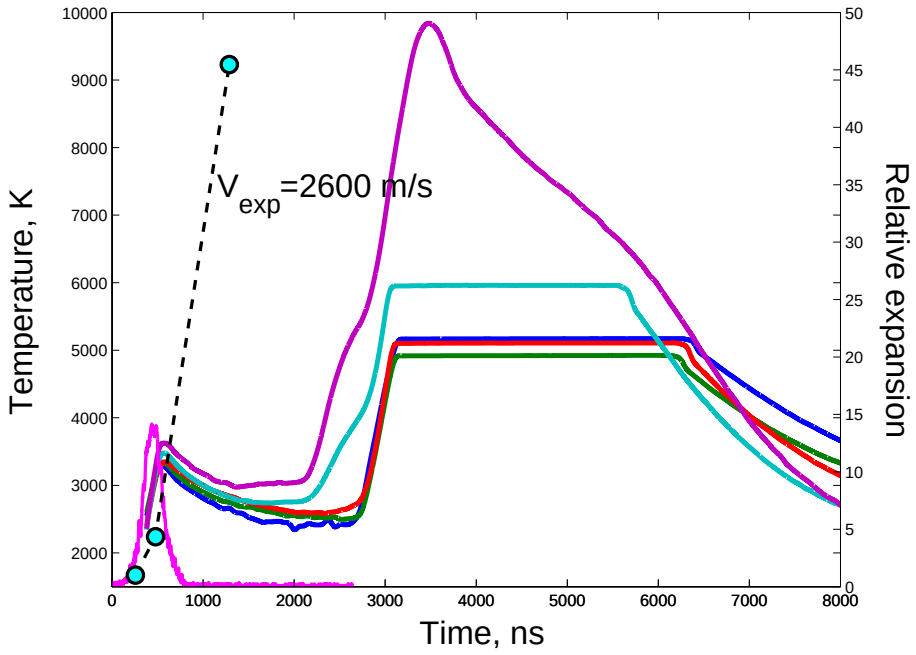

Figure 5.6: Brightness temperatures and expansion of the lead target in Experiment-3 (see Table 5.2 for more experimental details). Blue line – brightness temperature at 600 nm, green – at 700 nm, red – at 900 nm, cyan – at 1200 nm and violet – at 1500 nm. Magenta line – FCT signal, filled circles – relative expansion of target.

propagate back and forth with sound velocity in the transversal direction. As the result, the surface of the target and the radiative layer are disintegrated (perturbed), which is indeed reflected in the wavy structure in the brightness temperatures behavior. Meanwhile, in case of thin foils, the energy deposition is more uniform, since the foil is narrower than the beam and hence strong transverse pressure gradients do not occur. Therefore for experiments with current beam focal spot sizes, thin foils width $\leq$100 μm are more favorable.

In addition to pyrometric data, radiation spectrum from 430 nm to 760 nm was recorded by the streak-spectrometer during target irradiation. An intense, beam-induced scintillation, similar to Figure 5.7a, was observed in most of the experiment with lead. Two distinct lines centered at 505 nm and 525 nm can be seen sitting on top of the thermal background. Taking this into account, the pyrometer filter corresponding to 550$\pm$20 nm was excluded from all fitting procedures.

Relatively high temperature and expansion speed were observed in the Experiment-3 (see Figure 5.6 and Figure 5.7b). The brightness temperature at 1500 nm reached 9900 K, whereas the physical temperature could not be calculated, since most of the channels were saturated. However, one may conclude that peak physical temperature was not less than 9900 K, since brightness temperature is always equal or less the physical one. Anyway, this temperature values is already above the critical temperature, $T_{cr} = 5500\ K$, of lead and this experiment may serve as the first demonstration that overcritical entropy states in lead targets can be achieved, even with existing parameters of the uranium ion beam.

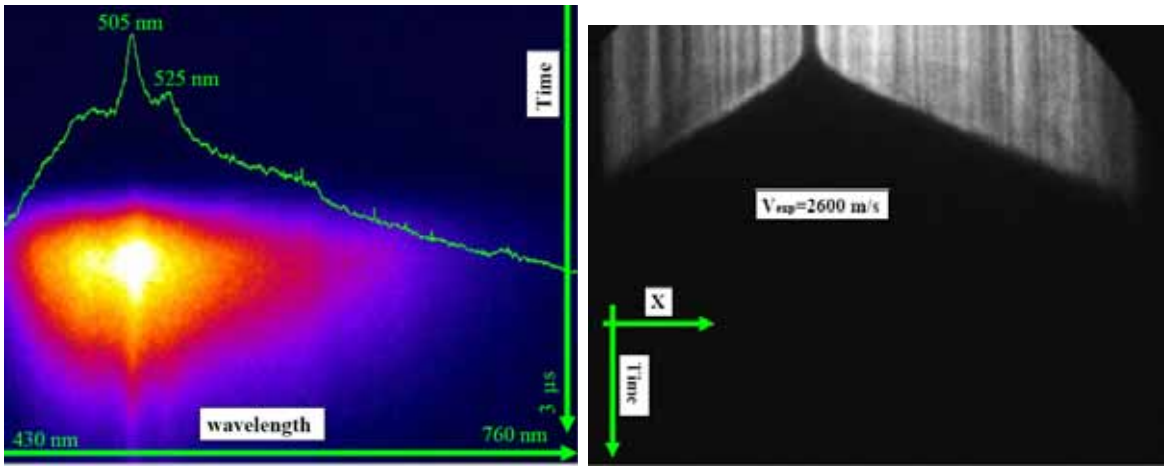

(a) (b)

Figure 5.7: Self-emission spectrum (a) and expansion dynamics (b) of the lead target in Experiment-3.

The high energy deposition in this experiment became possible due to focusing of a uranium ion beam to a relatively smaller spot with =120 μm FWHM in the horizontal plane. This focusing could be achieved utilizing improved electron cooling of the ion beam within the SIS-18 ring.

5.3 Experiments with tungsten targets

Experiment:	Width:	Intensity:	Gap:	FWHM:	Shot name:
1	240 μm	$1.05 \cdot 10^9$	2300 μm	300 μm	Shot2, Oktober 2005
2	100 μm	$1.52 \cdot 10^9$	2300 μm	120 μm	Shot199, December 2005
3	100 μm	$1.93 \cdot 10^9$	2300 μm	200 μm	Shot57, Oktober 2005

Table 5.2: Parameters in experiments with tungsten.

Three representative experiments with solid (see Figure 5.8), melted (see Figure 5.9) and evaporated (see Figure 5.11) tungsten targets are presented in this section. Beam-target parameters in these experiments are summarized in Table 5.3. All experiments were carried out in vacuum and the only constrain for free expansion were the observation windows of the protective casing (see Figure 3.3). Melting temperature of tungsten is 3695 K and boiling temperature is 5800 K. In the first kind of experiments shown in Figure 5.8, the tungsten target was heated up to 3000 K and during the entire record time it was measuring cooling of the solid slightly heated tungsten foil.

In the second kind of experiments shown in Figure 5.9, tungsten target was heated above the melting temperature and remained most of the time in the liquid state. In

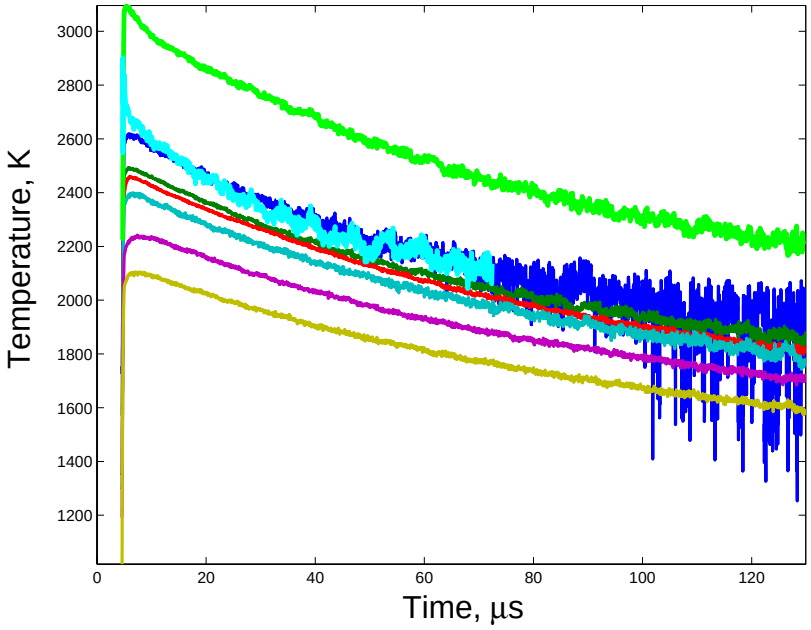

Figure 5.8: Temperature of tungsten target in Experiment-1 (see Table 5.3 for more details). Cyan line – T_{line}, green – T_{grey}, blue – $T_{brightness}$ at 550 nm, dark green – $T_{brightness}$ at 750 nm, red – $T_{brightness}$ at 900 nm, light blue – $T_{brightness}$ at 1100 nm, magenta – $T_{brightness}$ at 1300 nm, brown – $T_{brightness}$ at 1500 nm. The sample in this experiment remained in the solid state.

Figure 5.10 are shown images recorded in this experiment by the side CCD camera and backlighting streak camera.

The temperature records from this experiment show an unexpected fitted temperature growth at 50 μs and a simultaneous drop in the brightness temperature. This increase in temperature is contradictory, since no heat sources are available in the system after such a long period of time (the ion beam lasts only for 120 ns FWHM) and temperature should normally decrease. One of the explanations of this phenomena could be as follows. The liquid tungsten target continuously evaporates at its free surface. The fast expanding component (70 m/s) in Figure 5.10 may be identified as vapor which is followed by slower (7 m/s) expanding liquid. Knowing the distance between the target foil and the observation window, impact time of the vapor with the window can be estimated $\approx$ 50 microseconds. This is exactly the time when the anomalous temperatures growth is observed. When the vapor interacts with the cold wall it cools down and condensates on it, what causes a change in the optical transmission of the sapphire window. In this case the calibration of the pyrometer is not valid anymore and as the result, fitted and brightness temperature have wrong values. Therefore data in this experiment cannot be trusted after 50 μs, since the window becomes contaminated. Meanwhile, before this contamination occurs, the pyrometer data is reliable and temperature of the liquid component of the target is measured indeed, since the vapor is optically transparent.

In the experiment shown in Figure 5.11, the ion beam was focused to a smaller focal

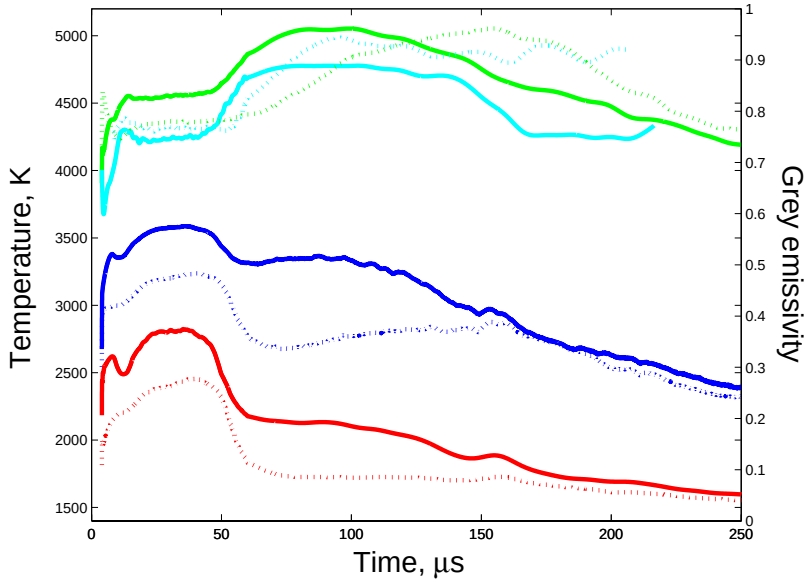

Figure 5.9: Temperature and emissivity of the tungsten target in Experiment-2 measured by both legs of the pyrometer (see Table 5.3 for more details). Cyan line – T_{line} fitted for Leg-1, cyan dashed – T_{line} fitted for Leg-2, green – T_{grey} fitted for Leg-1, green dashed – T_{grey} fitted for Leg-2, blue – $T_{brightness}$ at 900 nm measured by Leg-1, blue dashed – $T_{brightness}$ at 900 nm measured by Leg-2, red – ϵ_{grey} fitted for Leg-1, red dashed – ϵ_{grey} fitted for Leg-2. The sample in this experiment was melted.

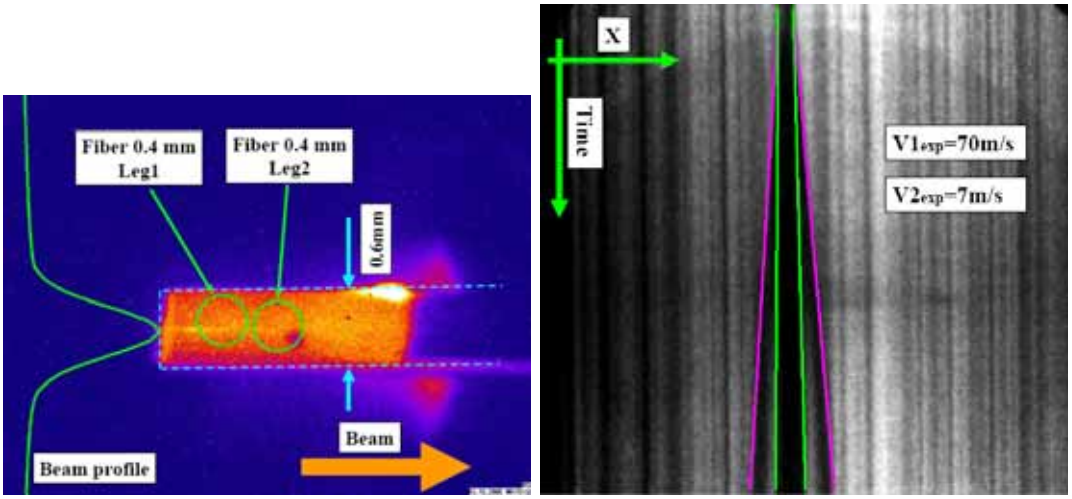

(a) Self-emission image of tungsten target. Also shown positions of probing fibers and the ion beam profile in the vertical plane.

(b) Expansion dynamics of tungsten target.

Figure 5.10: Self-emission image and expansion dynamics of the tungsten target in Experiment-2.

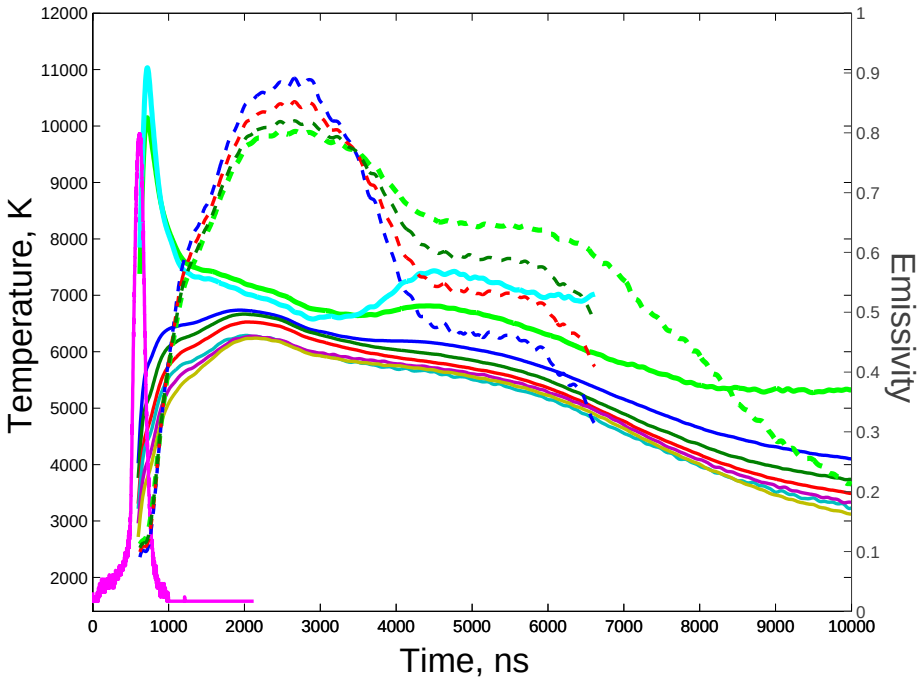

Figure 5.11: Temperature and emissivity of the tungsten target in Experiment-3 (see Table 5.3 for more experimental details). Cyan line – T_{line}, green – T_{grey}, blue – $T_{brightness}$ at 550 nm, dark green – $T_{brightness}$ at 750 nm, red – $T_{brightness}$ at 900 nm, light blue – $T_{brightness}$ at 1100 nm, magenta – $T_{brightness}$ at 1300 nm, brown – $T_{brightness}$ at 1500 nm, dashed green – ϵ_{grey}, dashed blue – ϵ_{line} at 550 nm, dashed dark green – ϵ_{line} at 900 nm, dashed red – ϵ_{line} at 1500 nm. The sample in this experiment was partially evaporated.

spot 120 μm FWHM in the horizontal plane, which lead to higher energy deposition in the target. It is remarkable that fitted temperature at the times around 1000 ns have different behavior in comparison to brightness temperatures: both grey and linear temperature fits[2] produced a sharp peak, while brightness temperatures behave more smoothly. In a some way, fitting has revealed additional information which cannot be obtained from brightness temperatures.

In the streak backlighting record of this experiment, shown in Figure 5.12, two expanding components of the target are seen: a fast (780 m/s) and a slow one (7 m/s). The fitted temperature in Figure 5.11 is higher than the boiling temperature of tungsten and the target must be in the gaseous state expanding with high velocity as it occurs in the experiments with lead. Meanwhile, the streak record has also the weakly expanding fraction of the target material present, even after 3 μs. One may identify this slow component a as a liquid one, which could not be completely evaporated by the beam. From the other hand, according to the fitted results, the temperature was far above the boiling temperature and complete evaporation should haven taken place. Meanwhile as the heating rates are relatively high, a meta-stable state may be in principle generated. For example, the dark part in the streak record could be simply slow

[2]Examples of the fitting of the experimental points to the modelled radiation in this experiment are shown in Figure 4.13

expanding superheated liquid. However, in order to validate this hypothesis a deeper analysis based on numerical simulation is required.

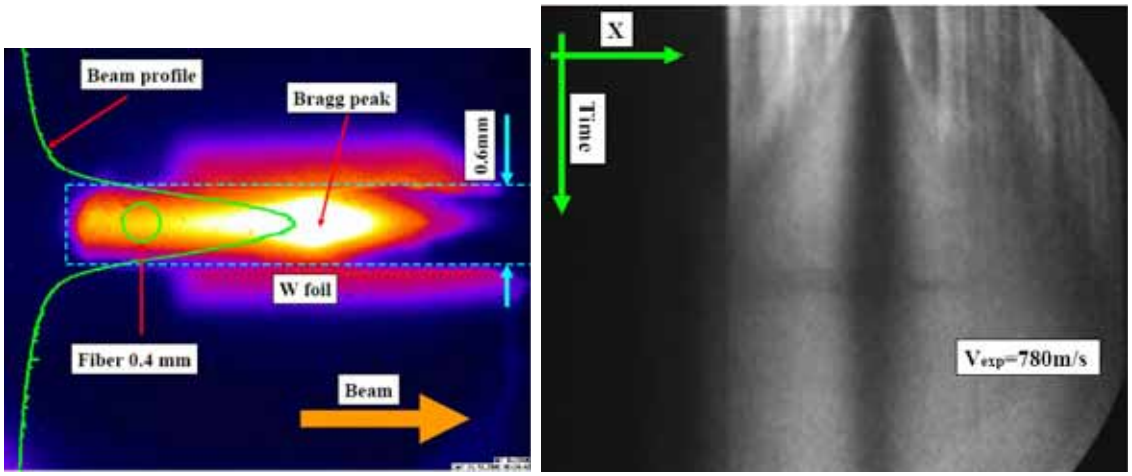

(a) Self-emission image of tungsten target. Also shown are the position of probing fiber and the ion beam profile in the vertical plane.

(b) Expansion dynamics of tungsten target.

Figure 5.12: Self-emission image and expansion dynamics of tungsten target in Experiment-3.

5.4 Experiments with sapphire targets

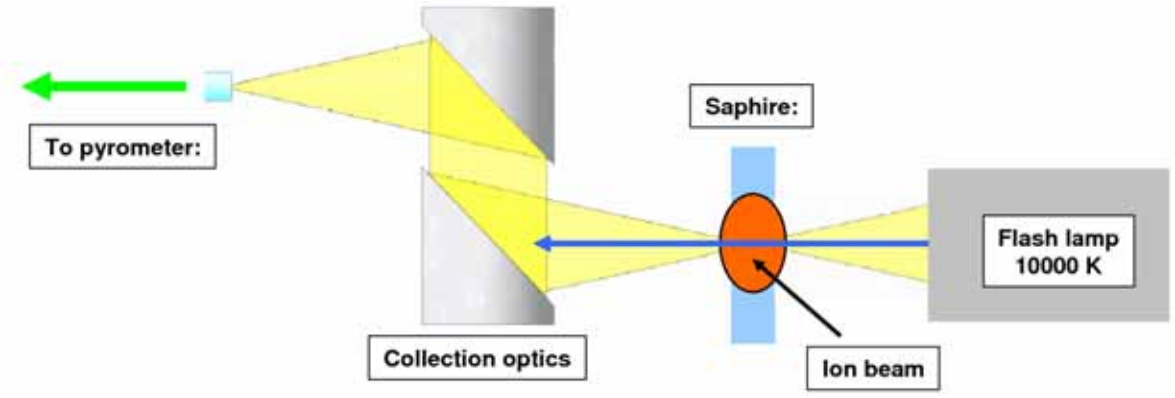

Figure 5.13: Experimental scheme for the study of sapphire transmission during the ion beam irradiation.

Pyrometric measurements of shock-heated metals are often performed through a transparent window acting as a shock anvil. Sapphire is an interesting material because of its rather high shock impedance and thermal strength. According to [63],

influence o emission and absorption effects appears in optical pyrometry experiments when sapphire is shocked above its Hugoniot elastic limit, which lies in the Mbar pressure range. In the experiments with heavy ion beams, sapphire is used as an observation window and as a confining wall for the hot expanded target with maximum pressure not exceeding several kbar. Thus any changes of optical properties during the interaction with a hot sample can be neglected. However, they may appear during the direct interaction with an ion beam, since the beam affects the electronic structure of the material, upon which optical properties usually depend.

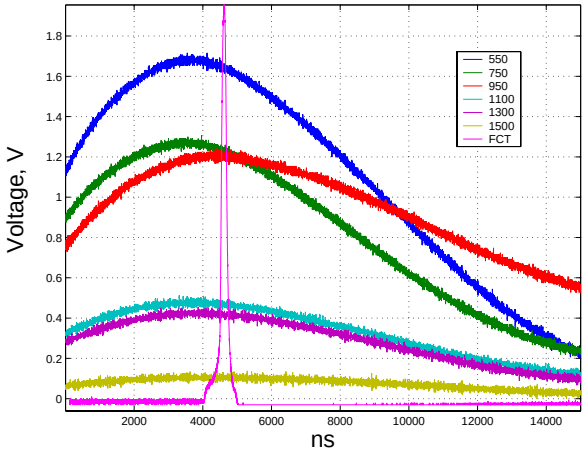

Figure 5.14: Reference curves (in Volts) recorded by the pyrometer channels during the xenon flash irradiation. Also shown the FCT record marking the arrival of the beam (magenta line). For higher accuracy, the peak output of the flash is chosen to coincide roughly with the arrival of the beam.

Normally a tungsten or tantalum diaphragm collimates the ion beam (see Figure 5.1), so that energy of the beam is deposited only in a target. Nevertheless, it may happen that at certain gap sizes, a fraction of the beam is not stopped completely in the diaphragm and inevitably interacts with the sapphire walls. Interaction with the beam leads to scintillation, reduction in optical transmission and heating of the sapphire sample wall itself.

Several scenarios of sapphire-beam interaction with various relative positions (between beam axis and sapphire) were investigated in this work and two kinds of experiments were carried out. In the first kind of experiments, changes in the optical transmission of a sapphire sample were measured by employing the pyrometer and a powerful xenon flash lamp simultaneously. The self-emission of the sapphire during beam irradiation was measured in the second kind of experiments, where only the pyrometer was involved.

The experimental scheme for the study of optical transmission of a sapphire sapphire during the ion beam irradiation is presented in Figure 5.13. A standard sapphire block is placed at the focus of the ion beam. Before every experiment, this block is illuminated from the side by an intense flash lamp. The optics of the pyrometer collects all light transmitted by the sapphire and guides it to the pyrometer. The corresponding pyrometric records, V_{ref}, are stored and serve as reference signals (see Figure 5.14).

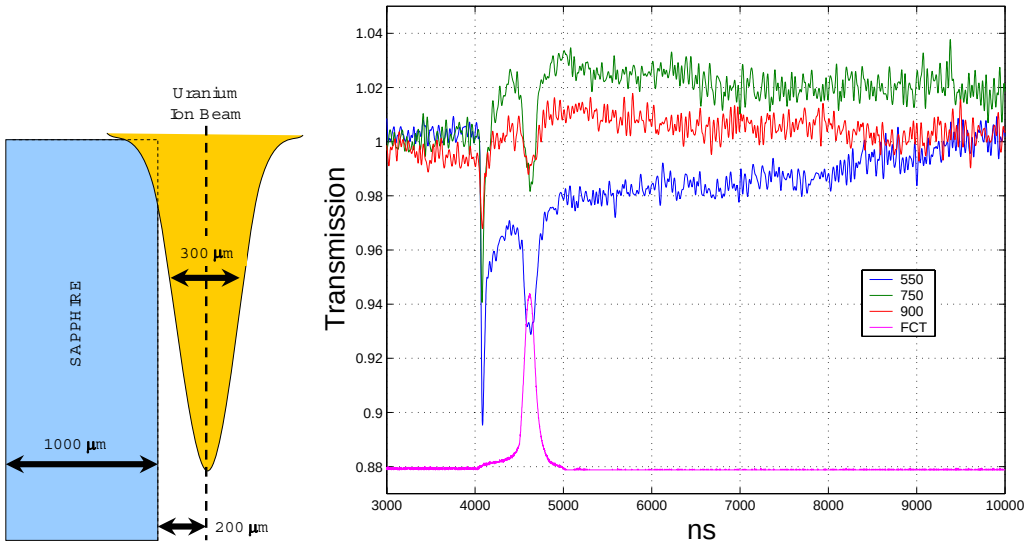

(a) Position of beam relative to the sapphire block (not scaled).

(b) Transmission of the sapphire sample.

Figure 5.15: Transmission of the sapphire sample at various wavelengths during ion beam irradiation: the center of the beam is 200 μm away from the sapphire surface. Beam intensity in this experiment was $1.28 \cdot 10^9$ particles bunch (Shot15, October 2005).

As the next step, without changing the arrangement, the same sapphire is irradiated by an ion beam and at the same time illuminated by the lamp in the way it was done in the reference shot. Since the only difference in comparison to the reference shot, is the presence of the ion beam, any changes are attributed to perturbations produced by heavy ions. Transmission at every channel of the pyrometer and at every moment of time is obtained by dividing the record obtained with the beam, V_{beam} by the reference record, V_{ref}.

$$\text{Transmission} = \frac{V_{\text{beam}}}{V_{\text{ref}}}.$$

This ratio is close to the true optical transmission, since the intensity of self-emission of a sapphire (as it will be shown later, this intensity corresponds to $\approx$ 3000 K) is much lower than the intensity of the flash lamp (temperature of flash is 10000 K) and thus, the self-emission at most of wavelengths can be neglected.

In Figure 5.15 is shown the result of an experiment, where the beam touches slightly the right side of a sample with the "Gaussian wing". Values of transmission over 1, mean that self-emission of sapphire was comparable with level of the reference signal. In this geometry of the experiment, the ion beam has caused temporal reduction in transparency but the sample itself remained undamaged. It is seen that during the interaction, the sapphire looses its transmission qualities at 550 nm, 750 nm and 900 nm while no changes at longer wavelengths (not shown in figure) were observed.

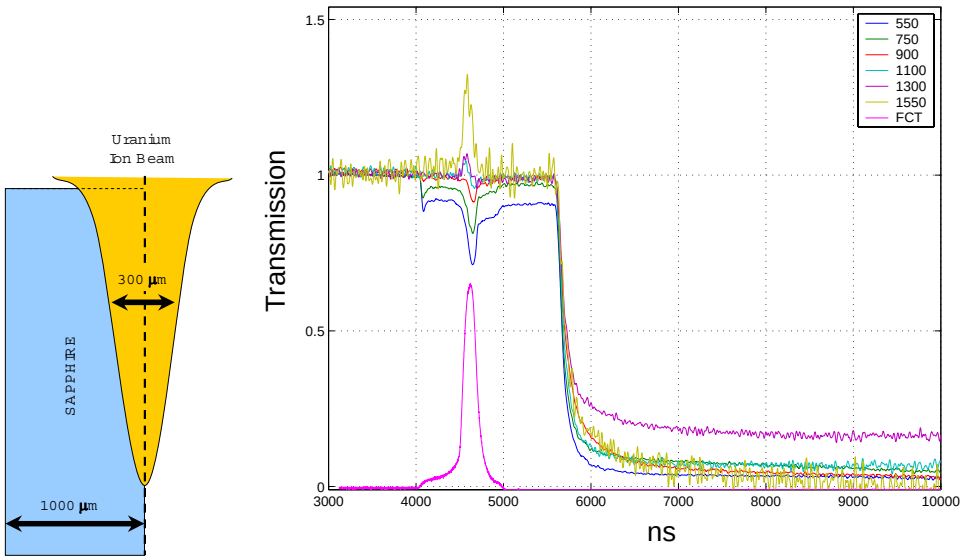

(a) Position of beam relative to the sapphire block (not scaled).

(b) Transmission of the sapphire sample.

Figure 5.16: Transmission of the sapphire sample at various wavelengths during ion beam irradiation: half of the beam interacts with sapphire. Beam intensity in this experiment was $1.05 \cdot 10^9$ particles/bunch (Shot22, October 2005).

After approximately 6 μs the transmission gradually returns to its initial state. This transparency reduction can be interpreted by the appearance of free electrons, which absorb light of the flash lamp. These free electrons may originate from the stripping of uranium ions as they propagate in the material.

The situation changes dramatically in the next two experiments, in which a half of the beam (Figure 5.16) and the entire beam (Figure 5.17) deposited their energy into sapphire respectively. In both cases, this interaction leads to heating of the sapphire to relatively high temperatures and its consequent destruction. The samples remain transparent for 1.5 μs after the end irradiation and then become irreversibly opaque. It is still not understood, why the sample becomes opaque several microseconds delayed even though the entire energy was already deposited earlier.

The fact that a body becomes opaque (means optically thick) indicates that its radiation should in principle gain a thermal character. In order to validate this, in the next series of experiments, only self emission of sapphire without the flash lamp, was measured. In Figure 5.18 is shown an experiment where the beam was aligned to the center of the sample as it was done in the experiment shown in Figure 5.17. During the first 1.5 μs the radiation is the superposition of thermal spectra and scintillation and later times radiation becomes thermal, making it possible to fit data to the grey body model.

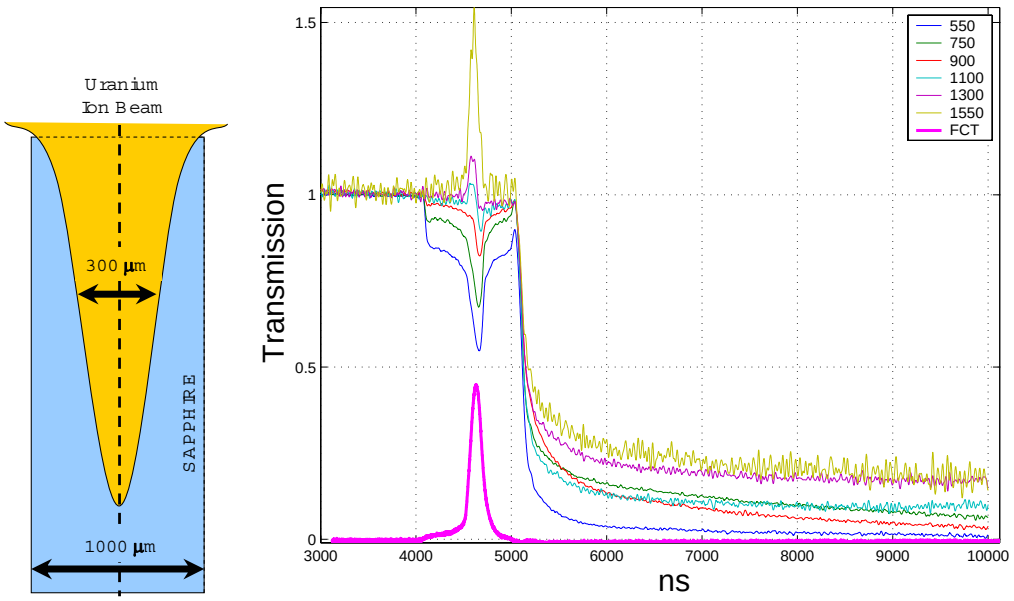

(a) Position of the beam relative to the sapphire block (not scaled).

(b) Transmission of the sapphire sample.

Figure 5.17: Transmission of the sapphire sample at various wavelengths during ion beam irradiation: the whole ion beam interacts with the sapphire sample. Beam intensity in this experiment was $1.87 \cdot 10^9$ particles/bunch (Shot26, October 2005).

The melting temperature of sapphire is approximately 2300 K, and fitted temperature is about 2600 K, thus the sapphire was melted. This could be an explanation of the opacity. However other reasons for the sapphire becoming opaque are possible. For example, the loss of transparency could be attributed to formation of micro cracks that scatter light and thereby reduce the transmission.

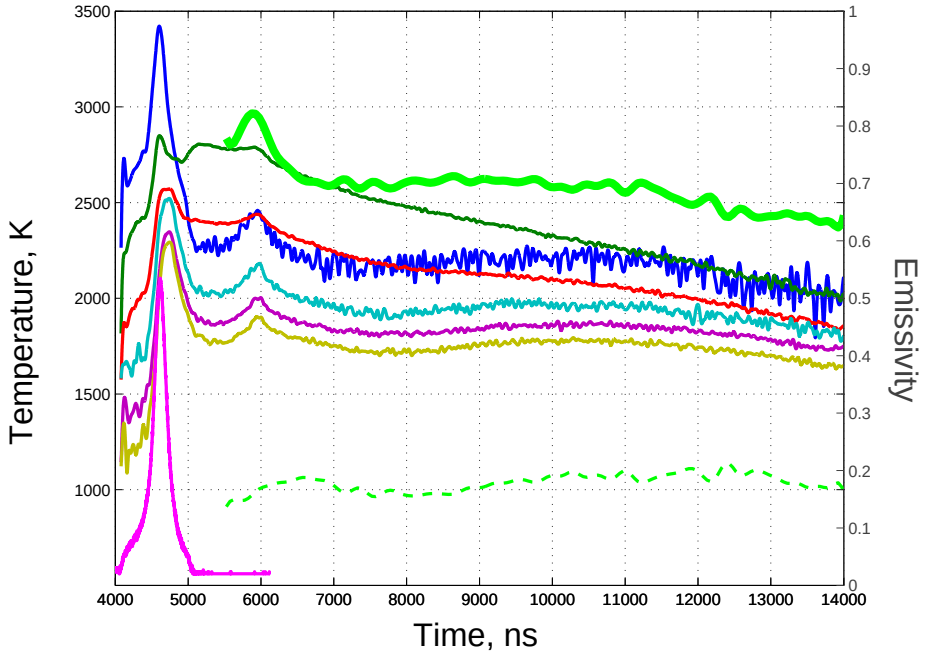

Figure 5.18: Brightness temperatures obtained from the self-emission of the sapphire sample. Radiation at 5000 ns obtains a thermal character making it even possible to fit it to the grey body model. The beam-targets position is similar to the experiment shown in Figure 5.17. Beam intensity in this experiment was $1.38 \cdot 10^9$ particles/bunch (Shot6, October 2005). Blue line — brightness temperature at 550 nm, green — at 750 nm, red — at 900 nm, cyan — at 1100 nm, lila — at 1300 nm, brown — at 1500 nm. Thick green line — grey temperature, dashed green — grey emissivity, magenta — FCT.

6 Suggestions for future experiments and conclusion

6.1 A Fast Laser Polarimeter

The next step in the temperature measurements of heavy-ion generated HED matter at the HHT should be the development of a technique that measures emissivity or reflectivity of the target material. A valuable addition to the pyrometric system would be a device that measures emissivity of a target simultaneously with the pyrometer. This may dramatically increase the accuracy of the temperature determination and will also provide information about electrical conductivity and phase transitions.

There are several different ways to determine the normal spectral emissivity, i.e. laser polarimetry [64], integrating sphere reflectometry [65], comparing the thermal radiation emitted from the surface of interest to the thermal radiation emitted from a black body cavity at the same temperature [66] or measuring the absorbance ratio at two wavelengths [37]. Recently, efforts have been made to apply reflectometry [67] and laser polarimetry [68] for dynamical measurements of emissivity for improvement of accuracy of temperature measurement in shock-compression experiments.

The laser polarimetry is one of the promising ways towards emissivity measurements in experiments with heavy ion beams. It is based on the measurement of the change in the state of polarization of a laser beam upon reflection at the surface of a sample. Figure 6.1 shows a schematic of the measurement geometry. From the measured change

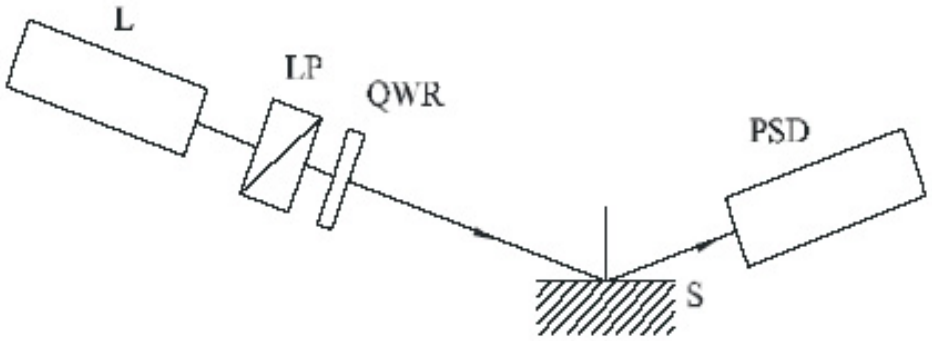

Figure 6.1: Schematic drawing of a laser polarimeter. L — laser; LP — linear polarizer; QWR — quarter-wave retarder; S — sample; PSD — polarization state detector.

in polarization the index of refraction, n and extinction coefficient k of the sample can be derived using the Fresnel equations [26]. Using the Kirchhoff's law in the energy

balance between the incident, absorbed, and reflected light fluxes at the surface of an opaque sample, the normal spectral emissivity of the sample is finally obtained from:

$$\epsilon = \frac{4n}{[(n+1)^2 + k^2]},$$

where ϵ the normal spectral emissivity, n-refraction index, k-extinction coefficient. This equation is only valid for vacuum (or air)- to-metal interfaces. More details the application of laser polarimetry to measurements on pulse-heated samples can be found, for example, in the reference [64].

6.2 Conclusions

The first HED physics experiments with heavy ion beams have been successfully carried out and have demonstrated a high potential for the present and future HED physics research with intense heavy ion beams. It was shown that even with existing ion beam parameters it is possible to generate HED matter samples with interesting unexplored states of matter, like overheated liquid, overcooled gas and two phase gas-liquid.

One of the key instruments in the performed experiments was the fast multichannel pyrometer. The pyrometer dynamically measures brightness temperature at 12 wavelengths in the visible and near infrared part of the spectrum with 5 ns temporal resolution. The unique design of the pyrometer allows simultaneous, independent temperature probing of two 400 μm-spots on the target surface. Several options for the optimal collection of light were investigated and finally an effective, compact and motorized light collection optics based on parabolic mirrors was elaborated. High efficiency of the collection optics and sensitivity of detectors allowed temperature measurements down to 800 K, while broad dynamic range of the system permitted temperature measurements up to 12000 K. The system is complete, fully operational and meets all demands of present experimental parameters in terms of speed, efficiency and accuracy of the measurement and no further improvements in the near future are needed. A slight modification will be required though, when the future FAIR facility will be operational, since higher and faster changing processes are expected. Electronics, detectors and filters that suit this future regime are available even now. The system is designed in the way that an upgrade towards higher temperatures and higher speed can be carried out rather easily.

The absolute intensity measured by the pyrometer at several different wavelengths permits application of various emissivity models for the determination of the physical temperature of the sample. In this work grey and linear models of emissivity models have been employed. It was demonstrated that application of these models is useful, since it reveals additional information that cannot be obtained from the analysis of the brightness temperatures. The multi-wavelength property of the pyrometer permit also application of more extensive models of emissivity based on real conductive properties of the sample.

In the course of the work various target materials such as copper, aluminum, tungsten, tantalum, sapphire and uranium dioxide, were irradiated ba intense uranium ion

beams. It was observed that different materials showed different behavior of hydrodynamic expansion, clearly seen on the pyrometer records. For the first time in the experiments with heavy ion beams tungsten and lead targets could be heated heated up to 12000 K. In these experiments the energy deposition of the ion beam was high enough to melt, and evaporate the entire sample. This high temperature value is already above the critical temperature of lead, which is the first demonstration that overcritical entropy states in a lead target can be achieved, with existing parameters of the ion beam.

In addition to temperature measurements, target expansion dynamics was measured using a backlighting/shadowgraphy system based on a streak camera. Expansion velocities up to 2600 m/s have been registered for lead and up to 1700 m/s for tungsten targets. In some experiments two expanding components were observed: fast expanding vapor and slow expanding liquid.

The developed fast multichannel pyrometer is indispensable for the present and the future HED physics experiments at GSI. The new experimental data, developed diagnostics and experience obtained during the course of this work are also of a great importance for planning future HED physics experiments at FAIR.

A Spectral characteristics

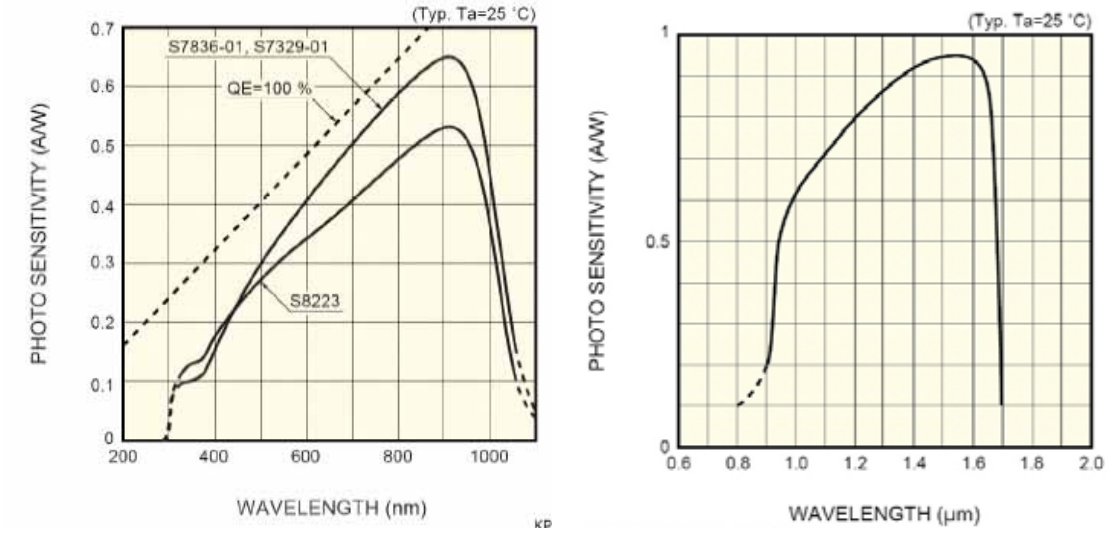

(a) Si Hamamatsu S7836-01 diode.

(b) InGaAS Hamamatsu G8376-05 diode.

Figure A.1: Spectral sensitivity of diodes used in the pyrometer.

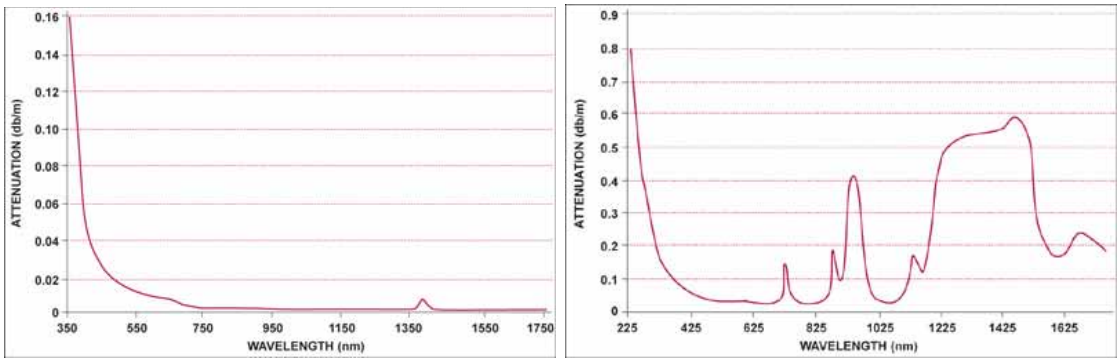

(a) VIS-NIF fiber.

(b) UV fiber.

Figure A.2: Light attenuation in glass fibers.

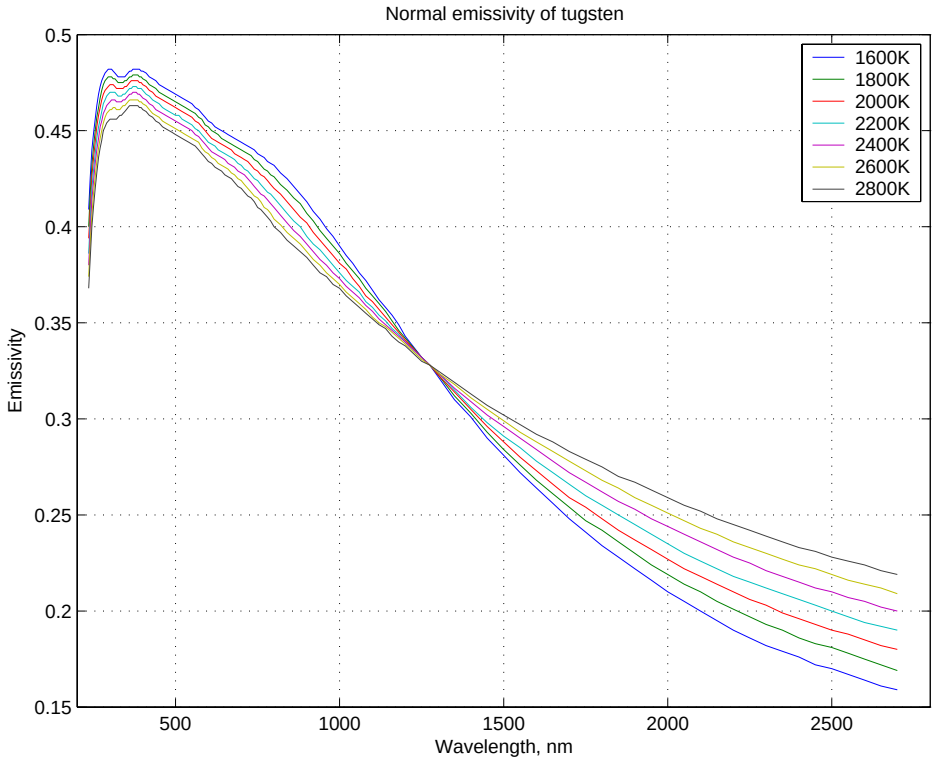

Figure A.3: Normal emissivity of tungsten.

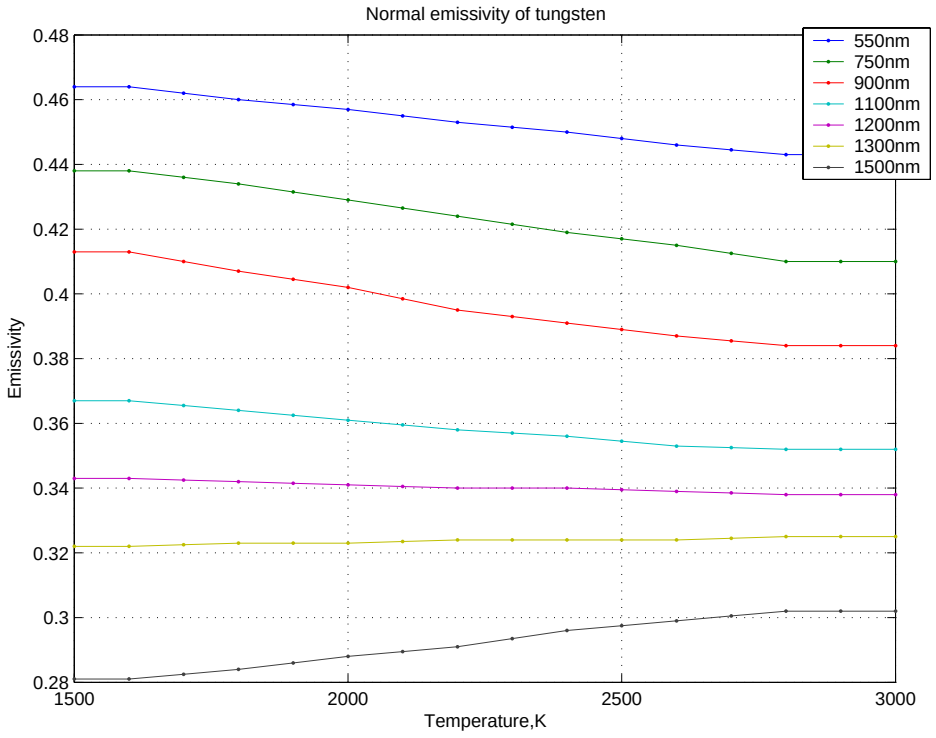

Figure A.4: Temperature behavior of normal emissivity of tungsten.

Bibliography

[1] A. Jayaraman, Rev. Mod. Phys., 55, (1983), 65.

[2] C.Narayan et al., Nature 393 (1998) 46.

[3] H.K.Mao and R.J.Hemley, Rev. Mod. Phys. 55 (1994) 671.

[4] J.M.Walsh,M. H. Rice, R. G. McQueen, F. L. Yarger, Phys. Rev.

[5] L. V. Altshuler, K. K. Krupnikov, M. I. Brazhnik, JETP, 7, (1958), 614.

[6] S. B. Kormer, A. I. Funtikov, V. D. Ulrin, A. N. Kolesnikova, Sov. Phys. - JETP, 15, (1962), 477. 108, (1957), 196.

[7] L. V. Altshuler, A. A. Bakanova, I. P. Dudoladov, E. A. Dynin, R. F. Trunin, B. S. Chekin, J. Appl. Mech. Techn. Phys., (22), (1981), 145.

[8] L. V. Altshuler, B. N.Moiseev, L. V. Popov, G. V. Simakov, R. F. Trunin, Sov. Phys. - JETP, 27, (1968), 420.

[9] R. F. Trunin,M. A. Podurets, B. N.Moiseev, G. V. Simakov, L. V. Popov, Sov. Phys. - JETP, 29, (1969), 630.

[10] Nellis et al., Phys. Rev. Lett., 89, 16 (2002)

[11] Y. B. Zeldovich, Y. P. Raizer, Physics of Shock Waves and High-Temperature Hydrodynamic Phenomena, Academic Press, New York (1966).

[12] G. R. Gathers, Rep. Progr. Phys., 49, (1986), 341.

[13] D.H.H. Hoffmann et al., Physics of Plasmas 9/9, 3651 (2002).

[14] N.A. Tahir, et.al., Phys. Rev.E 60(4), pp. 4715-4724,(1999).

[15] N.A. Tahir, et.al., Phys. Rev.E 61, pp. 1223-1232,(2000).

[16] N.A. Tahir, et.al., Phys. Rev. Spec. Topics Accel. Beams 6(2003) 020101.

[17] N.A. Tahir, et.al., Nucl. Instr. Meth. A544, (2005)16-26.

[18] S.Stoewe et al., Laser Part. Beams 18(2000)573-581.

[19] D. Varentsov et al., Laser Part. Beams 20(2002), 485-491.

[20] E. Dewald et.al., Laser Part. Beams 20(2002)521-526.

[21] Technical Proposal der HEDgeHOB Kollaboration,
URL: http://www.gsi.de/forschung/pp/TP-2005_e.pdf

[22] P. Hiernaut, R. Beukers, W. Heinz, R. Selfslag, M. Hoch, and R. W. Ohse, High Temp. High Press. 18:617 (1986).

[23] N.A. Tahir, et.al., Nucl. Instr. Meth. B 245, 85 - 93 (2006)

[24] V.W. Yuan, J. David Bowman, et.al., Phys. Rev. Lett., 94, 125504 (2005)

[25] S. H. Glenzer, G. Gregori,et.al., Phys. Rev. Lett., 90, 17 (2003)

[26] M. Born and E.Wolf, Principles of Optics, 7th edition, Cambridge,University Press (2002)

[27] A. Cezairliyan, J. Res. Natl. Bur. Stand. (U.S.). 75C:7 (1971).

[28] A. Cezairliyan, S. Krishnan, and J. L McClure, Int. J. Thermophys. 17:1455 (1996).

[29] B. Coates. High Temperatures-High pressures, 20 pp433-441(1988).

[30] M. A. Pellerin, B. K. Tsai, D. P. DeWitt, and G. J. Dall, in Temperature, Its Measurement and Control in Science and Industry, American Institute of Physics, Vol. 6, Part 2 (1992), p. 871.

[31] P.Drude, Annalen der Physik 14, 936 (1904)

[32] D. J. Price, 1949 Proc. Phys. Soc. A 62 278-283

[33] R.Hagens, Annalen der Physik 8,(1903)

[34] L. Michalski, K. Eckersdorf, J. Kucharski, J.McGhee, Temperature Measurement Second Edition, 2001 John Wiley

[35] P.Celliers and A.Ng, Phys. Rev. Lett., 90, 17 (2003)

[36] J. L. Gardner, T. P. Jones, and M. R. Davies, High Temp High Pressures 13, 459 (1981).

[37] D.P. Dewitt, Therory and practice of radiation thermometry, John wiley and& Sons, Inc., (1998).

[38] D. Varentsov, PhD thesis, TU-Darmstadt, (2002)

[39] G. Pottlacher et.al., Journal of Non-Crystalline Solids, 205-207(1996), 265-269.

[40] M. Kulish et.al., Rev. Sci. Inst., 72, 5(2001)

[41] S. Udrea, PhD thesis, TU-Darmstadt, (2004)

[42] A. Hug, Diploma thesis, TU-Darmstadt, (2006)

[43] G.R. Gathers, Int. Journal of Thermophysics,173-175, 13,1(1992).

[44] J. L. Gardner and T. P. Jones, J. Phys. E: Sci. Instum. 13:306(1980).

[45] C. Ronchi, R. Beukers, H. Heinz, J. P. Hiernaut, and R. Selfslag, Int. J. Thermophys. 13:107 (1992). J.

[46] G.A. Lyzenga, T.J. Ahrens, Rev. Sci. Inst 50, 1421-1424(1979).

[47] S. Ackerman, in Temperature: Its Measurement and Control in Science and Industry, A. I. Dahl, Ed. (Instrument Society of America, Pittsburgh, 1962), 3, Part 2, p. 849.

[48] G. H. Hornbeck, in [47]. 2, p. 475.

[49] M. Pasta, G. Ruffino, P. Soardo, and G. Toselli, High Temp. High Pressures 5, 99 (1973).

[50] K. L. Cashdollar, Appl. Opt. 18, 2595 (1979).

[51] J. L. Gardner, T. P. Jones, W.G. Sainty, Appl. Opt. 21, 1259 (1982).

[52] G.R. Gathers, Int. Journal of Thermophysics, 539-554, 13,3(1992).

[53] A. Cezairliyan, et. al., High Temperatures-High Pressures, 8, 103-111, (1976).

[54] N. Jackse, et.al., Phys. Rev. B 70, 174203 (2004).

[55] L. Cortella, et.al., Phys. Rev. Lett. 70, 1469-1472 (1993).

[56] Pyaling A., et.al., Int. J. of Thermophys.7993-1001(1998).

[57] A.V. Bushman, V.E. Fortov, Sov. Phys. Usp. 26 (1983) 465.

[58] F.D. Bennett in Physics of High Energy Density, part 7, eds. P. Caldirola and H. Knoepfel, Academic Press, New York and London, 1971.

[59] V.Ya. Ternovoi, V.E. Fortov et al., in Physics of Strongly Coupled Plasmas, eds. W.D. Kraeft et al., World Scientific Publishing Ltd, Singapore, 1996, pp.119-124.

[60] N.N. Novikov, Zh. Prikl. Mekh. Tekh. Fiz. 3, (1962) 22.

[61] V.E. Fortov, M.E. Lebedev, V.Ya Ternovoi, Rev. Gen. Therm. Fr. 371 (1992) 589.

[62] V.Ya. Ternovoi, A.S. Filimonov et al., in proceedings of Shock Compression of Condensed Matter 1997, p. 87.

[63] D. Partouche-Sebban , Physica B 364 1-13 (2005).

[64] G. Pottlacher, A. Seifter, Int. J. Thermophys., Vol. 23, No. 5, p1281-1291, 2002.

[65] F. Righini, G. C. Bussolini, A. Rosso, Proceedings of TEMPMEKO 96, ed. P. Marcino, Levrotto & Bella, Torino, pp. 489-492, 1997.

[66] A. Cezairliyan, J. Res. Nat. Bur. Stand., Vol. 75c, No. 1, 1971.

[67] P. Poulsen, D. E. Hare, "Temperature and wavelength dependent emissivity of a shocked surface: A first experiment.", Lawrence Livermore National Laboratory Report (UCRL-JC-146809).

[68] A. W. Obst, K. R. Alrick, K.Boboridis, W. T. Buttler, B. R. Marshall, J. R. Payton, M. D. Wilke, Int. J. Thermophys., Vol. 23, No. 5, p 1259-1266, 2002.

Acknowledgments

At the end of my work, I am very glad to have the opportunity to express my gratitude to the people whose collaboration and support have made the completion of this work ever possible.

First of all, I am happy to acknowledge Prof. Dr. Dr. h.c./RUS Dieter H.H. Hoffmann who offered me the opportunity to work on exciting subject of research in the first-class laboratory, with the high-end equipment and with the high-class professionals. I am grateful from the bottom of my heart for his invaluable encouragement, support, advice, understanding, kind care and friendly assistance that was always there even besides the professional activities.

I am particularly grateful to my colleague Dr. Dmitry Varentsov for his his readiness to discuss science all the time, for devotedly sharing with me his knowledge and experience, for his competent assistance and for his sincere comments and advises. His contribution to my formation as a scientist is indeed enormous.

I deeply appreciate the great help in preparation of our experiments and sharing with me the long and difficult beam time shifts by the entire HHT experimental team, all the graduate students, postdoctoral fellows and researchers: Dr. Serban Udrea, Dipl.-Phys. Alexander Hug, David Fernengel and Yuri Menzel. Thank you very much, guys!

I wish to especially thank my Russian collaborators from the IPCP and ITEP. I am deeply grateful to Mikhail Kulish, Dimitry Nikolaev, Dr. Vladimir Ternovoy, Dr. Alexander Fertmann and Dr. Vladimir Turtikov for their important contributions to this work, for their competent help with experiments and for sharing with me their priceless knowledge and experience.

It also a pleasure to express my gratitude to Dr. Naeem Thair for his extensive theoretical support, advices and help with writing this work. I am also grateful to Dr. Abel Blazevic, Dr. Karin Weyrich and Dipl.-Phys. Renate Knobloch for giving valuable comments regarding my thesis.

I am also indebted to the TU and GSI workshop people for their efficient work. In particular I would like to thank Dipl.-Ing. Heinrich Wahl, Dipl.-Ing. Gerhard Klappich, Dipl.-Ing. Markus Romig and Dipl.-Ing. Kalliopi Dermati.

I want to acknowledge "the laser fraction" of the plasma physics group, Prof. Dr. Markus Roth, Dipl.-Phys. Gabriel Schaumann, Dipl.-Ing. Marius Schollmeier, and Dipl.-Phys. Thomas Hessling for educating me about their fascinating experiments with the "big scary laser".

The research was funded by the Graduiertenkolleg "Physik und Technik von Beschleunigern" (GRAKO). I want to use the chance and thank the speaker of the GRAKO Prof. Dr. Dr. h.c. mult. Achim Richter.

At the end I am very grateful for the continuous encouragement and support of my family during this work as well as during my whole life. I would like to specially thank my father, Prof. Dr. Alexander Ni, who always could motivate me to study and continuously advised me: "never stop at achieved things and always advance further". My special thanks also goes to my mother, Dipl.-Ing. Galina Truhina, for her caress, kindness and endless love.

Curriculum Vitae

Name: Pavel Ni
Birth date/place: 20 August 1981, Alma-Ata, USSR.
Citizenship: Russian

Education profile:

1988-1998: Chernogolovka High School N82, Russia.
1998-2003: Student at Moscow Institute of Physics and Technology, Russia.
2002: Internship in Schlumberger Ltd., Tokyo, Japan.
2003: Internship in Alstom Ltd., Dättwill Switzerland.
From 1 Oktober 2003 PhD student at TU Darmstadt.

Hiermit erkläre ich, dass ich die Arbeit selbständig und nur mit den angegebenen Hilfsmitteln angefertigt und nicht schon früher eine Promotion versucht habe.

4 Juli 2006 Pavel Ni